INFORMATION TO USERS

RADIATIVE IMPACT OF ATMOSPHERIC AEROSOLS AND CLOUDS

By

Jeff Wong

Your file Votre référence

Our file Notre référence

0-612-36594-8

Canada

DALHOUSIE UNIVERSITY

FACULTY OF GRADUATE STUDIES

The undersigned hereby certify that they have read and recommend to the Faculty of

Graduate Studies for acceptance a thesis entitled "Radiative Impact of Atmospheric

Aerosols and Clouds"

_____

by   Jeff Wong

_____

in partial fulfillment of the requirements for the degree of Doctor of Philosophy.

Dated: _____ August 28, 1998 _____

External Examiner ___

Research Supervisor ___

Examining Committee ___
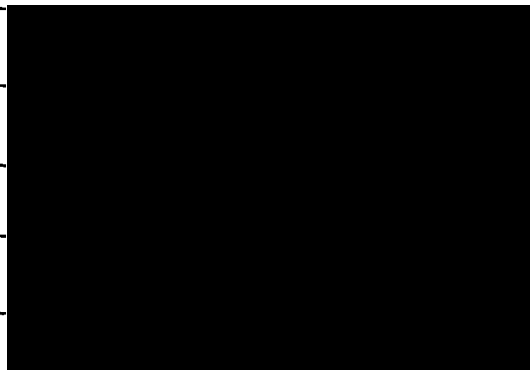
DALHOUSIE UNIVERSITY
DEPARTMENT OF
PHYSICS

The undersigned hereby certify that they have read and recommend to the Faculty of Graduate Studies for acceptance a thesis entitled "**Radiative Impact of Atmospheric Aerosols and Clouds**" by **Jeff Wong** in partial fulfillment of the requirements for the degree of **Doctor of Philosophy**.

Dated: <u>July 1998</u>

External Examiner: ███████████████████████
Dr. L. Barrie

Research Supervisor: _____
Dr. Petr Chýlek

Examing Committee: _____
Dr. J. G. Cordes

_____
Dr. U. Lohmann

DALHOUSIE UNIVERSITY

Date: **August 28, 1998**
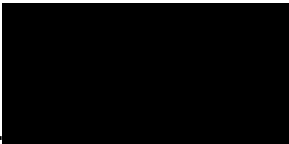
Author: **Jeff Wong**

Title: **Radiative Impact of Atmospheric Aerosols and Clouds**

Department: **Physics**

Degree: **Ph.D.**   Convocation: **October**   Year: **1998**

Permission is herewith granted to Dalhousie University to circulate and to have copied for non-commercial purposes, at its discretion, the above title upon the request of individuals or institutions.

_____
Signature of Author

Contents

List of Tables

List of Figures

敬獻給親愛的家人

Dedicated to my family

黃元彬

Yuen Bun Wong

黃伍綺雲

Yee Wan Wong

黃毅龍

Ngai Lung Wong

黃家賢

Kenneth Ka Yin Wong

Abstract

The effect of aerosols and clouds on Earth's shortwave radiation budget is studied in this thesis.

An expression for the global annual mean radiative forcing due to sulfate aerosols is extended for absorbing aerosols using a two-stream approximation. This expression depends on the backscattering fraction of the aerosol which varies with the effective radius of the aerosol size distribution. This variation leads to a factor of 2.0 variation in the radiative forcing of slightly absorbing aerosols.

Water vapor condenses onto hygroscopic aerosols which results in a change in size and a change in the concentration of the chemical components of the aerosol. The original Köhler equation accurately describes the equilibrium size of a hygroscopic aerosol. Use of the modified Köhler equation leads to errors due to its thermodynamically inconsistent nature. On a global annual average, the direct radiative forcing of hygroscopic sulfate aerosol is $-0.69 \, \mathrm{W \, m^{-2}}$. Over highly polluted regions, the local radiative forcing can be as high as $-7 \, \mathrm{W \, m^{-2}}$ which is comparable to the forcing due to increased greenhouse gas concentrations.

Using a plane-parallel model, an analytical expression is derived for the cloud radiative forcing ratio which is used as a measure of enhanced shortwave radiation absorption of clouds. With this model, high values of this ratio can be achieved by thick clouds with absorptances of approximately 0.3. High values of the ratio can also be obtained with low level clouds if the transmittance of the atmosphere above the cloud is reduced to approximately 0.8. This can be achieved by a high concentration of strongly absorbing aerosols.

List of Symbols

a : surface albedo

a_0, a_1, a_2, a_3, a_4 : fitting coefficients

A_1, A_2, A_3, A_4 : constants

a_w : water activity

α : coefficient of the optical depth in the two-stream approximation

A : absorptance

A : surface area [m^2]

A_c : initial absorptance of the cloudy atmospheric layer

A_c' : initial absorptance of the cloudy atmospheric layer for light that has been reflected by the surface

A^{dd} : absorbed flux by a cloudy sky column [W m^{-2}]

A^{dr} : absorbed flux by a clear sky column [W m^{-2}]

ACE : Aerosol Characterization Experiment

B : aerosol burden [g m^{-2}]

β : backscattering fraction integrated over all incident angles

$\beta(\mu_0)$: backscattering fraction of radiation for incident radiation with a cosine of the angle of incidence of μ_0.

C_1, C_2, C_3, C_4 : constants

CCM2 : the second version of the Community Climate Model — the GCM produced by NCAR

CRF : cloud radiative forcing [$\mathrm{W\,m^{-2}}$]

CRF_{atm} : cloud radiative forcing of the atmospheric column [$\mathrm{W\,m^{-2}}$]

CRF_S : cloud radiative forcing at the surface [$\mathrm{W\,m^{-2}}$]

CRF_T : cloud radiative forcing at the top of the atmosphere [$\mathrm{W\,m^{-2}}$]

d : the coefficient of the surface albedo in the approximate $\Re$ equations

ΔF_R : direct aerosol radiative forcing [$\mathrm{W\,m^{-2}}$]

ΔG : direct aerosol radiative forcing normalized by the aerosol burden [$\mathrm{W\,g^{-1}}$]

ΔR : change in planetary albedo due to an aerosol layer

$\frac{dN}{dr}(r)$: particle number size distribution [$\mathrm{cm^{-3}\mu m^{-1}}$]

$\frac{dS}{d\lambda}(\lambda)$: incident solar flux at the top of the atmosphere [$\mathrm{W\,m^{-2}\,\mu m^{-1}}$]

ERBE : Earth Radiation Budget Experiment

F : net downward radiative flux [$\mathrm{W\,m^{-2}}$]

F_- : downward radiative flux [$\mathrm{W\,m^{-2}}$]

F_+ : upward radiative flux [$\mathrm{W\,m^{-2}}$]

F_0 : incident solar flux [$\mathrm{W\,m^{-2}}$]

F^{all} : net all sky radiative flux [$\mathrm{W\,m^{-2}}$]

F^{cd} : net cloudy sky radiative flux [W m^{-2}]

F^{cd}_{-S} : downward cloudy sky radiative flux at the surface [W m^{-2}]

F^{cd}_{+S} : upward cloudy sky radiative flux at the surface [W m^{-2}]

F^{cd}_{-T} : downward cloudy sky radiative flux at the top of the atmosphere [W m^{-2}]

F^{cd}_{+T} : upward cloudy sky radiative flux at the top of the atmosphere [W m^{-2}]

F^{cr} : net clear sky radiative flux [W m^{-2}]

F^{cd}_{-S} : downward clear sky radiative flux at the surface [W m^{-2}]

F^{cd}_{+S} : upward clear sky radiative flux at the surface [W m^{-2}]

F^{cd}_{-T} : downward clear sky radiative flux at the top of the atmosphere [W m^{-2}]

F^{cd}_{+T} : upward clear sky radiative flux at the top of the atmosphere [W m^{-2}]

ϕ : azimuthal angle

g : asymmetry parameter

g^i : asymmetry parameter of wavelength band i

g_s : asymmetry parameter of a single particle

G : Gibbs free energy [J]

GCM : global climate model

i : complex number unit [$= \sqrt{-1}$]

i : van't Hoff factor

I_λ : monochromatic intensity of wavelength λ [W m^{-2} sr^{-1}]

I^+ : upward intensity stream

I^- : downward intensity stream

I_0 : incident downward intensity at the top of the aerosol layer

I_R : incident upward intensity at the bottom of the aerosol layer

k_B : Boltzmann's constant $[= 1.381 \times 10^{-23} \, \text{J} \, \text{K}^{-1}]$

k_{ext} : extinction coefficient $[\text{m}^{-1}]$

k_{ext}^i : extinction coefficient of wavelength band i $[\text{m}^{-1}]$

k_{sc}^i : scattering coefficient of wavelength band i $[\text{m}^{-1}]$

λ : wavelength $[\mu\text{m}]$

$\ln \sigma_0$: standard deviation of $\ln r$ in a lognormal number size distribution

$\ln \sigma_0'$: standard deviation of a lognormal size distribution of wet aerosols

LWC : liquid water content $[\text{g} \, \text{m}^{-3}]$

m_{eff} : effective refractive index of a solution

m_j : refractive index of component j in a solution

m_s : mass of solute in a solution $[\text{g}]$

m_w : mass of solvent in a solution $[\text{g}]$

M : molality [mole of solute per kg of solvent]

M : aerosol mass concentration $[\text{g} \, \text{m}^{-3}]$

M_s : molecular weight of solute molecules $[\text{g} \, \text{mole}^{-1}]$

M_w : molecular weight of solvent molecules $[\text{g} \, \text{mole}^{-1}]$

$M_{SO_4^{-2}}$: sulfate mass concentration $[\text{g} \, \text{m}^{-3}]$

μ, μ' : cosine of zenith angles

μ_0 : cosine of the zenith angle of the incident radiation

μ_L : equilibrium chemical potential of a solvent molecule in the liquid phase [J]

μ_L^0 : reference chemical potential of a solvent molecule in the liquid phase [J]

μ_L' : equilibrium chemical potential of a solute molecule in the liquid phase [J]

μ_V : equilibrium chemical potential of a solvent molecule in the vapor phase [J]

μ_V' : equilibrium chemical potential of a solute molecule in the vapor phase [J]

n_L : number of solvent molecules in a solution

n_L' : number of solute molecules in a solution

$n_{L,b}$: number of solvent molecules in the bulk phase of a solution

$n_{L,b}'$: number of solute molecules in the bulk phase of a solution

$n_{L,s}$: number of solvent molecules on the surface of a solution

$n_{L,s}'$: number of solute molecules on the surface of a solution

n_V : number of solvent molecules in a vapor phase

n_V' : number of solute molecules in a vapor phase

N : fractional cloud cover

N_A : Avogadro's number [= $6.022 \times 10^{23}\, mole^{-1}$]

N_0 : total particle number density [cm^{-3}]

NASA : National Aeronautics and Space Agency of the United States

NCAR : National Center for Atmospheric Research of the United States

p : equilibrium pressure [Pa]

p_L : equilibrium pressure in solution droplet [Pa]

p_∞ : equilibrium vapor pressure over a flat surface of pure solvent [Pa]

p'_∞ : equilibrium vapor pressure over a flat surface of solution [Pa]

P_λ : scattering phase function at wavelength λ

ρ : mass density [g cm^{-3}]

ρ_w : mass density of water [$= 1.0$ g cm^{-3}]

r : particle radius [μm]

r : clear sky atmospheric reflectance

r_0 : geometric mean radius in a lognormal number size distribution [μm]

r'_0 : geometric mean radius of a lognormal size distribution of wet aerosols [μm]

r_{eff} : effective radius of a particle size distribution [μm]

r_a, r_b, r_d : dry particle radii [μm]

$\tilde{r}_a, \tilde{r}_b$: wet particle radii [μm]

R : reflectance

$\mathfrak{R}$: cloud radiative forcing ratio

R^* : universal gas constant [$= 8.314$ J mole^{-1}K^{-1}]

R' : reflectance of the combined system of the atmospheric column, aerosol layer, and underlying surface

R^{Lalb} : cloud radiative forcing ratio for low surface albedo

R^{approx} : approximation of the cloud radiative forcing ratio

R^{Lcld} : approximate cloud radiative forcing ratio for the low cloud situation

R^{thick} : approximate cloud radiative forcing ratio for the thick cloud situation

R_a : reflectance of the upper atmospheric layer

R_c : initial reflectance of the cloudy layer

R_c' : reflectance of the cloudy layer for light that has been reflected by the surface

rh : relative humidity scaled to unity

σ : surface tension [$\mathrm{N\,m^{-1}}$]

σ_{ext} : particle extinction cross section [$\mathrm{m^2}$]

σ_{sc} : particle scattering cross section [$\mathrm{m^2}$]

S_0 : solar constant [$\approx 1370\,\mathrm{W\,m^{-2}}$]

t : initial clear sky atmospheric transmittance

t' : clear sky atmospheric transmittance for light that has been reflected by the surface

T : temperature [K]

T : transmittance

T_a : transmittance of the atmospheric layer above the aerosol layer

T_a : initial transmittance of the upper atmospheric layer

T_a' : upper atmospheric layer transmittance for light that has been reflected by the surface

T_a'' : upper atmospheric layer transmittance for light that is reflected by the cloudy layer but not by the surface

T_b : initial transmittance of the lower atmospheric layer

T_b' : lower atmospheric layer transmittance for light that has been reflected by the surface

T_c : initial transmittance of the cloudy atmospheric layer

T_c' : cloudy atmospheric layer transmittance for light that has been reflected by the surface

τ : extinction optical depth

τ_λ : extinction optical depth at wavelength λ

τ_{abs} : absorption optical depth

τ_{sc} : scattering optical depth

τ_{abs}^* : absorption optical depth of the aerosol layer

τ_{sc}^* : scattering optical depth of the aerosol layer

θ : zenith angle

TARFOX : Tropospheric Aerosol Radiative Forcing Observational Experiment

v_j : volume fraction of component j in a solution

ν : partial molar volume of water [m^3]

ω : single scattering albedo

ω_λ : single scattering albedo at wavelength λ

ω^i : single scattering albedo of wavelength band i

ζ : an arbitrary optical property

Acknowledgements

First and foremost, I would like to thank my research supervisor Dr. Petr Chýlek for this learning experience and for the opportunity to share his broad research interests.

I would also like to thank Dr. Jeffrey Kiehl and Bruce Briegleb of the National Center for Atmospheric Research for the help they provided during my visit there. My thanks go to Dr. Philip Russell, John Livingston, and Dr. Robert Bergstrom associated with the National Aeronautics and Space Administration. My thanks also go to Dr. Zhanqing Li for my stay at the Canada Centre for Remote Sensing. I am also grateful for the help I received from Dr. Qiang Fu and for his radiation model that he provided for use. I am indebted to Dr. Glen Lesins for his help and suggestions. I appreciate the constructive criticism from the readers of this thesis: Dr. John G. Cordes and Dr. Ulrike Lohmann; and from the external examiner Dr. Leonard A. Barrie.

I am thankful for the companionship of past and present colleagues of the Atmospheric Science Program of Dalhousie University (in alphabetical order): Maureen Cribb, Peter Damiano, Steven Dobbie, Stephen Gosse, Jeff Jardine, Dr. Linhong Kou, Dr. Jiangnan Li, Lisa Phinney, Dr. William Tso, Dr. Gorden Videen, Dr. Muyin Wang, and Barbara Winter.

I would like to thank Dalhousie University for providing an excellent academic setting and scholarship support.

Chapter 1

Introduction

Climate models are becoming more ambitious in their attempts to simulate the Earth's climate. The increase in the programs' sophistication is made possible by the rise in computing capabilities, and more importantly by the advancements in the understanding of climatic processes.

Ocean, land, and atmospheric processes are driven by the solar and terrestrial energy that propagate through the atmosphere by radiative transfer. Solar and terrestrial radiation can be characterized by the range of wavelengths that they encompass. Over 99% of solar radiation is accounted for by wavelengths less than $4\,\mu m$ whereas the majority of terrestrial radiation emitted by the planet has wavelengths greater than $4\,\mu m$ (Liou 1980). Due to this difference, solar radiation is characterized as shortwave radiation and terrestrial radiation as longwave radiation. With the help of satellite technology, the global annual average flux of solar energy that enters the Earth's atmosphere is measured to be $342\,W\,m^{-2}$. Of this amount, $238\,W\,m^{-2}$ is absorbed. The amount of longwave radiation that leaves the planet is $235\,W\,m^{-2}$ (Kiehl and Trenberth 1997). The global mean average annual uncertainty in the satellite measurements is $7.8\,W\,m^{-2}$ (Rieland and Raschke 1991). This means that the Earth is in radiative equilibrium to within measurement errors. There is higher confidence in the longwave results, so the absorbed shortwave flux is taken to be $235\,W\,m^{-2}$ (Kiehl and Trenberth 1997). The amount of energy absorbed, reflected, and emitted

1

by the atmosphere is influenced by the presence of aerosols and clouds.

Terrestrial radiation is absorbed and re-emitted by gases and clouds before it finally leaves the planet. The extent at which gases and clouds interact with longwave radiation depends on their ability to absorb radiation at different wavelengths and on the temperature of the absorber. In cloud free atmospheres, the difference in the global annual longwave flux emitted by the surface ($390\,\mathrm{W\,m^{-2}}$) and the flux that leaves the top of the atmosphere ($265\,\mathrm{W\,m^{-2}}$) is approximately $125\,\mathrm{W\,m^{-2}}$. It is estimated that 60% of this difference is due to water vapor and 26% is due to carbon dioxide. Clouds decrease the amount of terrestrial radiation that leaves the top of the atmosphere by $30\,\mathrm{W\,m^{-2}}$. Clouds increase the amount of longwave radiation that is re-emitted to the surface by the atmosphere by approximately $46\,\mathrm{W\,m^{-2}}$ from $278\,\mathrm{W\,m^{-2}}$ to $324\,\mathrm{W\,m^{-2}}$ (Kiehl and Trenberth 1997). The effect of clouds on the longwave radiative flux at the surface is uncertain since it depends on the amount of cloud cover and on the location of the clouds in the atmosphere. Estimates of the net upward flux of longwave radiation at the surface of the planet varies from $40\,\mathrm{W\,m^{-2}}$ to as high as $72\,\mathrm{W\,m^{-2}}$ (Kiehl and Trenberth 1997).

Climate models predict that the amount of shortwave radiation that is absorbed by the surface and by the atmosphere alone is approximately $168\,\mathrm{W\,m^{-2}}$ and $67\,\mathrm{W\,m^{-2}}$ respectively. Approximately $7\,\mathrm{W\,m^{-2}}$ of the $67\,\mathrm{W\,m^{-2}}$ is due to the presence of clouds. In cloud free atmospheres, water vapor is responsible for approximately 70% of the $60\,\mathrm{W\,m^{-2}}$ shortwave absorption and ozone follows with almost 25% of the absorption (Kiehl and Trenberth 1997). The effect of clouds is to decrease the total solar absorption of the atmosphere and surface by $50\,\mathrm{W\,m^{-2}}$.

Recent measurements by Cess et al. (1995), Ramanathan et al. (1995), and Pilewskie and Valero (1995) suggest that cloudy atmospheres absorb approximately $20\,\mathrm{W\,m^{-2}}$ more solar radiation than what is predicted by radiation and climate models. Since there is a high level of confidence on estimates of the total amount of solar radiation absorbed by the surface and atmosphere together ($235\,\mathrm{W\,m^{-2}}$) due to satellite observations, this means that the solar radiation absorbed by the atmosphere is

$87\,\mathrm{W\,m^{-2}}$ and the amount absorbed by the surface is only $148\,\mathrm{W\,m^{-2}}$. If the enhanced shortwave absorption by clouds is due to an unaccounted for physical mechanism, the implications are significant. Using the global climate model produced by the National Center for Atmospheric Research (NCAR), Kiehl et al. (1995) find enhanced shortwave cloud absorption results in a $4\,\mathrm{K}$ warming of the troposphere, and a reduction in surface wind speeds. But it is not clear if there is a true discrepancy in our understanding of shortwave absorption by clouds. The enhanced shortwave absorption by clouds of $20\,\mathrm{W\,m^{-2}}$ observed by Cess et al. (1995) may only re-emphasize that the solar radiation budget is uncertain. Estimates of the amount of solar radiation that is absorbed by the surface alone varies between $142\,\mathrm{W\,m^{-2}}$ and $191\,\mathrm{W\,m^{-2}}$ (Li et al. 1997), and the amount absorbed by the atmosphere is between $56\,\mathrm{W\,m^{-2}}$ and $98\,\mathrm{W\,m^{-2}}$ (Li et al. 1997). This is a spread greater than $40\,\mathrm{W\,m^{-2}}$.

A portion of the uncertainty in the shortwave radiation budget is attributed to atmospheric aerosols. Aerosols affect the radiation budget directly by absorbing and scattering solar radiation back to space (Charlson et al. 1992). Aerosols can also influence the radiation budget indirectly in their role as condensation nuclei for cloud droplets. The size distribution of cloud droplets and the lifetime of the cloud is affected by the concentration and chemical composition of the aerosols, which in turn affects cloud albedo (Lohmann and Feichter 1997; Twomey 1974). Interest in the radiative impact of aerosols has been focused on sulfate aerosols because their concentration in the atmosphere has risen due to human industrial activities (Boucher and Anderson 1995; Nemesure et al. 1995; Kiehl and Briegleb 1993). Radiative forcing is a measure of the radiative impact of a perturbation to the climate system. The radiative forcing of the direct effect of sulfate aerosols is on the order of $-1\,\mathrm{W\,m^{-2}}$ and an additional $-1\,\mathrm{W\,m^{-2}}$ of radiative forcing is due to the indirect effect (Charlson et al. 1992). The negative value implies a cooling effect on the climate system.

The combined aerosol forcing is comparable to the radiative forcing of $+2.45\,\mathrm{W\,m^{-2}}$ that is estimated to be due to the increase in greenhouse gas concentrations in the atmosphere since the beginning of the industrial age (Schimel et al. 1996). Due to the

differences in the spatial and temporal distribution of sulfate aerosols in comparison to greenhouse gases, this does not mean that they cancel each other locally. In highly polluted regions, the direct radiative forcing of sulfate aerosols is stronger than the greenhouse gas forcing (Kiehl and Rodhe 1995).

The purpose of this thesis is to examine how tropospheric aerosols and clouds affect the Earth's solar radiation budget. In particular, the direct radiative effect of both absorbing and non-absorbing tropospheric aerosols is studied; and the enhanced shortwave radiation absorption of clouds is examined.

In the following chapter absorbing aerosols are discussed. In particular, the solar radiative forcing of aerosols produced by biomass burning in cloud free skies is considered. A simple expression for the clear sky radiative forcing of an optically thin layer of absorbing aerosols is derived. The radiative forcing is proportional to the change in the reflectance of the layer after the introduction of aerosol in that layer. A two-stream radiative transfer model is used to calculate this change in reflectance. The dependence of the radiative forcing on the assumed refractive index of the aerosol is examined as well as the dependence on the assumed size distribution of the aerosol.

The optical properties of sulfate, nitrate, and sea salt aerosols are discussed in the next two chapters. Calculation of the optical properties of these aerosols is complicated by their hygroscopic nature. An amount of water vapor condenses on these particles depending on the ambient relative humidity which changes the size of the particles as well as the concentration of the chemical components that make up the aerosol. This, in turn, changes their light scattering characteristics. In order to study the radiative impact of hygroscopic aerosols, the growth of these particles with relative humidity must be understood.

Chapter 3 discusses the Köhler equation which describes the equilibrium size of a single hygroscopic aerosol as a function of relative humidity (Köhler 1936). Modifications of the Köhler equation have been proposed by several authors (Young and Warren 1992; Doyle 1961) that account for the concentration dependence of the variables in the Köhler equation. When the aerosol radius predicted by the original Köhler

equation and by the modified Köhler equation are compared to measurements, it is the original Köhler equation that agrees with the observations. Reasons for this discrepancy are presented. The Köhler equation is then used to predict the change in the aerosol size distribution as a function of relative humidity.

Now that the change in hygroscopic aerosol size distribution can be modeled, calculation of the optical properties of hygroscopic aerosols can proceed. This is described in chapter 4. How the radiative forcing due to the aerosols changes with relative humidity is considered. Sensitivity to the assumed initial dry size distribution is examined and the effect of using an average refractive index for the particle using volume as a weighting function is considered. The optical properties and radiative forcing of aerosols with different chemical compositions are compared.

A simple three layer atmospheric model is used to study the effect of clouds on Earth's shortwave radiation budget in chapter 5. The focus is on the possible enhanced shortwave radiation absorption proposed by Cess et al. (1995) and Ramanathan et al. (1995). They introduce a quantity denoted by $\Re$ that is equal to the ratio of the cloud radiative forcing observed at the surface to the cloud radiative forcing observed at the top of the atmosphere. This quantity is used as a measure of the enhanced shortwave radiation by clouds that they proposed. They find that $\Re \approx 1.5$ whereas current radiation and climate models predict $\Re \approx 1.0$. Using the atmospheric model an analytical expression for $\Re$ is derived. This expression is used to show the sensitivity of $\Re$ to atmospheric parameters and to suggest possible mechanisms that result in high values of this ratio.

In the final chapter, the conclusions drawn in this study are summarized and discussed. Suggestions are made concerning future improvements that can be made concerning Earth's shortwave radiation budget.

Chapter 2

Absorbing Aerosols

2.1   Introduction

Aerosols reflect a part of incoming solar radiation back to space (direct effect) and they modify cloud droplet size distribution which affects cloud albedo and cloud life time (indirect effects). Charlson et al. (1992) estimate the direct globally averaged radiative forcing due to anthropogenic sulfate aerosol to be $-1\,\mathrm{W\,m^{-2}}$ with an additional indirect effect by modifying cloud albedo of around $-1\,\mathrm{W\,m^{-2}}$. Penner et al. (1992) suggest that an additional globally averaged direct and indirect radiative forcing of about $-1\,\mathrm{W\,m^{-2}}$ each is due to radiative effects of smokes produced by biomass burning. Penner et al. (1992) note that the estimated radiative effects of anthropogenic sulfate and smoke aerosols had been probably exaggerated because otherwise a decrease of the global temperature should have been observed since the last century.

The direct radiative effect of anthropogenic sulfate aerosol have been investigated recently by Kiehl and Briegleb (1993) and Taylor and Penner (1994) using three dimensional models. The estimated direct globally averaged radiative forcing varied from $-0.3\,\mathrm{W\,m^{-2}}$ (Kiehl and Briegleb 1993) to $-0.9\,\mathrm{W\,m^{-2}}$ (Taylor and Penner 1994). The indirect aerosol radiative forcing is even more complicated to estimate due to the lack of understanding of the cloud-aerosol interaction (Meehl et al. 1996; Boucher

1995; Boucher and Lohmann 1995; Erickson III et al. 1995; Jones et al. 1994).

In this chapter the direct effect of anthropogenic smoke aerosol is considered. Specific features of this investigation are (a) derivation of the change of planetary albedo due to an aerosol layer that includes absorbing properties of aerosols and (b) Mie scattering calculation of the smoke particle backscattering fraction that shows a strong dependence on the aerosol size distribution.

2.2 Aerosol Radiative Forcing

At a given level in the atmosphere, the aerosol radiative forcing is defined as the change in the net downward radiative flux at that level due to the introduction of the aerosol into the atmosphere. The globally averaged aerosol radiative forcing at the top of the atmosphere due to the direct effect of aerosols, ΔF_R, was calculated by Charlson et al. (1992) using the expression

$$\Delta F_R = -\frac{S_0}{4}T_a^2(1 - N)(1 - a)^2 2\beta\tau_{sc}^* \tag{2.1}$$

where S_0 is the solar constant, T_a is the transmittance of the atmosphere above the aerosol layer, N is the fraction of sky covered by clouds, a is the albedo of the under-lying surface, β is the backscattering fraction which indicates the fraction of radiation scattered by aerosol into the upper hemisphere, and τ_{sc}^* is the aerosol layer scattering optical thickness. The physical meaning of individual factors in equation 2.1 is the following: $S_0/4$ is the globally averaged incident solar flux at the top of the atmosphere which has units of $W\,m^{-2}$, T_a^2 reduces the incident flux and the reflected flux by the transmittance of the atmosphere above the aerosol layer, $1 - N$ comes from the assumption that albedo changes due to aerosol is significant only in the cloud free atmosphere.

The last factor in equation 2.1

$$\Delta R = (1 - a)^2 2\beta\tau_{sc}^* \tag{2.2}$$

represents the albedo increase of the atmospheric system due to a non-absorbing aerosol layer.

To consider absorbing aerosols, the proper modifications to equation 2.2 must be found. The azimuthally independent radiative transfer equation for plane-parallel atmospheres at solar wavelengths is the starting point to extend equation 2.1 for use with absorbing aerosols.

$$\mu \frac{dI_\lambda(\mu, \tau_\lambda)}{d\tau_\lambda} = I_\lambda(\mu, \tau_\lambda) - \frac{\omega_\lambda}{2} \int_{-1}^{1} P_\lambda(\mu, \mu') \, I_\lambda(\mu', \tau_\lambda) \, d\mu' \tag{2.3}$$

where $I_\lambda(\mu, \tau_\lambda)$ is the intensity at the optical depth τ_λ (which is a unitless quantity that measures the extinction of a beam of radiation as it propagates through an atmospheric layer) and in the direction $\mu = \cos\theta$ (where θ is the zenith angle). The single scattering albedo, ω_λ, is defined as the ratio of the scattering coefficient to the extinction coefficient. $P_\lambda(\mu, \mu')$ is the azimuthally independent scattering phase function which describes the angular distribution of scattered energy. The normalization of the phase function is chosen to be

$$\frac{1}{2} \int_{-1}^{1} P_\lambda(\mu, \mu') \, d\mu' = 1 \tag{2.4}$$

The λ subscript indicates that those quantities are wavelength dependent. This subscript will be dropped from now on, to simplify notation, but the wavelength dependence is still implied.

In the two-stream approximation, the intensity is assumed to be

$$I(\mu, \tau) = \begin{cases} I^+(\tau) & \text{if } \mu > 0 \\ I^-(\tau) & \text{if } \mu < 0 \end{cases} \tag{2.5}$$

which separates equation 2.3 into two coupled equations

$$\mu \frac{dI^+(\tau)}{d\tau} = I^+(\tau) - \frac{\omega}{2} \int_{-1}^{0} I^-(\tau) P(\mu, \mu') \, d\mu' - \frac{\omega}{2} \int_{0}^{1} I^+(\tau) P(\mu, \mu') \, d\mu' \tag{2.6}$$

$$\mu \frac{dI^-(\tau)}{d\tau} = I^-(\tau) - \frac{\omega}{2} \int_{-1}^{0} I^-(\tau) P(\mu, \mu') \, d\mu' - \frac{\omega}{2} \int_{0}^{1} I^+(\tau) P(\mu, \mu') \, d\mu' \tag{2.7}$$

By integrating equation 2.6 over μ from 0 and 1, and equation 2.7 over μ from -1 to 0 these equation become

$$\frac{1}{2}\frac{dI^+(\tau)}{d\tau} = I^+(\tau) - \omega\beta I^-(\tau) - \omega(1-\beta)I^+(\tau) \qquad (2.8)$$

$$-\frac{1}{2}\frac{dI^-(\tau)}{d\tau} = I^-(\tau) - \omega(1-\beta)I^-(\tau) - \omega\beta I^+(\tau) \qquad (2.9)$$

where the backscattering fraction for isotropic radiation is

$$\beta = \frac{1}{2}\int_0^1 \int_{-1}^0 P(\mu,\mu')\,d\mu'\,d\mu \qquad (2.10)$$

These differential equations are coupled. By differentiating one of the equations by τ and substituting that result into the other equation, the solutions can be found to be of the form

$$I^+(\tau) = A_1\exp(\alpha\tau) + A_2\exp(-\alpha\tau) \qquad (2.11)$$

$$I^-(\tau) = A_3\exp(\alpha\tau) + A_4\exp(-\alpha\tau) \qquad (2.12)$$

where $\alpha^2 = 4(1-\omega)(1-\omega+2\beta\omega)$. The coefficients A_1, A_2, A_3, and A_4 can be determined with the boundary conditions that the downward intensity at the top of the layer is given by $I^-(0) = I_0$ and the upward intensity at the bottom of the layer is $I^+(\tau^*) = I_R$ where τ^* is optical thickness of the layer. These equations must also satisfy the differential equations 2.8 and 2.9. The change in the albedo of the system with the introduction of the aerosol layer is given by (Chýlek and Coakley 1974)

$$\Delta R = R' - a \qquad (2.13)$$

$$= \frac{I^+(0)}{I^-(0)} - \frac{I^+(\tau^*)}{I^-(\tau^*)} \qquad (2.14)$$

$$= \frac{(1-a)^2\omega\beta - 2a(1-\omega)}{(1-\omega) + (1-a)\omega\beta + \frac{\alpha}{2\tanh(\alpha\tau^*)}} \qquad (2.15)$$

Noting that for small arguments $\tanh(x) \to x$, equation 2.15 can be simplified for case of optically thin aerosol layers ($\tau^* \lesssim 1$). To first order in τ^* equation 2.15 reduces to

$$\Delta R = 2\tau^*[(1-a)^2\omega\beta - 2a(1-\omega)] \qquad (2.16)$$

Replacing $(1 - \omega)\tau^*$ by the absorption optical depth τ^*_{abs} and $\omega\tau^*$ by the scattering optical depth τ^*_{sc}, the change in the albedo is

$$\Delta R = (1 - a)^2 2\beta\tau^*_{sc} - 4a\tau^*_{abs} \qquad (2.17)$$

Thus the equation 2.1 is modified to a more general form valid also for absorbing aerosols

$$\Delta F_R = -\frac{S_0}{4}T_a^2(1 - N)[(1 - a)^2 2\beta\tau^*_{sc} - 4a\tau^*_{abs}] \qquad (2.18)$$

For a non-absorbing aerosol $\tau^*_{abs} = 0$ and equation 2.18 reduces to the equation 2.1 used by Charlson et al. (1992) for the case of non-absorbing sulfate aerosols. However, for absorbing aerosols the second term cannot be, generally, neglected.

Although the aerosol direct forcing can be determined by solving a more accurate form of radiation transfer model (Coakley et al. 1983), the advantage of an analytical solution in the form of equation 2.18 is an explicit dependence on the individual parameters determining the forcing. Note that the first term (the scattering term) on the right hand side of equation 2.17 depends on the aerosol backscattering fraction, β, while the the second term is independent of β.

2.3 Climate Forcing of Smoke Aerosols

The backscattering fraction β is a sensitive function of particle size. It is equal to 0.5 for small particles in the regime of Rayleigh scattering and it decreases with increasing size of aerosol particles. The choice of particle size distribution and the corresponding value of the backscattering fraction is crucial for the estimate of aerosol direct climate forcing.

Aerosol particles produced by biomass burning have a wide range of sizes. Aerosol particles produced by fires will grow at ambient relative humidity to larger equilibrium sizes. The range of observed particle radii (Mulholland and Ohlemiller 1982; Helsper et al. 1980; Woods et al. 1991; Cachier et al. 1991; Einfeld et al. 1991) is from

0.01 μm to about 5 μm. Radke (1991) observe three distinct modes of biomass burning aerosols: nucleation mode with radii below 0.05 μm, accumulation mode with radii 0.05 μm $< r < 1.0 \mu$m and coarse mode with radii above 1 μm. The accumulation mode dominates aerosol mass and aerosol light scattering properties (Radke 1991). Similar distribution of sizes is found by Holben et al. (1991) who use the lognormal size distribution to describe the biomass burning aerosols.

To investigate the dependence of aerosol direct forcing on the aerosol size distribution, the lognormal size distribution of the form

$$\frac{dN}{dr}(r) = \frac{N_0}{\sqrt{2\pi}\, r \ln \sigma_0} \exp\left[-\frac{\ln^2(\frac{r}{r_0})}{2 \ln^2 \sigma_0}\right]$$

(2.19)

is used with the geometric mean radius, r_0, between 0.05 μm and 0.30 μm and with standard deviation $\ln \sigma_0$ between 0.3 and 0.7. A useful quantity that can be calculated for any size distribution, regardless of the analytical form used to describe it, is the effective radius. Distributions with the same effective radius tend to have similar optical characteristics. The effective radius is defined as

$$r_{eff} = \frac{\int_0^\infty r^3 \frac{dN}{dr}\, dr}{\int_0^\infty r^2 \frac{dN}{dr}\, dr}$$

(2.20)

which can be integrated for the lognormal distribution to

$$r_{eff} = r_0 \exp\left(\frac{5}{2} \ln^2 \sigma_0\right)$$

(2.21)

The effective radius of the distributions being considered changes from 0.06 μm to 1.02 μm, which is within the range of the observed effective radii from fresh to aged biomass burning aerosols as given by Holben et al. (1991) and Radke (1991).

Several refractive indices with real parts between 1.33 and 1.43 and imaginary parts between 0.0035 and 0.0115 (Holben et al. 1991) are used to calculate the asymmetry parameter (g) with Mie theory. The asymmetry parameter is defined as the average cosine of the scattering angle weighted by the scattering phase function. The dependence of g on the refractive index (within the stated limits) was found weak compared to the dependence on the effective radius of the size distribution.

The backscattering fraction is calculated using an approximate relation (Sagan and Pollack 1967)

$$\beta = \frac{1 - g}{2} \tag{2.22}$$

which for the considered sizes of aerosol particles is close to the backscattering fraction for an average $60°$ solar zenith angle (Wiscombe and Grams 1976). For the smallest fresh biomass burning aerosols ($r_0 = 0.05\,\mu$m) $\beta = 0.37$, while for the large size end of the aged biomass burning aerosols ($r_0 = 0.30\,\mu$m) $\beta = 0.11$. Figure 2.1 plots the backscattering fraction for all the size distributions and refractive indices considered as functions of the geometric mean radii of the size distributions. This figure shows that for a given r_0, β decreases as $\ln \sigma_0$ increases. This is because the wider distributions include higher numbers of larger-sized particles which have lower backscattering fractions.

The backscattering fraction of the absorbing aerosols is replotted in figure 2.2 as functions of effective radius. Size distributions with different r_0 and $\ln \sigma_0$ that have similar effective radii, r_{eff}, have similar backscattering fractions. This is consistent with the effective radius being the most suitable variable characterizing the scattering properties of particle polydispersion (Hansen and Travis 1974; Damiano and Chýlek 1994).

To isolate the effect of smoke aerosol size distribution on the climate forcing all other parameters are kept constant with values taken from Penner et al. (1992). Thus the absorption and the scattering optical thickness of a smoke layer are $\tau_{abs}^* = 0.0026$ and $\tau_{sc}^* = 0.030$ respectively, the global averaged albedo $a = 0.22$ over the land and $a = 0.06$ over the ocean with 80% of aerosols being over the land; the solar constant is $1370\,\mathrm{W\,m^{-2}}$, the atmospheric transmittance above the aerosol layer is taken to be $T_a = 0.79$ (Penner et al. 1992) and cloudiness $N = 0.6$. The results of direct radiative forcing calculated with equation 2.18 are shown in figure 2.3 as functions of effective radius. The biomass burning induced direct climate forcing ΔF ranges from about $-0.2\,\mathrm{W\,m^{-2}}$ for distributions with large effective radii to $-1.0\,\mathrm{W\,m^{-2}}$ for the distributions with effective radii of approximately $0.06\,\mu$m.
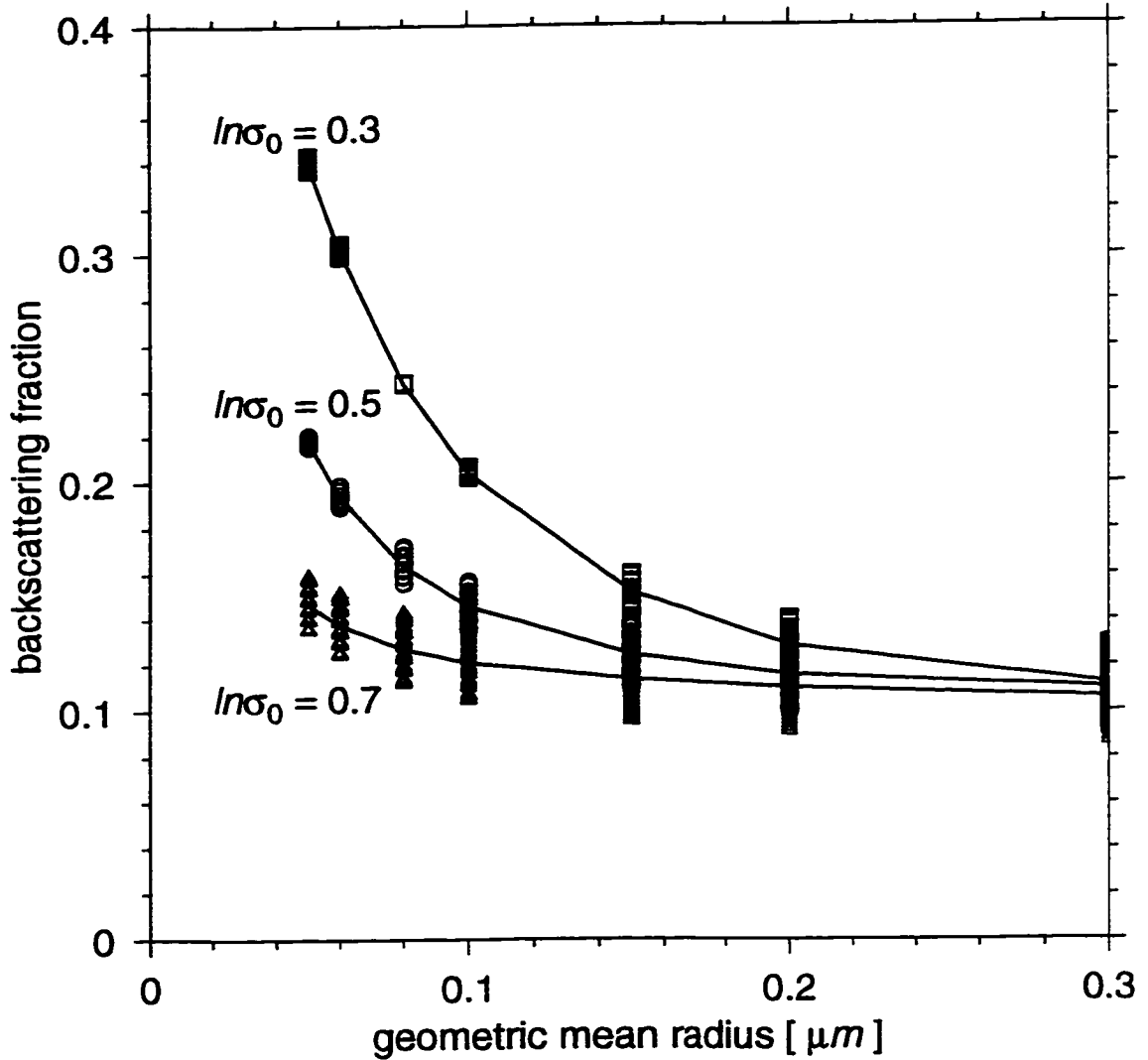
Figure 2.1: The backscattering fraction of lognormal size distributions of absorbing aerosols as functions of geometric mean radius. The $\square$, $\circ$, and $\triangle$ symbols correspond to distributions with $\ln \sigma_0 = 0.3$, 0.5, and 0.7 respectively. Refractive indices with real parts between 1.33 and 1.43 and imaginary parts between 0.0035 and 0.0115 are considered.
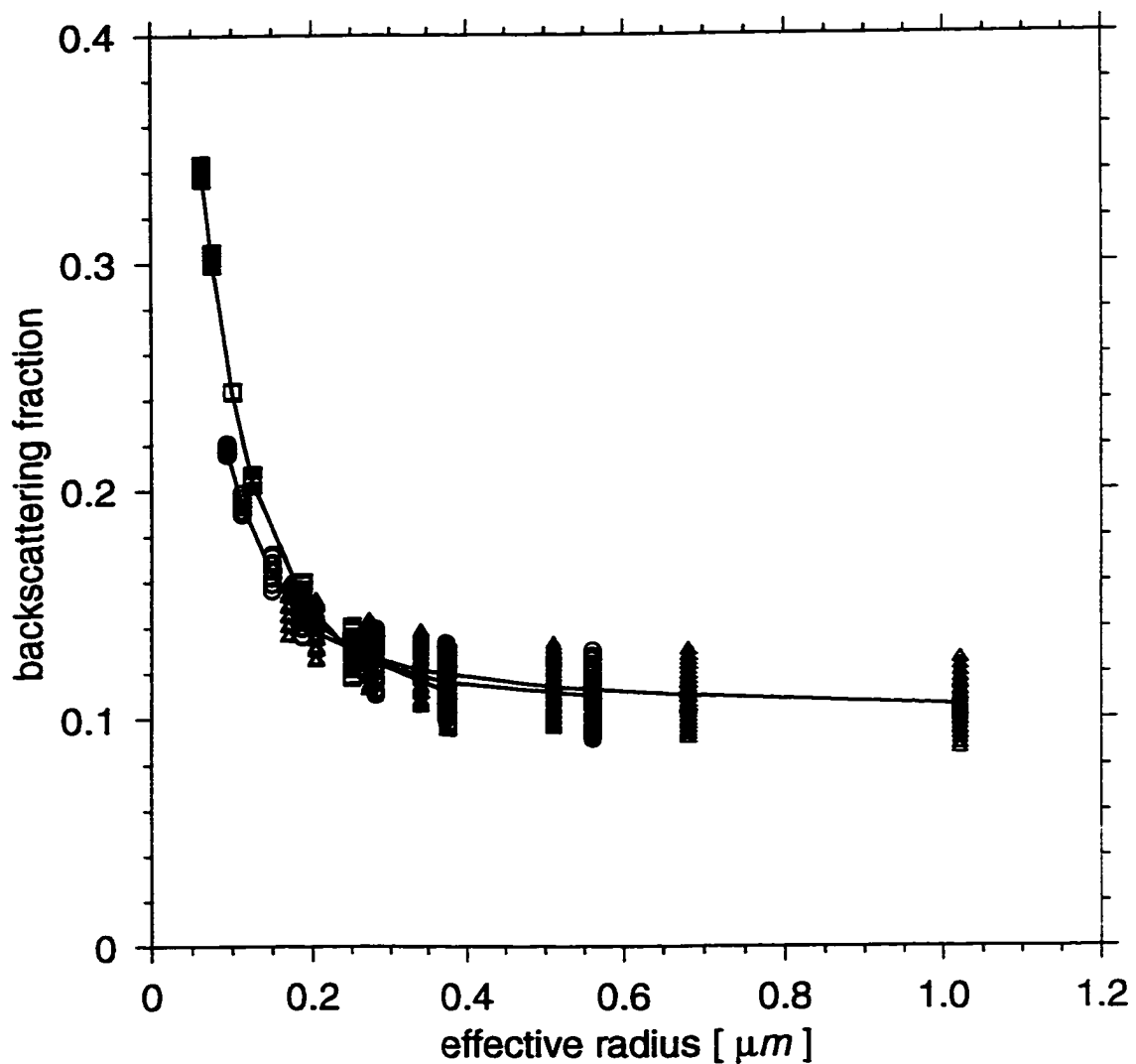
Figure 2.2: The backscattering fraction of lognormal size distributions of absorbing aerosols as functions of effective radius. The □, o, and △ symbols correspond to distributions with $\ln \sigma_0 = 0.3$, 0.5, and 0.7 respectively. Refractive indices with real parts between 1.33 and 1.43 and imaginary parts between 0.0035 and 0.0115 are considered.

Figure 2.3: The direct radiative forcing of lognormal size distributions of absorbing aerosols as functions of effective radius. The $\square$, $\circ$, and $\triangle$ symbols correspond to distributions with $\ln \sigma_0 = 0.3$, 0.5, and 0.7 respectively.

2.4   Summary

The direct radiative forcing of an optically thin aerosol layer is given by equation 2.18. The advantage of expression 2.18 is its simplicity and an explicit dependence of the forcing on aerosol layer optical thickness and aerosol backscattering fraction. For the case of non-absorbing aerosols equation 2.18 is reduced to the form used previously by Charlson et al. (1992) and Penner et al. (1992).

The aerosol backscattering fraction is a sensitive function of aerosol size distribution. Considering measurements of aerosol size distributions produced by biomass burning (Mulholland and Ohlemiller 1982; Helsper et al. 1980; Woods et al. 1991; Cachier et al. 1991; Einfeld et al. 1991; Radke 1991; Holben et al. 1991) the direct radiative forcing due to smoke aerosols varies between $-0.2\,\mathrm{W\,m^{-2}}$ and $-1.0\,\mathrm{W\,m^{-2}}$ depending on the size distribution used. The distributions with smaller effective radii result in stronger radiative forcing. A similar dependence on size distribution of radiative effects of sulfate aerosols was pointed out by Kiehl and Briegleb (1993). This range of uncertainty can be reduced by additional field measurements and modeling of the smoke aerosol size distribution and its changes with relative humidity. The result of Penner et al. (1992) of radiative forcing $-0.8\,\mathrm{W\,m^{-2}}$ (when absorption was accounted for) is reproduced with size distribution with $r_{eff} = 0.08\,\mu\mathrm{m}$.

The direct aerosol radiative forcing was considered only in the cloud free portion of the atmosphere in a similar way was done by Charlson et al. (1992) and Penner et al. (1992). Coakley et al. (1983) considered climate forcing of tropospheric aerosols including the cloudy part of the atmosphere. His results suggest that inclusion of aerosol forcing over the cloudy part of the atmosphere increases the direct aerosol forcing by 20 to 25%.

Chapter 3

Growth of Hygroscopic Aerosols

3.1   Introduction

Atmospheric aerosols affect the radiative energy balance of the planet in two ways. The indirect radiative effect of aerosol refers to the change in the radiative forcing of clouds either by the lifetime of the clouds, or by the size distribution and chemistry of the droplets that make up the cloud (Twomey 1974: Twomey 1977: Twomey et al. 1984). How the aerosols themselves absorb and scatter radiation is called the direct radiative effect (Charlson et al. 1992). A considerable amount of attention has been paid to the climatic impact of sulfuric acid, ammonium sulfate, and ammonium bisulfate aerosols (Pilinis et al. 1995; Boucher and Anderson 1995; Nemesure et al. 1995; Russell et al. 1996). These sulfate aerosols are of interest because of the increase in their atmospheric concentration due to the increase in sulfur containing gas emissions from human industrial activities (Charlson and Wigley 1994). Sea salt aerosols are also of interest since they are the dominant kind by mass over the oceans (Winter and Chýlek 1997; Gong et al. 1997).

Sulfate and sea salt aerosols are hygroscopic in nature — meaning water vapor readily condenses on them resulting in an increase in particle size depending on the ambient relative humidity. Measurements indicate that the mass of the particle can increase by over a factor of four if the relative humidity is greater than 0.90 (Tang

1997; Tang and Munkelwitz 1994). This increase in size changes the optical properties of these particles. Before the radiative effect of hygroscopic aerosols can be determined, the growth of these particles with relative humidity must be known.

In this chapter, the Köhler equation is discussed. This equation gives the increase in particle size as a function of relative humidity. One of the parameters in this equation is the van't Hoff factor which accounts for the nonideality of the solution and which measurements show to be a function of solute concentration (Low 1969). Because of this, modifications to the Köhler equation have been suggested (Young and Warren 1992) but calculations using this modified equation disagree with measurements whereas calculations using the original Köhler equation are in agreement. Reasons for this are presented. Comparisons are also made with calculations where the Köhler equation is used with a constant value of the van't Hoff factor and when using Gerber's parameterization for particle growth (Gong et al. 1997; Gerber 1985). The Köhler equation is then used to predict the change in size distributions of hygroscopic aerosols.

The results from this chapter will be used in chapter 4 to calculate the optical properties and the radiative forcing of hygroscopic aerosols as functions of relative humidity.

3.2   Köhler Equations

The equation governing the growth of aerosols with relative humidity and activation of cloud droplets is generally known as the Köhler equation (Köhler 1936; Rogers and Yau 1989; Pruppacher and Klett 1997). The erroneous use of this phase equilibrium condition has a long history. Howell (1949) in his work on cloud droplets growth did not include the van't Hoff factor. McDonald (1953) pointed out the error. Low (1969) calculated values of the van't Hoff factor from tables of mean ionic activities for different concentrations of solutions consisting of various salts. Low (1969) also implied that a variable van't Hoff factor should be used in the Köhler equation for

cloud and aerosol physics applications.

Reiss (1950) and Doyle (1961) derived a modified Köhler equation that contains a term proportional to the partial derivative of the droplet surface tension with respect to the droplet composition. Young and Warren (1992) derived the modified Köhler equation that also contains the derivative of the van't Hoff factor with respect to concentration.

Analytical arguments suggesting that the modified Köhler equation derived by Young and Warren (1992) is not correct are presented and that the original Köhler equation is the proper equation for applications in cloud and aerosol physics. These conclusions are supported by comparing theoretical calculations with laboratory measurements.

3.2.1 Raoult's law, van't Hoff factor, and water activity

Raoult's law describes the changes in equilibrium vapor pressure over a flat surface of solution as a function of solute concentration (Rogers and Yau 1989: Adkins 1983: Pruppacher and Klett 1997)

$$\frac{p'_\infty}{p_\infty} = \frac{n_L}{n_L + n'_L} \tag{3.1}$$

where p'_∞ and p_∞ are, respectively, the equilibrium vapor pressure over a flat surface of solution and over a flat surface of pure water, and n_L and n'_L are the number of moles or molecules of solvent (water) and solute (dissolved salt) present in the solution, respectively. Equation 3.1 is used to define an ideal solution (Hobbs 1995).

An empirical coefficient, the van't Hoff factor i, is introduced to account for non-ideal characteristics of real solutions. Non-ideal effects include partial dissociation, and ion-ion and ion-water interactions. Equation 3.1 is modified to

$$\frac{p'_\infty}{p_\infty} = \frac{n_L}{n_L + i\,n'_L} \tag{3.2}$$

where the van't Hoff factor is considered to be an empirical function of the concentration.

Except for the van't Hoff factor, the right hand side of equation 3.2 is known from the composition of the solution. The left hand side can be measured experimentally. The experimental values, giving the fractional decrease of the equilibrium vapor pressure due to a definite amount of solute present in the solution, are generally known as water activities of the considered solution (Pruppacher and Klett 1997). The water activity, a_w, is thus given by

$$\frac{p'_\infty}{p_\infty} = a_w(M) \tag{3.3}$$

where the dependence on solution concentration will be expressed in terms of molality, M (moles of solute per kilogram of solvent).

It is the water activity that is usually measured experimentally. From the water activity other quantities of interest can be calculated. A useful expression for the van't Hoff factor i as a function of solute concentration and water activity can be obtained from equations 3.2 and 3.3 in the form

$$
\begin{aligned}
i &= \frac{n_L(1 - a_w)}{n'_L a_w} \\
&= \frac{m_w M_s(1 - a_w)}{m_s M_w a_w} \\
&= \frac{1000\,(1 - a_w)}{M M_w a_w}
\end{aligned}
\tag{3.4}
$$

where m_s and M_s are the mass and the molecular weight of the solute, m_w and M_w are the mass and the molecular weight of the solvent (water) and M is the molality of the solution. Equation 3.4 was used by Low (1969) and by Young and Warren (1992) to calculate the van't Hoff factor from the water activity, a_w.

Figure 3.1 plots the van't Hoff factor of ammonium sulfate ($(NH_4)_2SO_4$) solutions as a function of solute mass fraction obtained from equation 3.4 with the water activity measurements reported by several groups (Tang and Munkelwitz 1994; Chan et al. 1992; Liang and Chan 1997; Cohen et al. 1987). The relative difference between the van't Hoff factors obtained from the different research groups is within 20% relative to the Tang and Munkelwitz (1994) values. Since water activity measurements for
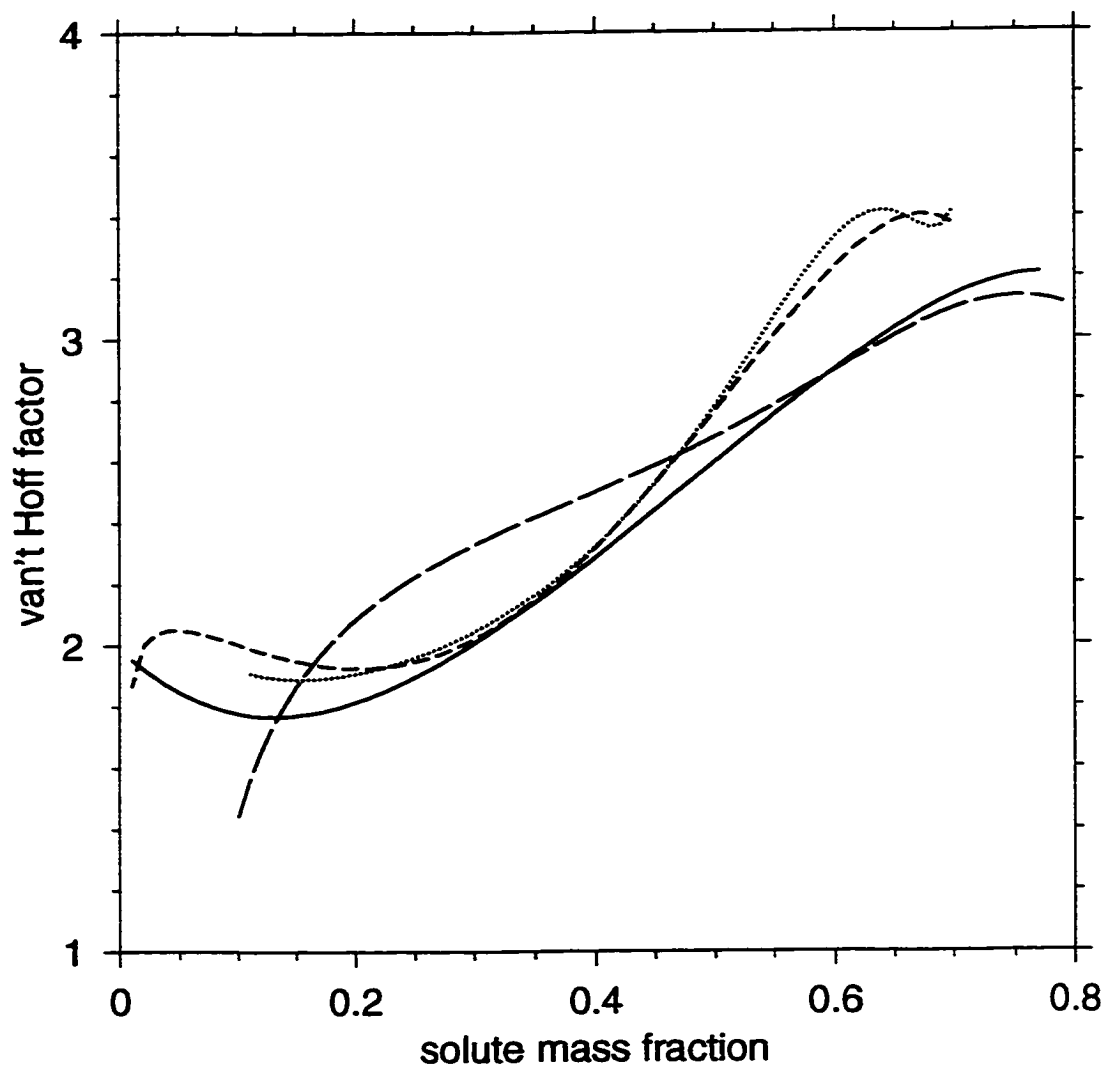
Figure 3.1: van't Hoff factor of $(NH_4)_2SO_4$ as a function of mass solute fraction obtained from measurements from Tang and Munkelwitz (1994) (solid line), Chan et al. (1992) (short dashed line), Liang and Chan (1997) (long dashed line), and Cohen et al. (1987) (dotted line).

sulfuric acid, ammonium bisulfate, nitric acid, and sea salt solutions have also been reported by the research group lead by Tang (Tang et al. 1997; Tang 1996; Tang and Munkelwitz 1994) which are also of atmospheric interest, their values are used exclusively in the following calculations.

3.2.2 Phase equilibrium condition

To distinguish between various quantities referring to the vapor or the liquid phase, the subscript V is used for vapor and L is used for liquid. In thermodynamic equilibrium, the chemical potential, $\mu_V(T, p)$, of a water vapor molecule in air at temperature T and the water vapor pressure p, has to be equal to the chemical potential, $\mu_L(T, p_L)$, of a water molecule inside the solution droplet at the pressure p_L:

$$\mu_V(T, p) = \mu_L(T, p_L) \tag{3.5}$$

The appropriate chemical potentials can be written as (Adkins 1983; Callen 1985)

$$\mu_V(T, p) = \mu_L^0(T, p_\infty) + k_B T \ln\left(\frac{p}{p_\infty}\right) \tag{3.6}$$

and

$$\mu_L(T, p_L) = \mu_L^0(T, p) + 2\frac{\sigma\nu}{r} + k_B T \ln(a_w) \tag{3.7}$$

where p_∞ is an equilibrium pressure over a flat surface of pure solvent, k_B is the Boltzmann constant, σ is the surface tension of the solution droplet, ν is a partial molecular volume of solvent in the drop, μ_L^0 is the chemical potential of pure solvent liquid, and a_w is the water activity.

Substituting for the chemical potentials into equation 3.5 and neglecting the small term, $\mu_L^0(T, p) - \mu_L^0(T, p_\infty)$, for water molecules in liquid (Reiss and Koper 1995), the equilibrium condition is obtained in a form of the Köhler equation

$$\frac{p}{p_\infty} = a_w \exp\left(\frac{2\sigma M_w}{r \rho_w R^* T}\right) \tag{3.8}$$

after replacing $\nu = M_w \rho_w^{-1} N_A^{-1}$, where ρ_w is the density of the solvent and N_A is Avogadro's number. The universal gas constant is $R^* = N_A k_B$.

A more formal derivation in line with the general structure of equilibrium thermodynamics is to look for an extreme in an appropriate thermodynamic potential. In the case of phase transition at given temperature and pressure, the corresponding thermodynamic potential is Gibbs free energy (Adkins 1983; Callen 1985). The Gibbs free energy of a solution droplet surrounded by the vapor of its constituents may be written in the form

$$G(T,p) = n_L \mu_L(T,p) + n_L' \mu_L'(T,p) + n_V \mu_V(T,p) + n_V' \mu_V'(T,p) + \sigma A$$

$$(3.9)$$

where all quantities are evaluated at ambient temperature and pressure. n_L and n_V are the number of molecules of water (solvent) in the liquid and vapor phase, n_L' and n_V' are the corresponding numbers of molecules of solute. μ_L and μ_L' are chemical potentials of solvent and solute in the drop and μ_V and μ_V' are the corresponding chemical potentials in the vapor phase; A is the surface area of the solution and σ is its surface tension.

The partial derivative of the Gibbs free energy with respect to a suitable concentration variable determines the equilibrium condition and the sign of the second partial derivative determines the nature of the equilibrium (stable or unstable equilibrium). This procedure is more general than the one used above in the derivation of the equilibrium condition 3.8, however, it also provides more opportunities to obtain inaccurate results when various terms appearing in the equations are not treated in a consistent manner. In this way, several forms of modified Köhler equations have been derived (Reiss 1950; Doyle 1961; Young and Warren 1992) in the past.

It is assumed that the salt molecules are limited to the liquid phase so that $n_V' = 0$. Additional constraints are: $\partial n_L / \partial n_V = -1$ (the total number of water molecules is a constant), $\partial n_L' / \partial n_L = 0$ (salt is limited to the liquid phase) and $\partial \mu_V / \partial n_L = 0$ (the chemical potential of water molecules in vapor is a function of T and p only). By taking the partial derivative of the Gibbs free energy with respect to the number of

water molecules in the droplet, and using the above given constraints the following equation is obtained

$$
\begin{aligned}
\left(\frac{\partial G}{\partial n_L}\right) =& \mu_L(T,p) - \mu_V(T,p) + \sigma\frac{\partial A}{\partial n_L} \\
&+ n_L\frac{\partial \mu_L(T,p)}{\partial n_L} + n_L'\frac{\partial \mu_L'(T,p)}{\partial n_L} + A\frac{\partial \sigma}{\partial n_L}
\end{aligned}
\tag{3.10}
$$

When the partial derivative of the Gibbs free energy is set to zero, and only the first three terms on the right hand side of equation 3.10 are kept, the result is the standard form of the Köhler equation 3.8.

The last term in equation 3.10 contains the partial derivative of surface tension with respect to the concentration variable. When this term is retained the modified Köhler equation containing the term $\partial\sigma/\partial n_L$ is obtained (Reiss 1950; Doyle 1961). Theoretical results obtained using such a modified Köhler equation are in disagreement with experimental measurements (Flageollet et al. 1980; Wilemski 1988).

The water molecule chemical potential μ_L is a function of water activity, a_w, and thus it can be considered to be a function of the van't Hoff factor, i. Consequently the term $\partial\mu_L/\partial n_L$ in equation 3.10 contains the derivative of the van't Hoff factor with respect to the droplet composition variable. The terms containing a derivative of the surface tension and of the van't Hoff factor were retained by Young and Warren (1992) in the derivation of their version of the modified Köhler equation.

However, in a thermodynamically consistent treatment Wilemski (1984) and Reiss and Koper (1995) demonstrated that the last three terms on the right hand side of equation 3.10 will cancel each other. The Gibbs-Duhem identity for this situation states that

$$
n_{L,b}\frac{\partial \mu_L(T,p)}{\partial n_L} + n_{L,b}'\frac{\partial \mu_L'(T,p)}{\partial n_L} = 0
\tag{3.11}
$$

where $n_{L,b}$ and $n_{L,b}'$ is the number of solvent and solute molecules, respectively, that is in the bulk phase of the drop and not on the surface of the drop. The Gibbs adsorption equation relates the number of solvent molecules on the surface, $n_{L,s}$, and

the number of solute molecules on the surface, $n'_{L,s}$.

$$n_{L,s}\frac{\partial\mu_L(T,p)}{\partial n_L} + n'_{L,s}\frac{\partial\mu'_L(T,p)}{\partial n_L} = -A\frac{\partial\sigma}{\partial n_L} \tag{3.12}$$

The sum of equations 3.11 and 3.12 results in

$$n_L\frac{\partial\mu_L(T,p)}{\partial n_L} + n'_L\frac{\partial\mu'_L(T,p)}{\partial n_L} = -A\frac{\partial\sigma}{\partial n_L} \tag{3.13}$$

Thus, setting $\partial G/\partial n_L = 0$ and using equations 3.10 and 3.13, the original Köhler equation 3.8 is recovered. The correction terms obtained by Young and Warren (1992) cancel each other out. The same conclusion was reached recently by Konopka (1996). Consequently, it is the Köhler equation 3.8 that provides the correct equilibrium condition for the solution droplet in both, the supersaturated and subsaturated water vapor pressures.

3.2.3 Numerical results and experimental measurements

To compare results predicted by the Köhler equation 3.8 and by the modified Köhler equation derived by Young and Warren (1992) a solution of ammonium sulfate $((NH_4)_2SO_4)$ in water is considered with a dry radius of $0.025\,\mu m$. Figure 3.2 shows the relative humidity as a function of solution droplet radius for relative humidities slightly above 1.0. The solid curve is for the Köhler equation 3.8 with the van't Hoff factor as a function of molality as given by Tang and Munkelwitz (1994). The dotted line is for the Köhler equation 3.8 with the constant van't Hoff factor ($i = 3$), and the dashed curve is for the case of the modified Köhler equation suggested by Young and Warren (1992) that contains the additional derivative of the van't Hoff factor. Results displayed in figure 3.2 are similar to those obtained by Young and Warren (1992).

Young and Warren (1992) assumed that the modified Köhler equilibrium curve (dashed line in figure 3.2) is the correct solution. They observed that the Köhler equation 3.8 with a constant van't Hoff factor $i = 3$ (dotted line in figure 3.2) is very close to the modified Köhler equation results, while the Köhler equation 3.8
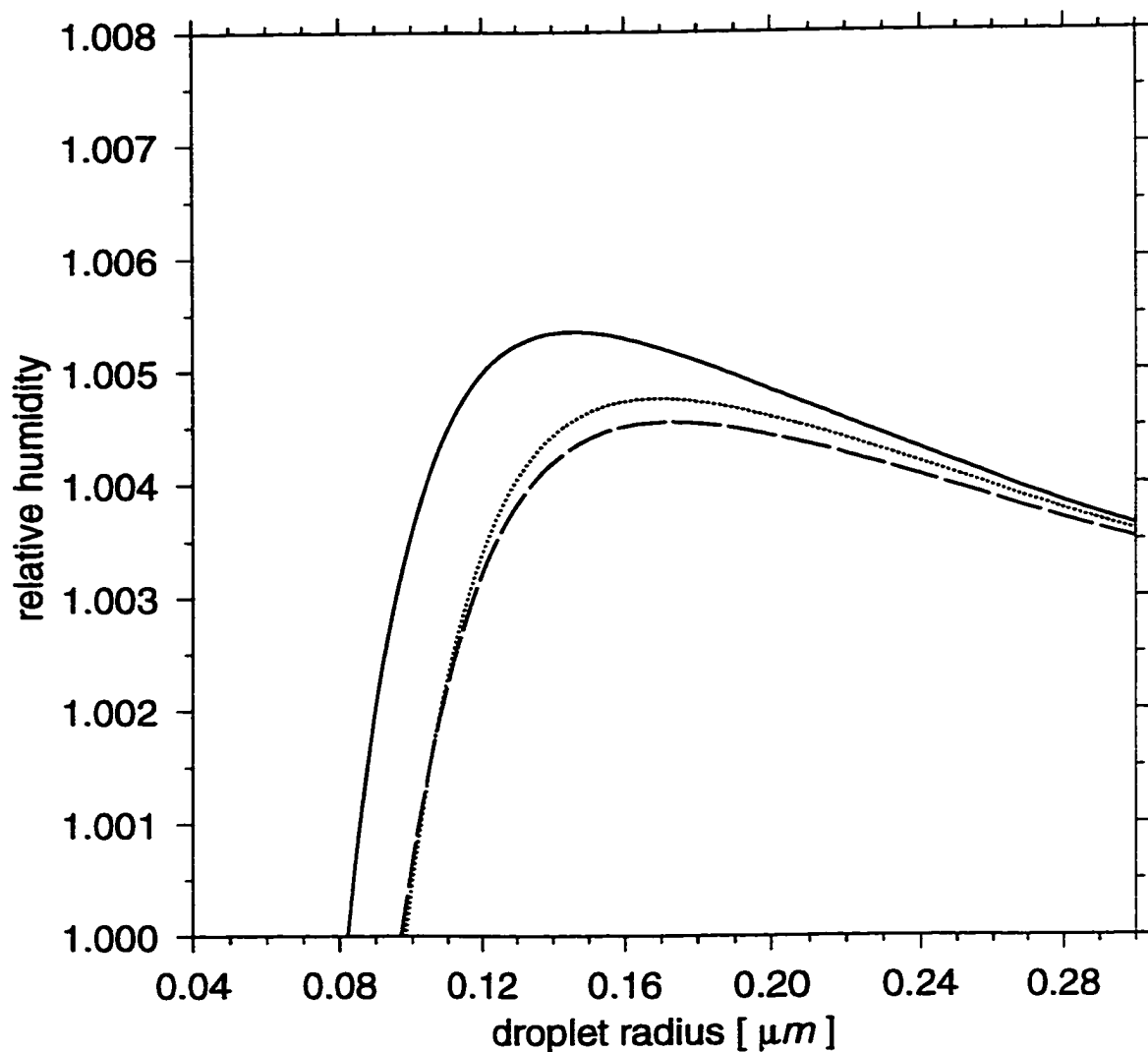
Figure 3.2: The relative humidity of an $(NH_4)_2SO_4$ aerosol with a dry radius of 0.025 μm as a function of particle radius. The dotted line is obtained from the Köhler equation with a constant $i = 3.0$. The solid line uses the van't Hoff factor from Tang and Munkelwitz (1994) in the Köhler equation. The dashed line used the modified Köhler of Young and Warren (1992).

with a concentration dependent van't Hoff factor i (solid line in figure 3.2) deviates considerably from the modified Köhler equation results. They concluded that it is better for cloud physics applications to consider i to be a constant equal to its assumed value at infinite dilution ($i = 3$ for $(NH_4)_2SO_4$), rather than take i to be a function of molality, as suggested by McDonald (1953) and Low (1969). Unfortunately, at that time there were no sufficiently accurate measurements at supersaturated vapor pressure that could be used to show which of the theoretical results was correct.

With the development of laser and electromagnetic levitation of individual droplets (Ashkin and Dziedzic 1977; Chýlek et al. 1978; Chýlek et al. 1983; Fung et al. 1987), it became possible to accurately measure the mass of individual levitated droplets as a function of relative humidity. Tang and Munkelwitz (1994) measured the mass of liquid water condensed on an individual ammonium sulfate particle as a function of relative humidity. Their results of the mass growth factor (the ratio of total aerosol mass to the dry aerosol mass) are shown as ● symbols in figure 3.3. The mass of the $(NH_4)_2SO_4$ aerosol remains unchanged as it is exposed to an increasing relative humidity, until the deliquescence point at about 0.80 is reached. The condensed water dissolves $(NH_4)_2SO_4$ and the solution droplet continues to grow with increasing relative humidity. When relative humidity is decreased, the solution droplet evaporates until the recrystallization point around 0.37 is reached. This set of measurements provides a suitable set of results against which the Köhler equation 3.8 and modified Köhler equation (Young and Warren 1992) can be tested.

Figure 3.3 shows the experimental measurements together with numerical results obtained using the modified Köhler equation of Young and Warren (1992) (short dashed line), the Köhler equation 3.8 with a variable van't Hoff factor (solid line), and the Köhler equation with a constant $i = 3$ (dotted line). The measurements of water activity by Tang and Munkelwitz (1994) are used to calculate the van't Hoff factor for an $(NH_4)_2SO_4$ solution using the equation 3.4. It is the Köhler equation 3.8, with the variable van't Hoff factor i, that provides the best agreement with experimental data. The Köhler equation with a constant van't Hoff factor, and Young
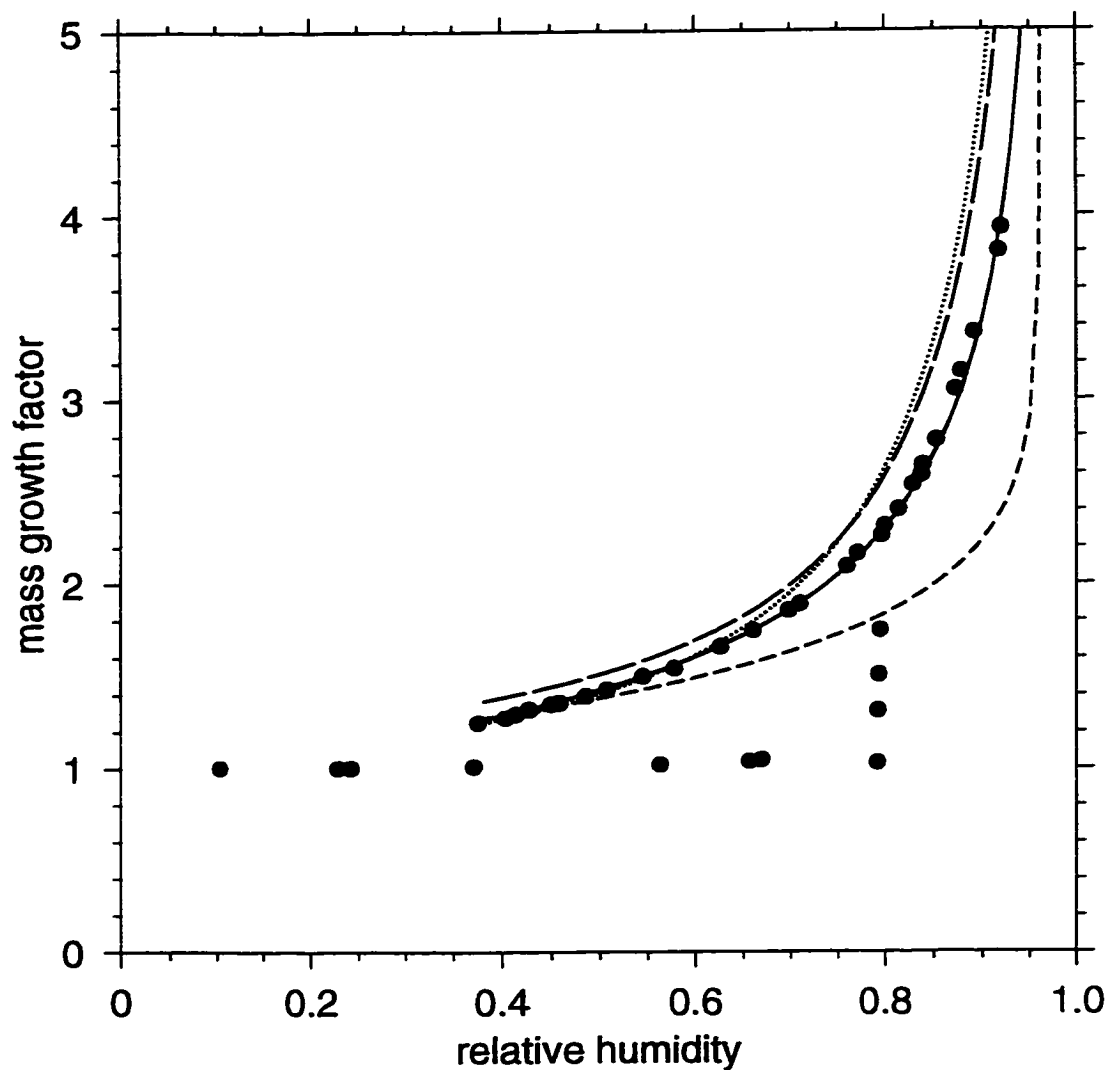
Figure 3.3: The equilibrium mass growth factor of a 10.0 μm dry radius $(NH_4)_2SO_4$ aerosol as a function of relative humidity. The ● symbols are the measurements of Tang and Munkelwitz (1994). Results obtained from the Köhler equation with a concentration dependent i (solid line) and a constant $i = 3.0$ (dotted line) are drawn. Values calculated with the modified Köhler equation is shown with the short dashed curve and with Gerber's parameterization with the long dashed curve.

and Warren (1992)'s modified Köhler equation lead to considerable errors at higher relative humidities. At a relative humidity of 0.85, the relative difference of using a constant i is 23%. Using Young and Warren (1992)'s leads to a relative difference of -26%.

A fourth curve is also drawn with the long dashed line in figure 3.3. This curve is obtained by using the Gerber parameterization that approximates the equilibrium radius of a drop as a function of relative humidity (Gong et al. 1997; Gerber 1985). This parameterization has the form:

$$r = [r_d^3 + \frac{C_1 r_d^{C_2}}{C_3 r_d^{C_4} - \log(rh)}]^{\frac{1}{3}} \tag{3.14}$$

where r_d is the radius of the dry particle in units of cm and the coefficients of $(NH_4)_2SO_4$ are $C_1 = 0.4809$, $C_2 = 3.082$, $C_3 = 3.110 \times 10^{-11}$, and $C_4 = -1.428$. The advantage of parameterizations such as equation 3.14 is that the the equilibrium radius is expressed explicitly as a function of relative humidity. In contrast, using the Köhler equation 3.8 to obtain the equilibrium radius for a given relative humidity is an iterative procedure because the water activity is a function of concentration and hence a function of radius as well.

The results from the Gerber equation 3.14 are similar to those obtained from the Köhler equation with a constant van't Hoff factor. Both over-predict the mass growth factor. At a relative humidity of 0.85, the relative difference of this curve relative to using the Köhler equation with a concentration dependent i is 18%. This difference increases to 40% when the relative humidity is 0.95.

The top panel of figure 3.4 shows the predicted mass growth factor for a particle with a dry radius of 0.10 μm. The equilibrium radius predicted by the Gerber parameterization under-predicts the results obtained from the Köhler equation with a variable van't Hoff factor by a relative difference -8% at 0.80 relative humidity. At approximately 0.90 relative humidity, the Gerber parameterization begins to overestimate the mass growth factor. At 0.95 relative humidity, the Gerber parameterization over-predicts the mass growth factor by 9%. For particles with a dry radius of 0.01 μm,
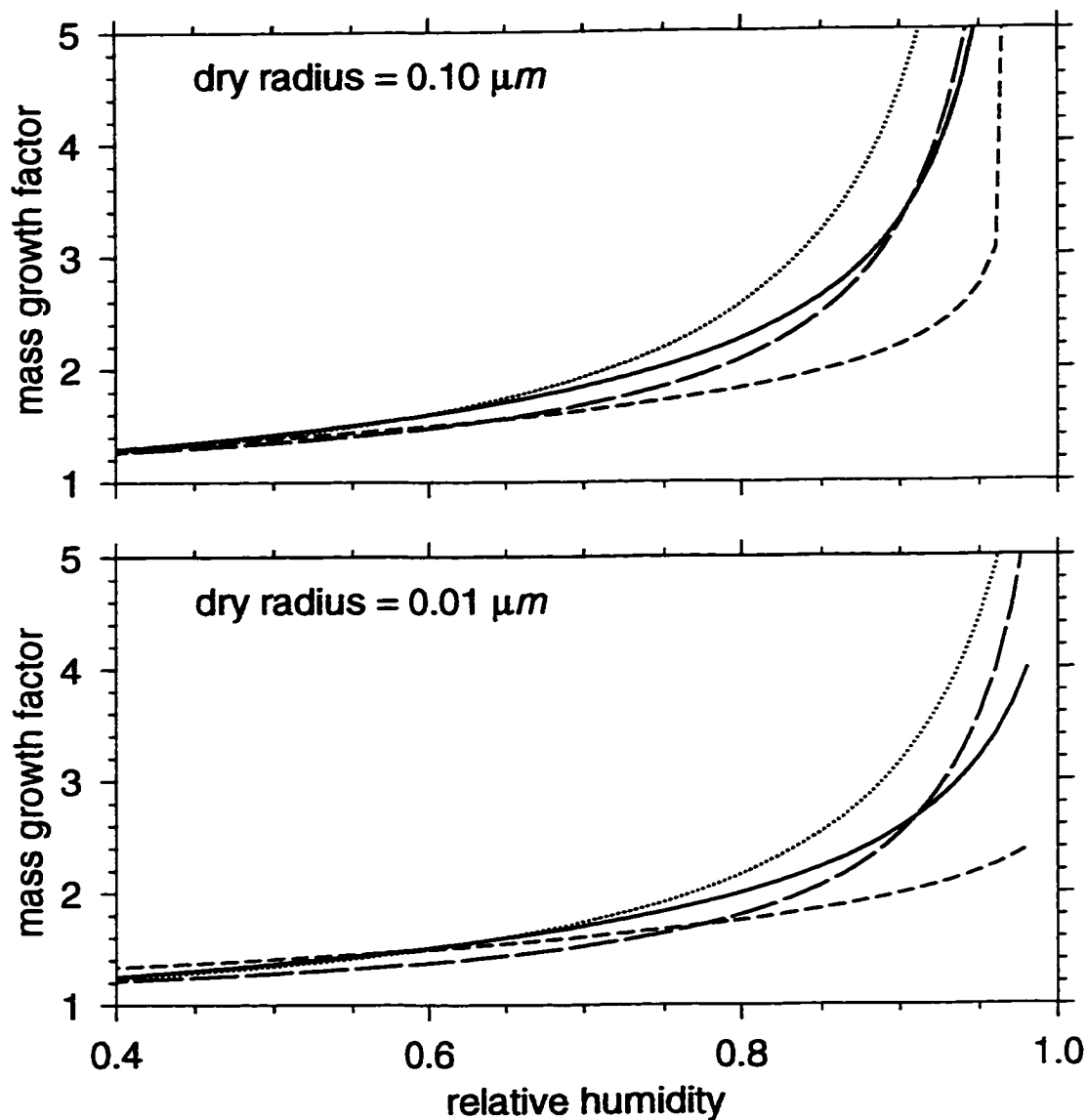
Figure 3.4: The equilibrium mass growth factor of 0.10 μm (top panel) and 0.01 μm (bottom panel) dry radius $(NH_4)_2SO_4$ aerosol as a function of relative humidity. Results obtained from the Köhler equation with a concentration dependent i (solid line) and a constant $i = 3.0$ (dotted line) are drawn. Values calculated with the modified Köhler equation are shown with the short dashed curve and with Gerber's parameterization with the long dashed curve.

the results obtained from the modified Köhler equation underestimates growth relative to the Köhler equation with a concentration dependent van't Hoff factor. When the relative humidity is 0.85 the relative difference is -16%. Using a constant $i = 3.0$ results in an overestimate in growth when the relative humidity is greater than 0.65. By 0.85 relative humidity the relative difference is 14%. For this smaller particle, the Gerber parameterization no longer produces results that are similar to using a constant van't Hoff factor in the Köhler equation. At 0.85 relative humidity, the Gerber parameterization under-predicts the mass growth factor with a relative difference of -7%; but at 0.95 relative humidity it over-predicts the growth by a relative difference of 12%.

Figure 3.5 plots the mass growth factor using the Köhler equation of sulfuric acid (H_2SO_4), ammonium bisulfate (NH_4HSO4), nitric acid (HNO_3), and ammonium sulfate aerosols that have a radius of $0.10 \mu m$ when dry. Only the descending path of the hysteresis effect is drawn. The mass growth factor for NH_4HSO_4, shown with the short dashed line, is close to the solid curve corresponding to $(NH_4)_2SO_4$. An importance difference between the two is that the crystallization relative humidity of NH_4HSO_4 is less than 0.05 compared to 0.37 for $(NH_4)_2SO_4$ (Tang 1996). The deliquescence humidity of NH_4HSO_4 is also lower at 0.69 than that of $(NH_4)_2SO_4$ (which is 0.80). Sulfuric acid aerosols are in a liquid state for all relative humidities and they have strongest mass growth of the three sulfate aerosols considered, as shown with the dotted line. The long dashed line corresponds to HNO_3 aerosols. The mass growth curve of HNO_3 is weaker than that of H_2SO_4 when the relative humidity is less than 0.60 but for higher relative humidities the mass growth factor of HNO_3 is stronger. At 0.95 relative humidity, the mass growth factor of HNO_3 is 25% larger than that of sulfuric acid.

Another aerosol type that is of atmospheric interest is sea salt aerosol. Sea salt is not a pure substance but is a mixture of NaCl, Na_2SO_4, K_2SO_4, $MgSO_4$, $Fe_2(SO_4)_3$, and $MnSO_4$ (d'Almeida et al. 1991). Sodium Chloride (NaCl) is the dominant chemical species with a mass fraction of 0.90. Aerosols with one pure chemical component
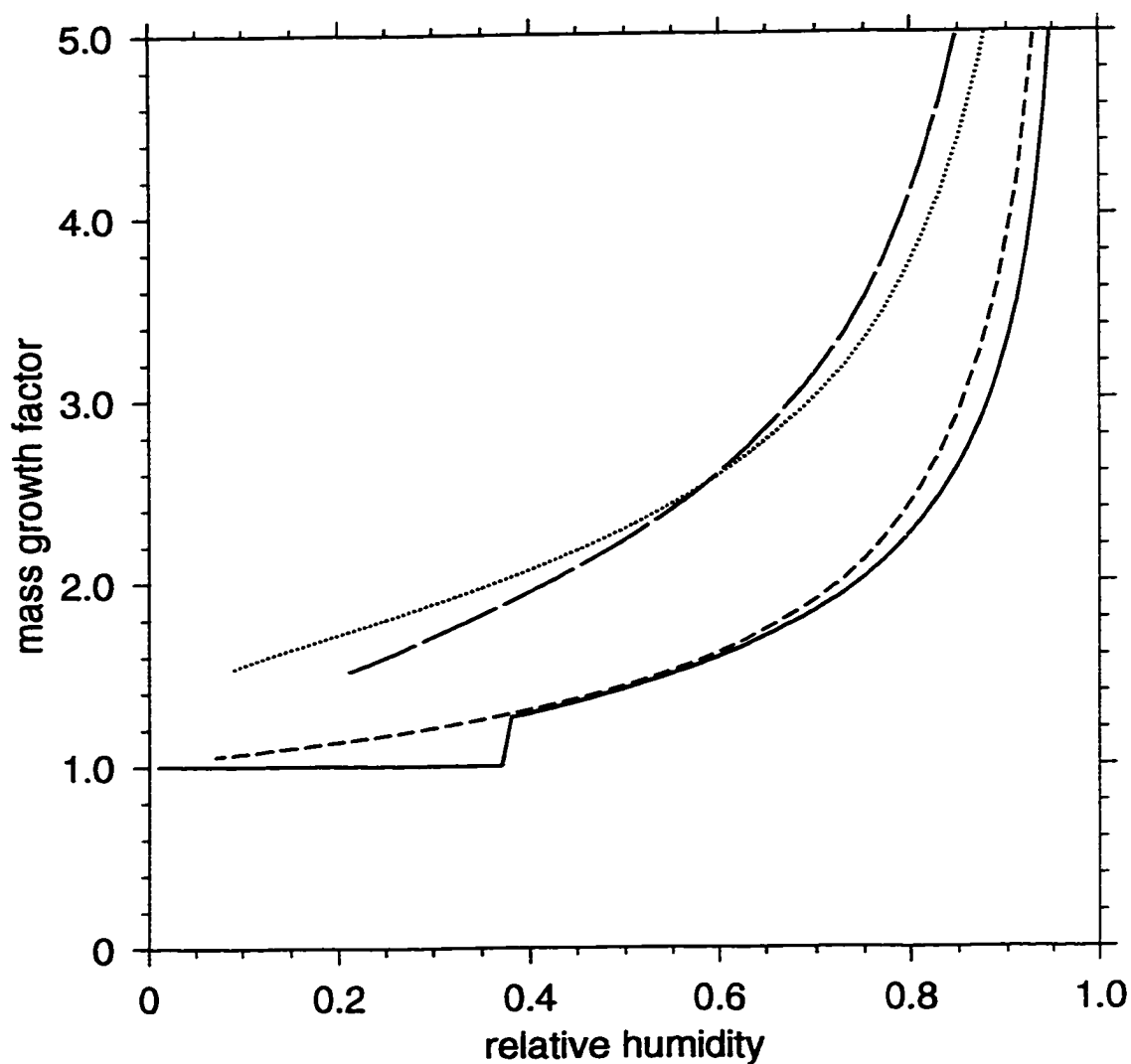
Figure 3.5: The equilibrium mass growth factor of 0.10 μm dry radius aerosols of H$_2$SO$_4$ (dotted line), NH$_4$HSO4 (short dashed line), (NH$_4$)$_2$SO$_4$ (solid line), and HNO$_3$ (long dashed line) as functions of relative humidity. The results are obtained from the Köhler equation with a concentration dependent i (Tang et al. 1988; Tang and Munkelwitz 1994; Tang 1996). Only the descending path of the hysteresis effect is drawn.

when dry, such as NaCl particles, do not increase in mass until the deliquescence relative humidity is reached. For NaCl, the deliquescence humidity is 0.75. However Tang et al. (1997) observed that the mass of sea salt particles slowly increases as relative humidity increases (below 0.75) due to components with lower deliquescence humidities that are dissolved. When the relative humidity is around 0.74, all the chemical components have dissolved and further growth behavior is similar to other one component particles. The evaporation curve of sea salt aerosols is similar to NaCl aerosols with a crystallization humidity of 0.45 that is slightly lower than the 0.47 crystallization humidity of NaCl. Unlike NaCl aerosols, sea salt aerosols are not completely dry when the humidity is less than 0.45. In subsequent calculations involving sea salt aerosols, sea salt is treated as if it were a single component particle with sharp transitions from the wet and dry states at the crystallization and deliquescence humidities of 0.45 and 0.74 but the mass density, molecular weight, and refractive index of sea salt are still used. Figure 3.6 shows the growth curve of a sea salt aerosol (solid line) with a dry radius of $10.0\,\mu$m and $0.10\,\mu$m. The dotted line in figure 3.6 corresponds to using a constant $i = 2.0$ in the Köhler equation and the dashed line are results obtained from using the Gerber parameterization for sea salt (equation 3.14). The coefficients for the Gerber parameterization corresponding to sea salt are $C_1 = 0.7674$, $C_2 = 3.079$, $C_3 = 2.572 \times 10^{-11}$, and $C_4 = -1.424$ (Gong et al. 1997). For the larger sized particle these two curves are similar to each other but both underestimate the growth predicted with the concentration dependent van't Hoff factor by a relative difference of approximately -33% at the crystallization relative humidity. When the dry sea salt aerosol size is $0.10\,\mu$m, the mass growth factor obtained by the Gerber parameterization is -37% at the crystallization relative humidity.
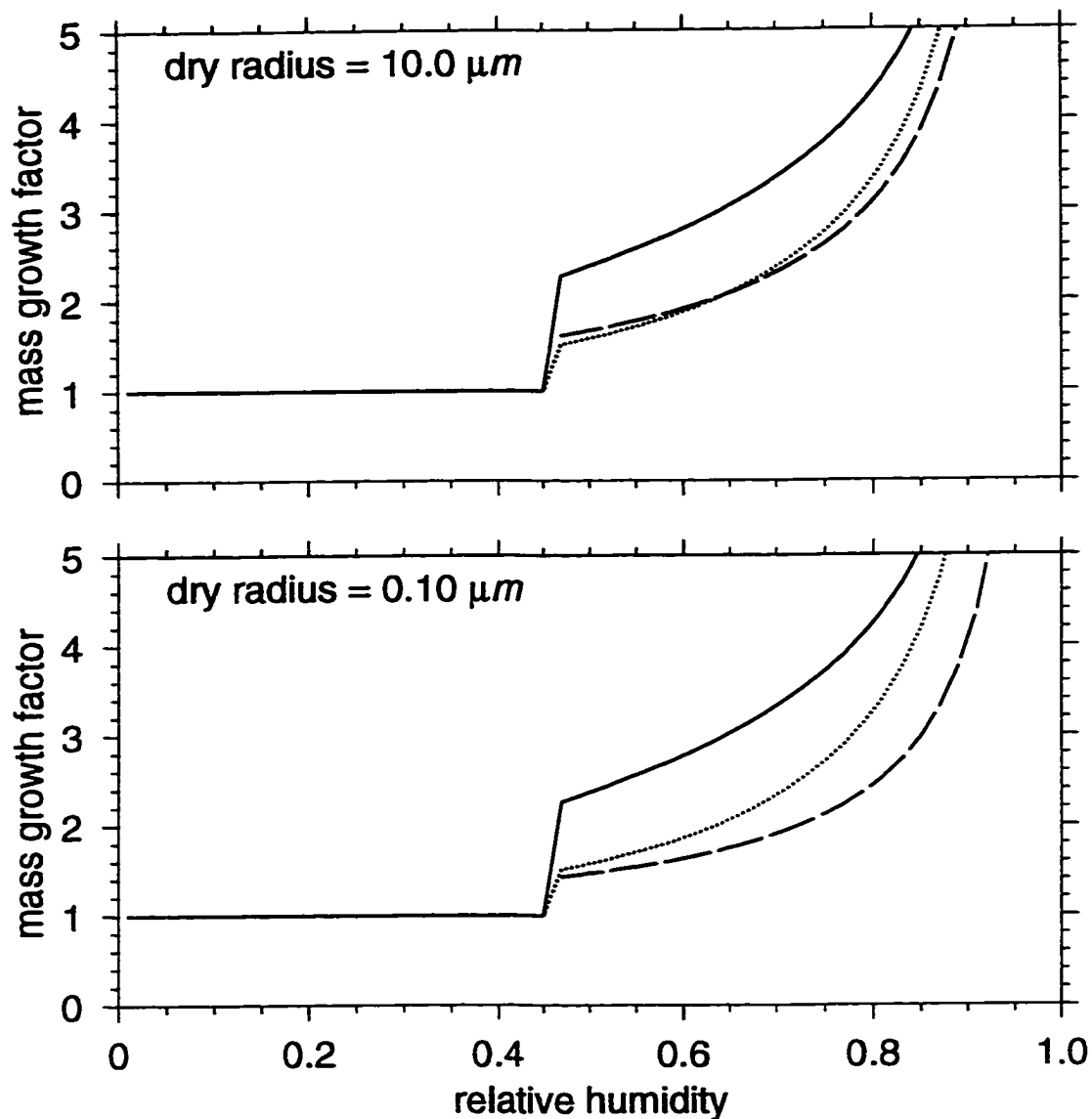
Figure 3.6: The equilibrium mass growth factor of a 10.0 μm (top panel) and 0.10 μm (bottom) dry radius sea salt aerosols as a function of relative humidity. Results obtained from the Köhler equation with a concentration dependent i from Tang et al. (1997) (solid line) and a constant $i = 2.0$ (dotted line) are drawn with results obtained using Gerber's parameterization (dashed line). Only the descending path of the hysteresis effect is drawn.

3.3 Size Distribution

The size of an individual aerosol depends on its chemical composition, its production mechanism, its past interactions with other particles, and on ambient environmental conditions such as relative humidity. Because there are so many factors involved, a collection of aerosols will not be expected to be uniform in size. Jaenicke (1993) and Whitby (1978) use three lognormal functions (equation 2.19) that are added together to form the total size distribution. Each mode was attributed to a different mechanism of production. Coarse mode particles are those particles larger than 1.0 μm in radius. The fine mode particles are less than 1.0 μm in size and are further subdivided into the nucleation and accumulation modes. The nucleation mode particles have radii less than 0.10 μm and particles between 0.10 and 1.0 μm are designated as accumulation mode particles. Sulfate aerosols are formed in the atmosphere by gas-to-particle conversion, which is a series of chemical reactions of sulfur containing gases such as SO_2 to SO_4^{-2} (Charlson and Wigley 1994). Nitrate aerosols are formed by the gas-to-particle conversion of NO_2 (Finlayson-Pitts and Pitts 1986). Sea salt aerosols are introduced into the atmosphere by air bubble bursting at the ocean surfaces (Gong et al. 1997). For aerosols, most of the attention is focussed on the accumulation mode because of this mode's radiative importance (Boucher and Anderson 1995; Nemesure et al. 1995). Even though the nucleation mode has more particles, the accumulation mode has a stronger radiative effect because of their larger size (Lenoble 1993) and there is a smaller number of the coarse mode particles (Lenoble 1993). Furthermore, the atmospheric lifetime of the accumulation mode particles is longer (Gong et al. 1997; Whitby 1978; Wallace and Hobbs 1977).

In order to predict the change in a size distribution of hygroscopic aerosol, three assumptions are made. It is assumed that the particles in the initial dry size distribution do not interact with each other by collision and coagulation events. This first assumption leads to the conclusion that the total number of particles is conserved. The second assumption is that there is enough water vapor in the ambient environment so that there is no competition between particles for the available water vapor.

The third assumption is that each particle independently grows to its equilibrium size described by the Köhler equation.

With these three conditions, the aerosol size distribution is subjected to the following constraint

$$\int_{\bar{r}_a}^{\bar{r}_b} \frac{dN}{dr}(rh)\,dr = \int_{r_a}^{r_b} \frac{dN}{dr}(rh = 0)\,dr \qquad (3.15)$$

where $\bar{r}_a$ and $\bar{r}_b$ are the equilibrium radii at relative humidity rh of aerosol particles with dry radii of r_a and r_b respectively.

Figure 3.7 illustrates the change in a lognormal size distribution of H_2SO_4 aerosols when the relative humidity is increased to 0.95. The initial distribution plotted with the solid curve has $r_0 = 0.05\,\mu m$, and $\ln\sigma_0 = 0.7$. The evolved curve is drawn with the dashed line. A lognormal functional form can be fitted to the new distribution as shown by the dotted line.

The ratio of the fitted to the initial geometric mean radius is plotted as a function of relative humidity in figure 3.8 for H_2SO_4 (o), $(NH_4)_2SO_4$ (•), NH_4HSO_4 (□), HNO_3 (*), and sea salt (▷) aerosol. Initial r_0 of 0.02, 0.05, 0.07, 0.10, 0.15, 0.20, 0.40, 0.60, 0.80, and 1.00 μm are considered with an initial $\ln\sigma_0$ of 0.7.

The growth of NH_4HSO_4 and $(NH_4)_2SO_4$ are similar except for the characteristic crystallization point of NH_4HSO_4 which is at 0.38 relative humidity. The strongest growth is attributed to sea salt aerosols when the relative humidity is greater than their crystallization point of 0.42 relative humidity. Below that point, H_2SO_4 has the most water condensed on them, followed by HNO_3.

Comparing figure 3.8 with figures 3.5 and 3.6, we see that the change in the mean radius with relative humidity is similar to the growth of an individual particle of the same chemical composition. The increase in $\ln\sigma_0$, shown in figure 3.9, is less than 5% for relative humidities less than 0.95 for all the cases that are being considered. Over 0.95 relative humidity, the increase is less than a factor of 1.2.
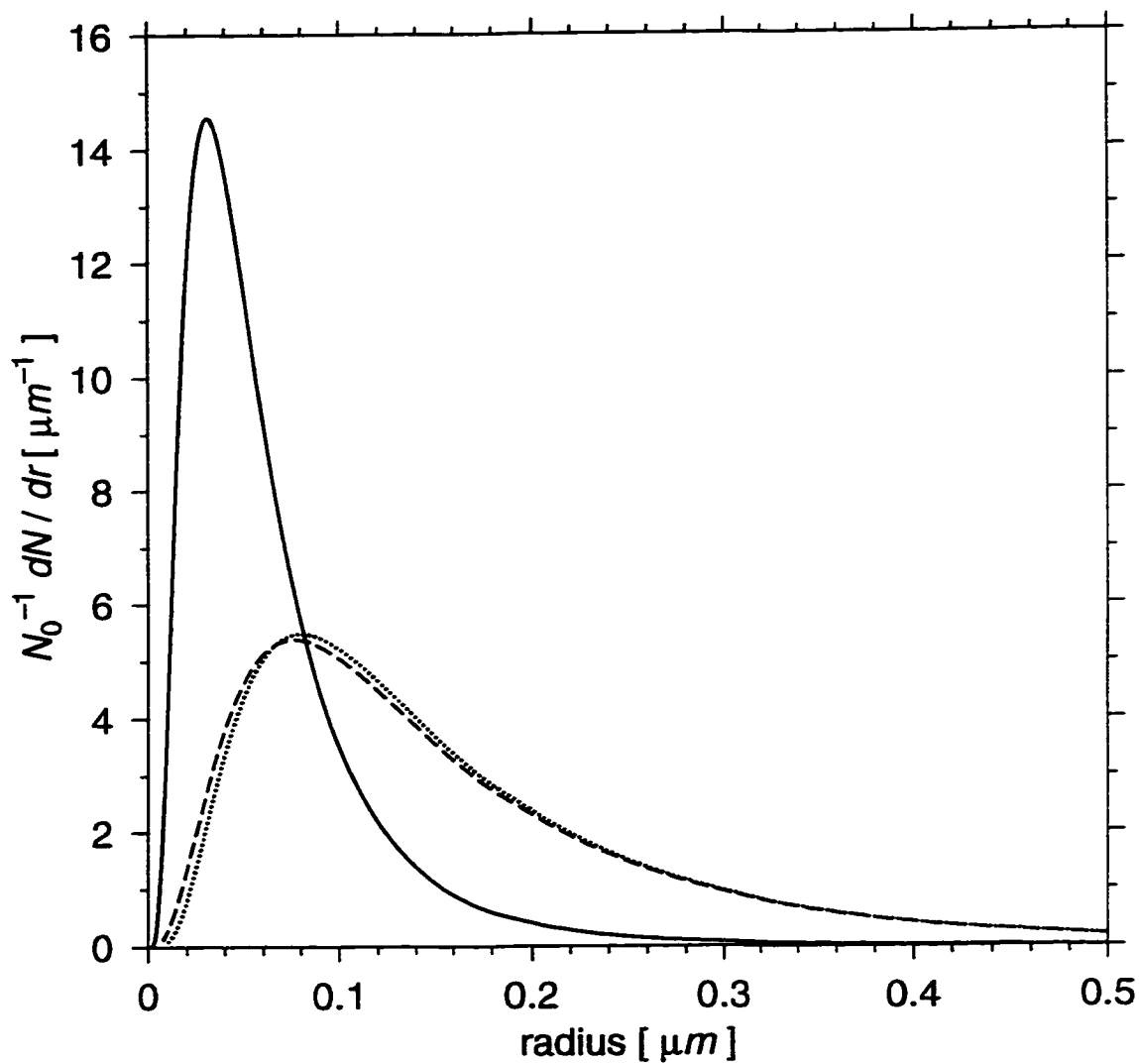
Figure 3.7: The change in a normalized dry size distribution of H_2SO_4 (solid curve) with the relative humidity increased to 0.95 (dashed curve). A lognormal function fitted to the evolved distribution is also shown (dotted curve). The initial distribution has $r_0 = 0.05\,\mu$m and $\ln\sigma_0 = 0.7$.
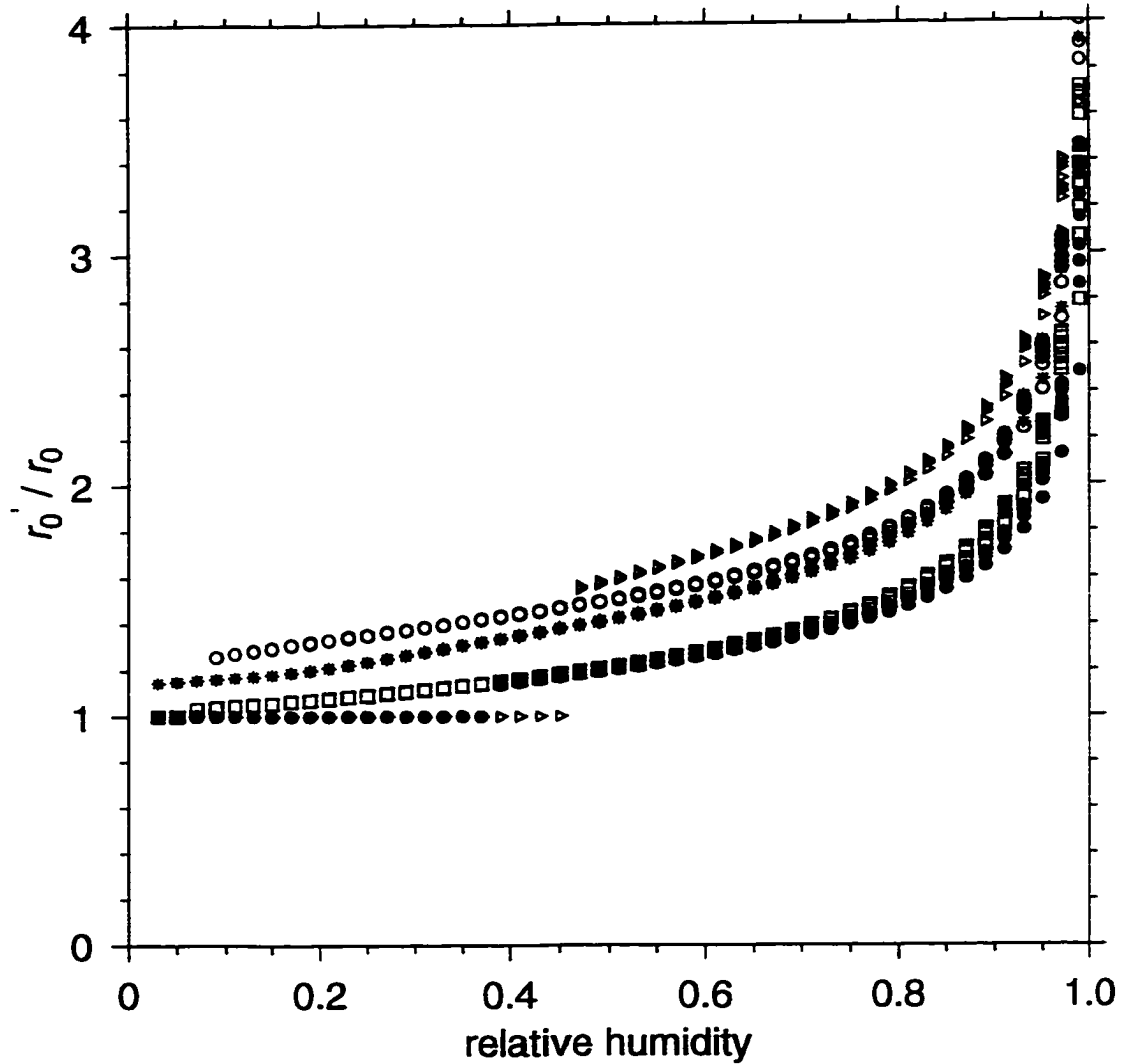
Figure 3.8: The change in the geometric mean radius of aerosol size distributions with relative humidity. Initial dry lognormal distributions of H_2SO_4 (o), $(NH_4)_2SO_4$ (•), NH_4HSO_4 (□), HNO_3 (*), and sea salt (▷) aerosols with $\ln \sigma_0 = 0.7$ and r_0 of 0.02, 0.05, 0.07, 0.10, 0.15, 0.20, 0.40, 0.60, 0.80, and 1.00 μm are considered. Only the descending path of the hysteresis effect is drawn.
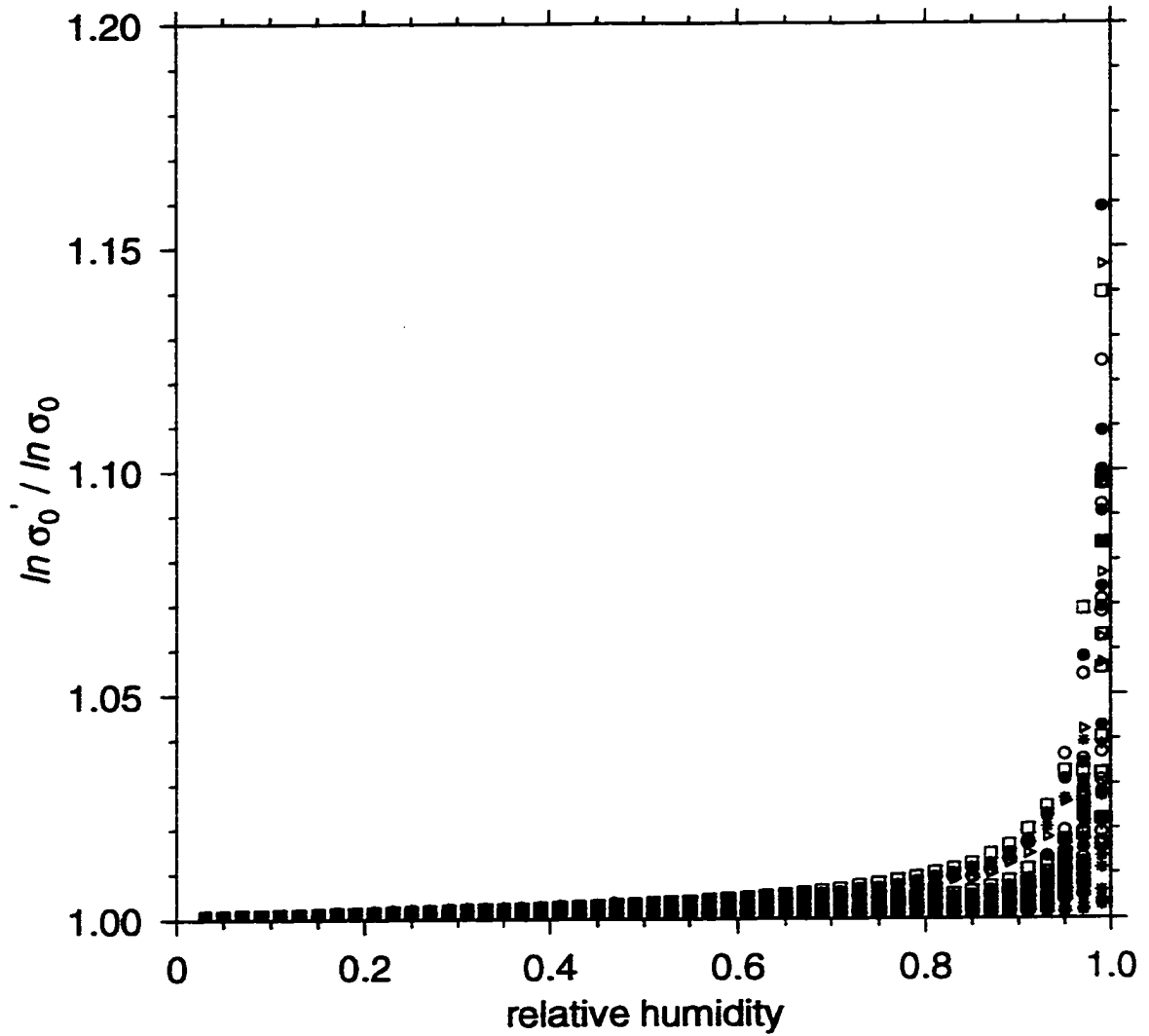
Figure 3.9: The change in $\ln \sigma_0$ of aerosol size distributions with relative humidity. Initial dry lognormal distributions of H_2SO_4 (o), $(NH_4)_2SO_4$ (•), NH_4HSO_4 (□), HNO_3 (*) and sea salt (▷) aerosols with $\ln \sigma_0 = 0.7$ and r_0 of 0.02, 0.05, 0.07, 0.10, 0.15, 0.20, 0.40, 0.60, 0.80, and 1.00 μm are considered.

3.4 Summary

The application of equilibrium thermodynamics leads to the Köhler equation 3.8 as an equilibrium condition between the vapor and solution droplet. The modified Köhler equation derived recently by Young and Warren (1992) is theoretically inconsistent and it is in disagreement with experimental data. Also, the suggestion (Young and Warren 1992) that it is more accurate to use the Köhler equation with a constant van't Hoff factor rather than with the van't Hoff factor dependent on the solution concentration, is not supported by theory or experiment. It is the original Köhler equation with the concentration dependent van't Hoff factor, as suggested by McDonald (1953) and Low (1969), that is the proper equilibrium condition. The results following from this equation are in agreement with experimental data at sub-saturated conditions.

The Gerber parameterization relates particle radius and relative humidity explicitly. This is an advantage since solving the Köhler equation for particle radius is an iterative procedure. For dry $(NH_4)_2SO_4$ aerosols larger than $1\,\mu m$ in radius, the predicted growth factor is similar to solving the Köhler equation with a constant van't Hoff factor with a relative error of approximately 40% at a relative humidity of 0.95. But for smaller dry aerosols, the Gerber parameterization is within 10% of the Köhler equation's mass growth factor for relative humidities less than 0.95. This may be sufficiently accurate for most purposes but for sea salt aerosols, the relative difference of the mass growth factor predicted by the Gerber parameterization relative to the Köhler equation is greater than 30%. Therefore the Köhler equation with a concentration dependent van't Hoff factor must be used for sea salt aerosols.

Using the Köhler equation, changes in a lognormal size distribution of hygroscopic aerosols can be calculated by assuming that the number of aerosols is conserved, and that there is enough water vapor and enough time for each particle to grow to its equilibrium size. A new lognormal function can be fitted to the changed distributions. With the change in aerosol size distribution with relative humidity now known, the optical properties of hygroscopic aerosols and the radiative forcing due to these aerosols can be calculated. This is the topic of the following chapter.

Chapter 4

Radiative Properties of Hygroscopic Aerosols

4.1   Introduction

Considerable effort has been made to estimate the change in climate due to human activities. Fossil fuel burning, changes in land use, and other industrial activities have led to an increase in the atmospheric concentration of carbon dioxide (CO_2), methane (CH_4), nitrous oxide (N_2O), and halocarbon compounds (Schimel et al. 1996). These gases are greenhouse gases which have a warming influence on the surface by absorbing thermal radiation and re-emitting a portion of this energy back to the surface. The radiative forcing at a given level of the atmosphere is the change in the net downward radiative flux at that level due to a perturbation of the Earth and atmosphere system. This quantity, that has units of $W\,m^{-2}$, is a measure of the climatic impact of the perturbation. The increase in greenhouse gas concentration since the mid-1700's has resulted in a surface radiative forcing of approximately $2.45\,W\,m^{-2}$ (Schimel et al. 1996).

The concentration of aerosols in the atmosphere has also risen due to anthropogenic influences. Aerosols affect climate by absorbing and scattering solar radiation. This interaction is called the direct effect. Aerosols also have an indirect effect

which refers to the effect that they have on the radiative properties of clouds. There is considerable variability in the chemical composition and size of the aerosols leading to variability in the radiative characteristics of the particles. Much of the attention of aerosols has been focused on sulfate aerosols because there is a large amount of data about them from acid rain studies. Charlson et al. (1992) estimate the global annual mean direct radiative forcing of sulfate aerosols to be approximately $-1.3 \, \mathrm{W \, m^{-2}}$ and the radiative forcing due to the indirect effect to be approximately $-1 \, \mathrm{W \, m^{-2}}$. The negative value of the radiative forcing implies a cooling effect on climate. Since the total radiative forcing of sulfate aerosols is of the same magnitude as the radiative forcing due to increases in greenhouse gas concentrations, it is clear that sulfate aerosols must be considered if climate predictions are to be made.

Current estimates of sulfate aerosol direct radiative forcing are uncertain (Pan et al. 1997; Schimel et al. 1996). Part of the uncertainty is due to the spatial and temporal variability of the sulfate aerosol. Sulfur containing gases such as sulfur dioxide (SO_2) are emitted into the atmosphere from industrial emissions. Natural emissions of sulfur containing gases include dimethyl sulfide by marine phytoplankton (Charlson et al. 1987). Sulfate (SO_4^{-2}) is formed from the sulfur dioxide by gas-to-particle conversions where the gas chemically reacts in the atmosphere. The atmospheric lifetime of the aerosol is on the order of a week (Chuang et al. 1997; Bondietti and Papastefanou 1993). This leads to geographical variation in the direct radiative forcing of the aerosols since the particles will be concentrated near their emission sources. This is in contrast to greenhouse gases such as carbon dioxide which are considered to be well mixed in the lower atmosphere. The forcing due to increases in greenhouse gas concentrations still varies with location because of the variations in temperature, water vapor, and cloud cover (Kiehl and Rodhe 1995). Progress has been made in modelling the distribution of sulfate using chemical transport models (Pham et al. 1995; Langner and Rodhe 1991) and global climate models (Feichter et al. 1997). There is also uncertainty in defining the optical properties of the particles themselves. The dominant chemical composition of sulfate aerosols is a

mixture of sulfuric acid, ammonium bisulfate, and ammonium sulfate (Charlson et al. 1978) depending on the amount of ammonia available.

In this chapter, the variation of the optical properties of tropospheric ammonium sulfate aerosols with relative humidity and the effect on the direct radiative forcing due to the aerosols are examined. Variation due to the hysteresis effect of hygroscopic growth, initial size distribution, and refractive index mixing are considered. Comparisons are made with the sulfuric acid, ammonium bisulfate, and nitric acid aerosols. The optical properties and direct radiative forcing of sea salt aerosols are also considered. Sulfate, nitrate, and sea salt aerosols do not absorb much solar radiation. Other aerosols such as black carbon, soil dust, and biomass burning aerosols are not considered since their hygroscopic nature and refractive index are uncertain. The optical properties of ammonium sulfate and sea salt aerosols obtained when aerosol growth is modelled with the Köhler equation with a constant van't Hoff factor and with the Gerber parameterization are compared with those obtain with a variable van't Hoff factor in the Köhler equation.

The optical properties of sulfate aerosols are parameterized as functions of relative humidity and are used in a radiation model that accounts for the spatial and temporal changes in sulfate burden and relative humidity. The radiative forcing is calculated over every location of the planet and for each month and the results are averaged to obtain the global annual average direct radiative forcing of sulfate aerosols. The result is compared to values obtained when the optical properties were not completely treated for hygroscopic growth.

4.2   Optical Properties

Three optical properties needed in common radiative transfer models are the extinction optical depth, τ, the single scattering albedo, ω, and the asymmetry parameter, g.

The aerosol extinction optical depth is a unitless quantity that indicates the

amount of radiation that is removed from an incident beam after it has passed through an aerosol layer. If the aerosol amount is specified by aerosol burden, B in units of $g\,m^{-2}$, then the optical depth can be obtained by

$$\tau = \left(\frac{k_{ext}}{M}\right) \times B \tag{4.1}$$

where M is the aerosol mass concentration in units of $g\,m^{-3}$ and k_{ext} is the extinction coefficient in units of m^{-1}. The quotient k_{ext}/M is called the specific extinction coefficient of the aerosol and has units of $m^2\,g^{-1}$.

For a size distribution, dN/dr, of particles, the extinction coefficient is calculated by

$$k_{ext}^{i} = \frac{\int_{\lambda_i}^{\lambda_{i+1}} \int_{r=0}^{\infty} \sigma_{ext} \frac{dN}{dr} \frac{dS}{d\lambda} \, dr \, d\lambda}{\int_{\lambda_i}^{\lambda_{i+1}} \frac{dS}{d\lambda} \, d\lambda} \tag{4.2}$$

where σ_{ext} is the extinction cross section of an individual particle which has the dimensions of m^2. The solar flux at the top of the atmosphere, $dS/d\lambda$ (Thekaekara and Drummond 1971), is used as the weighting function to obtain an average value of k_{ext} that is representative for the wavelength band defined by λ_i and λ_{i+1}. If the aerosol size distribution is lognormal then the total aerosol mass concentration is obtained by

$$
\begin{aligned}
M &= \int_0^{\infty} \frac{4\pi}{3} \rho r^3 \frac{dN}{dr} \, dr \\
&= \frac{4\pi}{3} \rho N_0 r_0^3 \exp\left(\frac{9}{2} \ln^2 \sigma_0\right)
\end{aligned} \tag{4.3}
$$

where ρ is the mass density of the aerosol.

The energy that is removed from the incident beam can be either scattered into another direction or absorbed by the particle itself. The single scattering albedo is the fraction of the energy that is scattered to the total extinction

$$\omega^i = \frac{k_{sc}^i}{k_{ext}^i} \tag{4.4}$$

where k_{sc}^i is the scattering coefficient which is calculated in the same manner as k_{ext}^i but replacing σ_{ext} with the scattering cross section σ_{sc} in equation 4.2

$$k_{sc}^i = \frac{\int_{\lambda_i}^{\lambda_{i+1}} \int_{r=0}^{\infty} \sigma_{sc} \frac{dN}{dr} \frac{dS}{d\lambda} \, dr \, d\lambda}{\int_{\lambda_i}^{\lambda_{i+1}} \frac{dS}{d\lambda} \, d\lambda}$$ (4.5)

The single scattering co-albedo, $1 - \omega$, is the fraction of the total extinction that is due to absorption.

The asymmetry parameter is obtained by

$$g^i = \frac{\int_{\lambda_i}^{\lambda_{i+1}} \int_{r=0}^{\infty} g_s \sigma_{sc} \frac{dN}{dr} \frac{dS}{d\lambda} \, dr \, d\lambda}{\int_{\lambda_i}^{\lambda_{i+1}} \int_{r=0}^{\infty} \sigma_{sc} \frac{dN}{dr} \frac{dS}{d\lambda} \, dr \, d\lambda}$$ (4.6)

where g_s is the asymmetry parameter of a single particle.

The extinction cross section, scattering cross section, and asymmetry parameter are all complicated functions of particle size, shape, chemical composition, and wavelength. For the accumulation mode aerosol size distributions that are being considered, the size of the particles is comparable to the wavelength of shortwave radiation. The particles are assumed to be homogeneous and spherical in shape, so Mie theory can be used to calculate each optical property given the particle radius r, the wavelength of light λ, and both the real and imaginary parts of its refractive index m of the particle (Bohren and Huffman 1983; van de Hulst 1981). The refractive index is also wavelength dependent.

In chapter 3, the effect of relative humidity on the size of the particle was studied. Increasing the relative humidity can result in an increase in the radius by over a factor of 2.0 which can lead to significant changes to the scattering characteristics of the particle. Changes in the optical properties due to changes in the relative humidity are not solely due to the resultant change in size. They are also due to the change in the chemical composition of the particle which alters the refractive index.

To treat the change in the refractive index as water condenses on the particle, the effective refractive index, m_{eff}, is obtained from the refractive indices of the pure components, m_j, by assuming a linear dependence in the volume fractions of the

components, v_j,

$$m_{eff} = \sum_j m_j v_j \qquad (4.7)$$

where the summation over j is for each chemical component. This is one of the simplest of mixing rules (Chýlek et al. 1988), which is reasonably accurate if the refractive indices of the individual components are not too different.

The real part of the refractive index of water (H_2O) used is the compilation of measurements by Hale and Querry (1984) between wavelengths of 0.200 and 0.675 μm, Palmer and Williams (1974) for wavelengths up to 2.0 μm, and by Downing and Williams (1975) for wavelengths longer than 2.0 μm. The imaginary refractive index are obtained from Hale and Querry (1984), Downing and Williams (1975), and Kou et al. (1993).

The refractive index of sulfuric acid (H_2SO_4) measured by Palmer and Williams (1975) for solutions of 0.75 concentration by mass is used for the real part with measurements starting at 0.36 μm. Palmer and Williams (1975)'s data for the imaginary part begins at 0.70 μm and is replaced in the wavelength interval between 1.47 and 2.56 μm by data from Gosse et al. (1997) for 0.72 solution. Equation 4.7 is used to obtain the refractive index of 0.99 solution.

The refractive index for wavelengths greater than 0.3 μm of crystalline ammonium sulfate measured by Toon et al. (1976) is adopted with Gosse et al. (1997) data between 1.405 and 2.660 μm wavelength for 0.40 solution.

The only data found for the refractive index of dry ammonium bisulfate for short-wave radiation is a real value of 1.473 tabulated in Lide (1997). This value and an imaginary part of zero are taken for the whole solar wavelength domain. Lide (1997) is also the source of the real refractive index value of 1.397 for dry nitric acid. The imaginary part for nitric acid is also taken to be zero. For the refractive index of crystalline sea salt, values from Volz (1972) are used.

The real and imaginary parts of the refractive index for water and crystalline sea salt are plotted in figure 4.1 along with the index of 0.99 sulfuric acid and ammonium sulfate solutions.
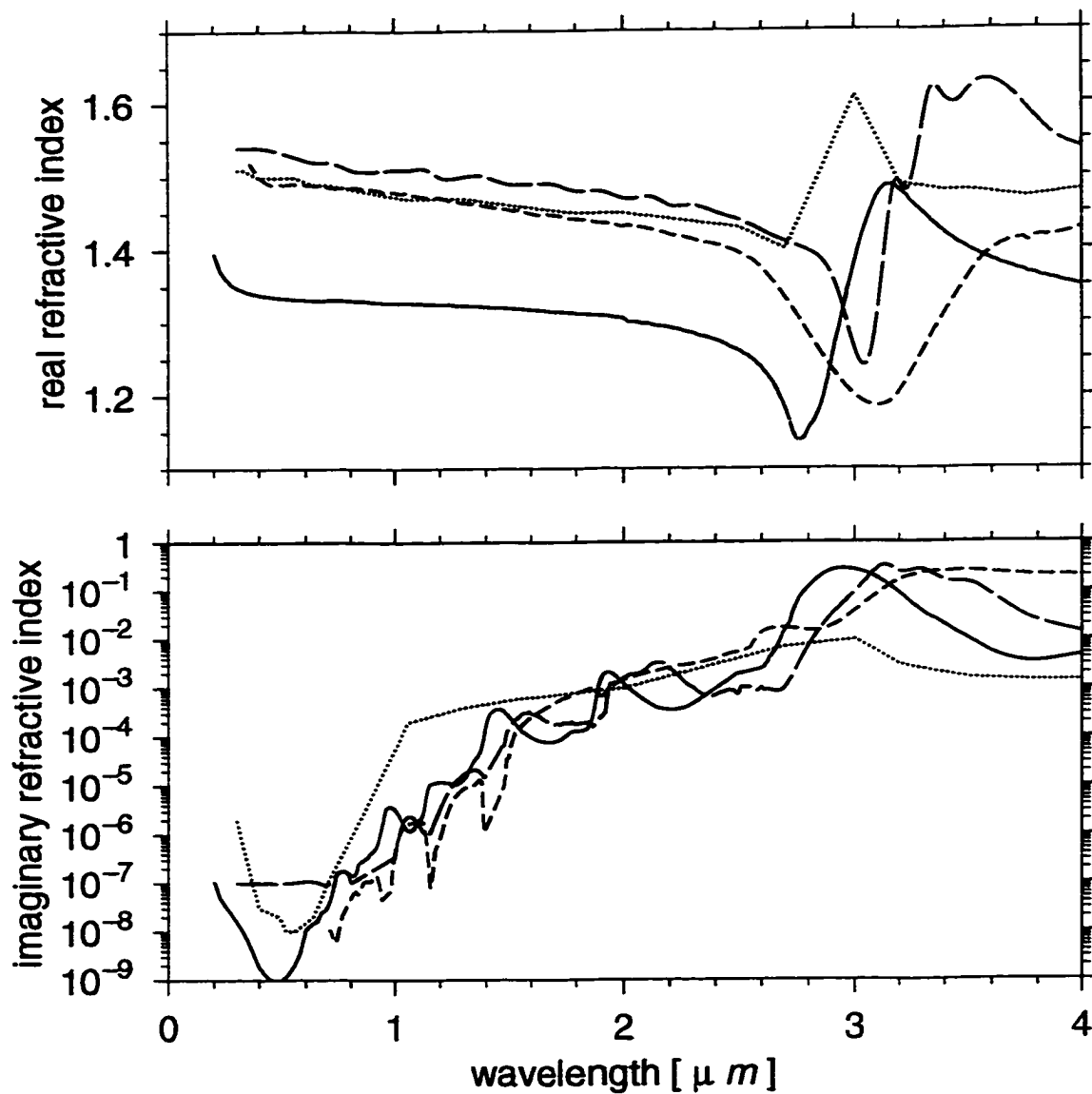
Figure 4.1: The wavelength dependence of the real part (top panel) and the imaginary part (bottom) of the refractive index of H_2O (solid line) and sea salt (dotted line). The refractive index of 0.99 solutions of H_2SO_4 (short dashed line) and $(NH_4)_2SO_4$ (long dashed line) are also plotted.

Given the relative humidity and size distribution of dry aerosol, the Köhler equation (equation 3.8) is used with the constraint of particle number conservation (equation 3.15) to determine the equilibrium size distribution of the aerosol. At the same time, the volume fraction of the solute in each particle is obtained by the cube of the ratio of the equilibrium radius to the initial dry radius. With this volume fraction, the effective refractive index of the particle is obtained by equation 4.7. With the effective refractive index and equilibrium radius, the Mie scattering properties can be calculated for each wavelength. It is these values of σ_{ext}, σ_{sc}, g_s, and the equilibrium dN/dr that are used in the integrals 4.2, 4.5, and 4.6.

In the three panels of figure 4.2, the extinction coefficient (top panel), single scattering albedo (middle), and asymmetry parameter (bottom) of ammonium sulfate are plotted as functions of wavelength at relative humidities of 0.0 ($\square$), 0.51 ($\blacktriangle$), 0.75 ($\circ$), and 0.90 ($*$). The specific extinction and asymmetry parameter decrease as the wavelength of light increases while the single scattering co-albedo increases. The amount of radiation emitted by the sun also decreases as the wavelength gets longer (Thekaekara and Drummond 1971).

Figure 4.3 plots the extinction coefficient per unit mass of sulfate (SO_4^{-2}), single scattering co-albedo, and asymmetry parameter of ammonium sulfate aerosols as functions of relative humidity for the wavelength band between 0.175 and 0.690 μm. This wavelength band contains 0.456 of the solar energy that is emitted by the sun. The initial dry size distribution parameters shown in this case are $r_0 = 0.05\,\mu$m and $\ln \sigma_0 = 0.7$. This is the same size distribution that is discussed by Kiehl and Briegleb (1993) and Haywood and Shine (1995).

The hysteresis effect of ammonium sulfate aerosols is shown by the curve drawn with the $\bullet$ symbols. The optical properties remain constant at the values corresponding to dry aerosols as the relative humidity is increased. Once the deliquescence humidity is reached, which is 0.80 for ammonium sulfate aerosols, the particle grows in size and the refractive index of the particle changes with the increase in particle mass due to condensed water. This results in a change in the optical properties. For
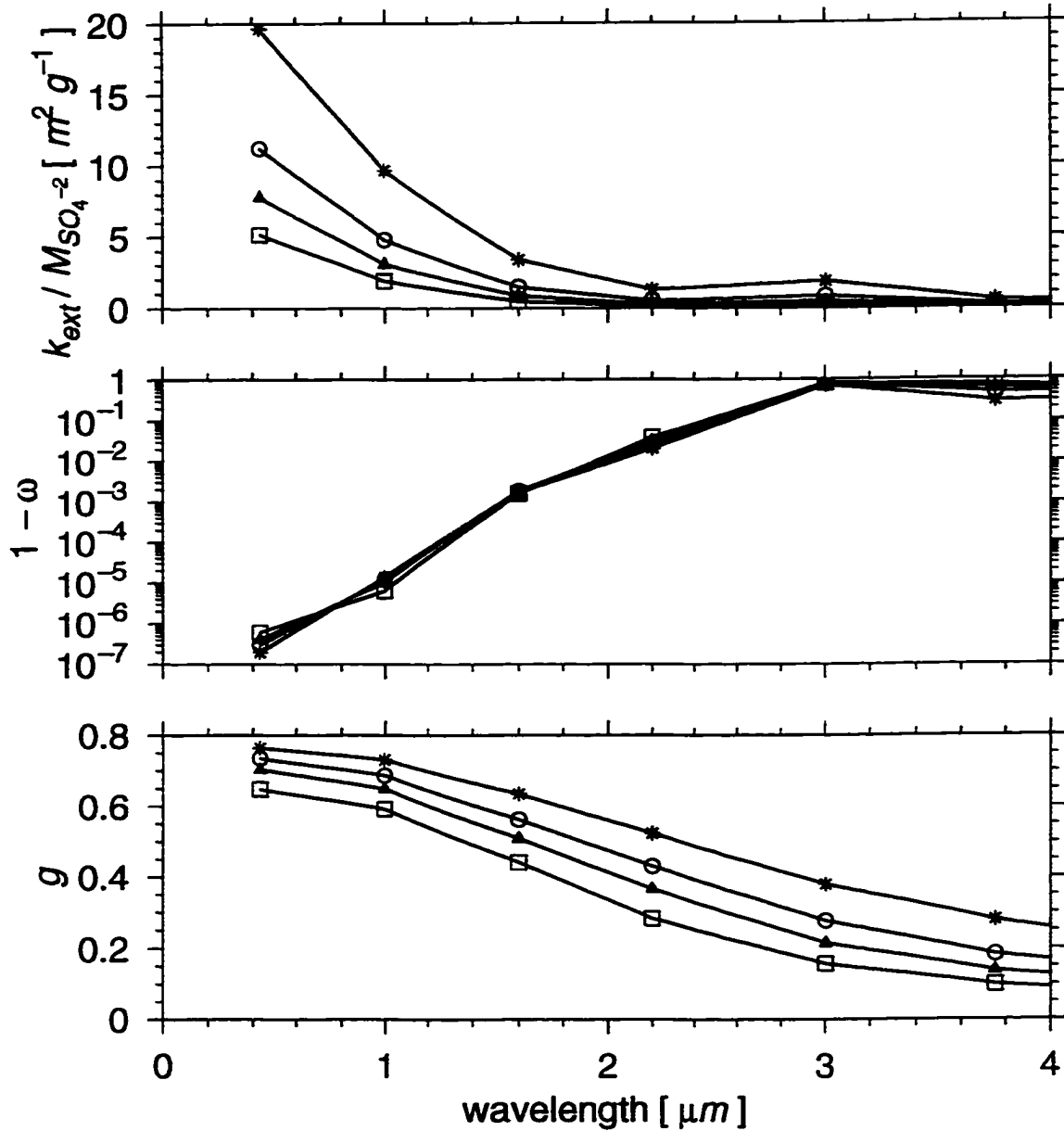
Figure 4.2: The specific extinction (top), single scattering co-albedo (middle), and asymmetry parameter (bottom) of a lognormal size distribution of $(NH_4)_2SO_4$ aerosol with $r_0 = 0.05\,\mu m$ and $\ln\sigma_0 = 0.7$ as functions of wavelength for relative humidities of 0.0 ($\square$), 0.51 ($\blacktriangle$), 0.75 ($\circ$), and 0.90 ($*$)
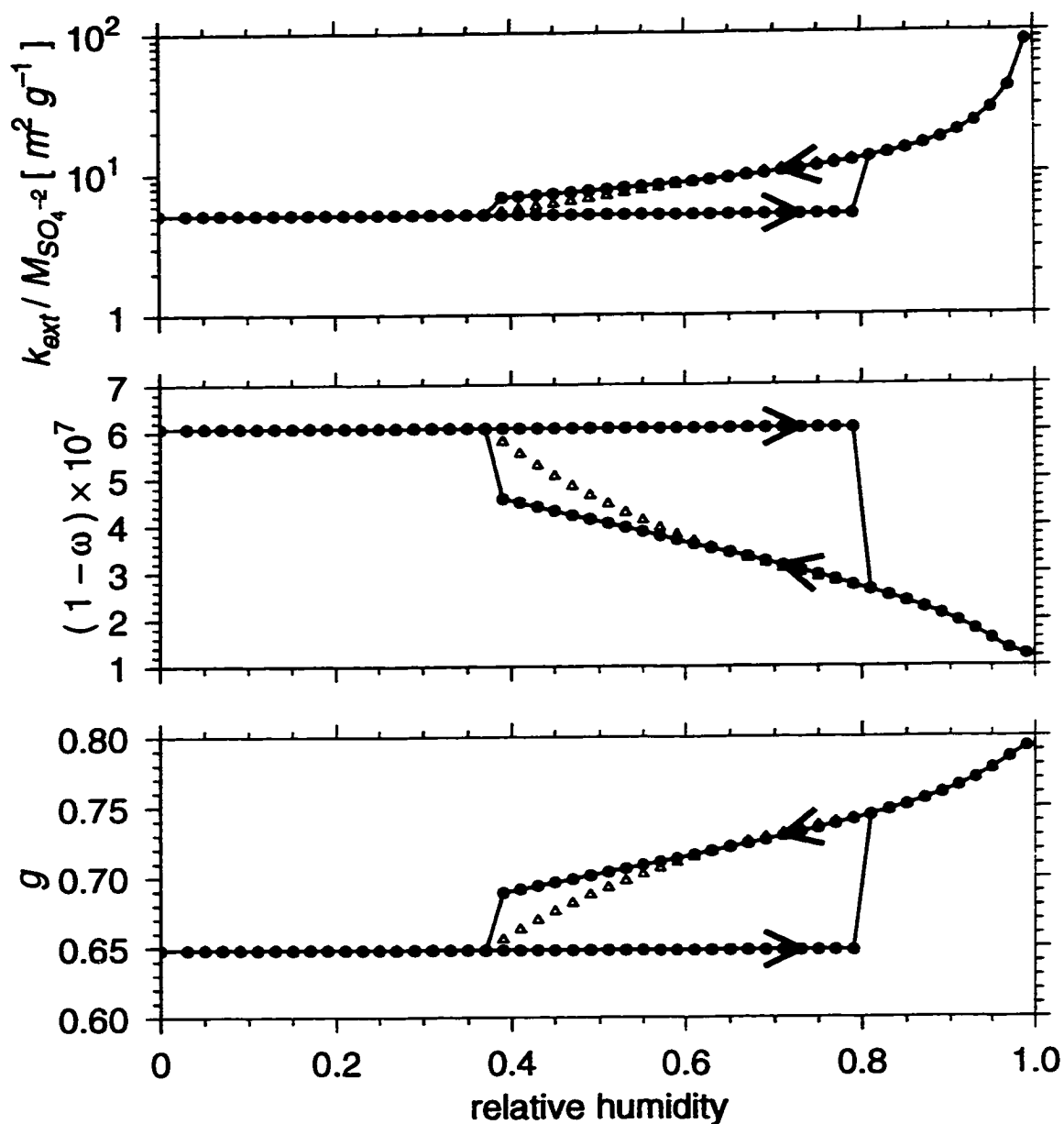
Figure 4.3: The specific extinction coefficient (top panel), single scattering co-albedo (middle), and asymmetry parameter (bottom) of a lognormal size distribution of $(NH_4)_2SO_4$ aerosol with $r_0 = 0.05$ μm and $\ln \sigma_0 = 0.7$ for the wavelength band between 0.20 and 0.69 μm as functions of relative humidity. The curve drawn with the ● symbol illustrates the hysteresis effect of aerosol growth and the △ corresponds to using the mean of the wet and dry state radii to model aerosol growth.

this particular case, the specific extinction increases by a factor of 2.5 from $5.2\,m^2\,g^{-1}$ to $13.0\,m^2\,g^{-2}$. The single scattering co-albedo is reduced from its initial value of 6.1×10^{-7} by a factor of 0.43 to 2.6×10^{-7}. The asymmetry parameter increases from 0.65 to 0.74 — a factor of 1.15. The specific extinction and asymmetry parameter continues to increase as the relative humidity is increased, and the single scattering co-albedo decreases. At 0.99 relative humidity, the specific extinction is $85\,m^2\,g^{-1}$, the asymmetry parameter is 0.79, and the single scattering co-albedo is 1.2×10^{-7}. When the relative humidity is decreased while the aerosols are in a wet state, the optical properties varies smoothly until the relative humidity reaches the crystallization point, which is 0.37 for ammonium sulfate aerosols. At that point, the specific extinction is $6.8\,m^2\,g^{-1}$ — still a factor of 1.3 times the value of the dry state aerosol. The asymmetry parameter is 1.06 times larger than the dry state value at 0.69, and the co-albedo is 4.6×10^{-7}. When the relative humidity is decreased below the crystallization humidity the optical properties changes to the values corresponding to the dry aerosol. Most climate and radiation models are not able to follow the history of the particles. Such models may attempt to treat the hysteresis effect of particle growth by using the mean of the wet and dry state radius of a particle to represent its radius when the relative humidity is between the crystallization and deliquescence points. The $\triangle$ symbols in figure 4.3 correspond to using this average radius.

To characterize the radiative impact of these changes in the optical properties, the radiative forcing at the top of the atmosphere due to a layer of the aerosol is calculated. Radiative forcing at a given level in the atmosphere is defined as the change in the net downward radiative flux due to a change in the atmospheric conditions. In this case, this change is the introduction of a layer of aerosols which backscatter and hence decrease the net downward flux.

The Fu-Liou radiation model (Fu 1991) is used to obtain the radiative forcing due to the aerosol in the standard mid-latitude summer atmosphere (McClatchey et al.

band	minimum wavelength [μm]	maximum wavelength [μm]	solar weight
1	0.20	0.69	0.458
2	0.69	1.30	0.358
3	1.30	1.90	0.110
4	1.90	2.50	0.036
5	2.50	3.51	0.023
6	3.51	4.00	0.004

Table 4.1: Solar wavelength bands of the Fu-Liou radiation model and the solar weight in each band.

1971). The atmospheric system is divided into 70 horizontally uniform layers. The Fu-Liou model uses the correlated k-distribution technique to model the transmittance of atmospheric gases. The radiative transfer through each of these layers is solved for 6 solar wavelength bands, which are tabulated in Table 4.1, using the delta-four-stream approximation (Liou 1992; Liou and Fu 1988). This program allows the user to set parameters such as the solar zenith angle, solar constant, and surface albedo. The user can place any amount of aerosol in any of the atmospheric layers after specifying the optical properties of the aerosol for each wavelength band.

The sulfate aerosol is placed in the bottom atmospheric layer which is approximately 1 km thick with a burden of $10^{-2} \, \mathrm{g\,m^{-2}}$. This is stronger than the global average burden of anthropogenic sulfate, which is approximately $3.8 \times 10^{-3} \, \mathrm{g\,m^{-2}}$, but polluted regions are estimated to have burdens greater than $2.0 \times 10^{-2} \, \mathrm{g\,m^{-2}}$ (Pham et al. 1995). The surface albedo is set to 0.0 and one can expect the radiative forcing to decrease with non-zero surface albedos by inspecting equation 2.1. The solar zenith angle is set to $60°$. The broadband radiative forcing is plotted as a function of relative humidity in the aerosol layer in figure 4.4.

The radiative forcing due to aerosols in their dry state is $-6.2 \, \mathrm{W\,m^{-2}}$ which increases by almost a factor of two to $-11.9 \, \mathrm{W\,m^{-2}}$ when the deliquescence humidity is reached. The forcing continues to grow stronger with increasing humidity. At the
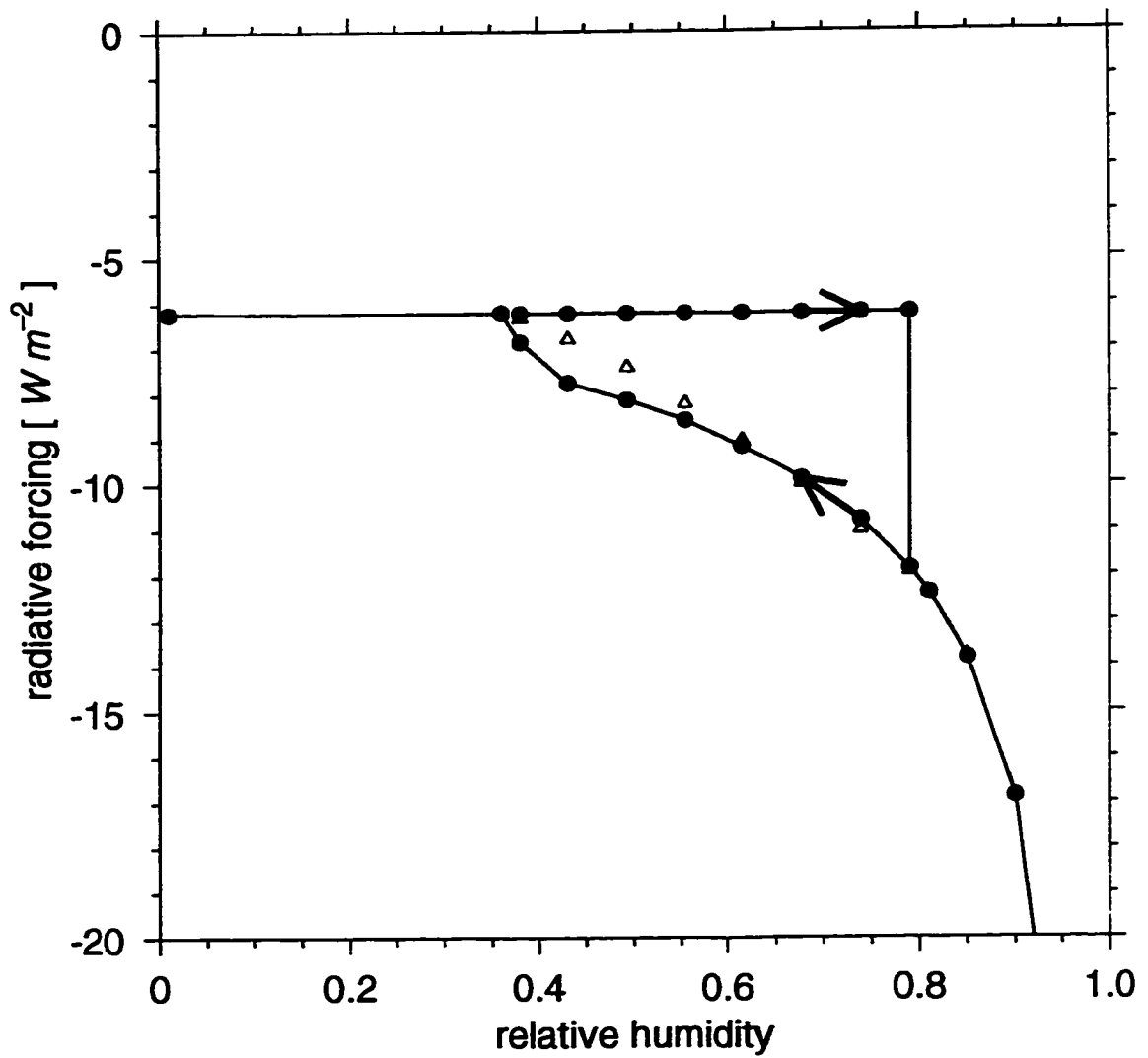
Figure 4.4: The direct top-of-the-atmosphere radiative forcing of a lognormal size distribution of $(NH_4)_2SO_4$ aerosol with $r_0 = 0.05\,\mu m$ and $\ln \sigma_0 = 0.7$ as a function of relative humidity. The curve drawn with the $\bullet$ symbol illustrates the hysteresis effect of aerosol growth. The curve drawn with $\triangle$ corresponds to using the mean of the wet and dry state radii to model aerosol growth with relative humidity. The surface albedo is zero, the solar zenith angle is $60°$, and the sulfate burden is $10^{-2}\,g\,m^{-2}$.

crystallization relative humidity, the radiative forcing of the wet aerosol is 1.1 times stronger than the dry aerosol. This large change demonstrates the importance of considering the hygroscopic nature of these aerosols.

Climate models may not be able to follow the hysteresis effect of aerosol growth. To address this problem when the relative humidity is between the crystallization and deliquescence points, the radius of the aerosol is taken to be the mean of the wet and dry state radii. The resulting optical properties are shown with the $\triangle$ symbols in figure 4.3. The radiative forcing due to aerosols with this behavior is also shown in figure 4.4. The aerosol radiative forcing with this treatment follows the curve corresponding to wet aerosols when the humidity is greater than 0.60 and for humidities less than 0.60 the curve is closer to the wet aerosol curve than to the dry aerosol curve. This is similar to Boucher and Anderson (1995) and Haywood et al. (1997)'s study where they modeled aerosol radius in this humidity domain with a linear interpolation between the dry radius at the crystallization point and the wet radius at the deliquescence point. Using their global climate model (GCM), Boucher and Anderson (1995) found a 20% increase in the global radiative forcing of ammonium sulfate aerosol when the optical properties of the wet aerosol is used than when the optical properties of the dry aerosol is used for relative humidities between the crystallization and deliquescence points. They found a 3% decrease in the forcing when the linear interpolation treatment of aerosol growth is used compared to using the wet aerosol optical properties. Haywood et al. (1997) found similar differences.

In chapter 3, the growth of ammonium sulfate aerosols predicted by the Gerber parameterization (Gong et al. 1997; Gerber 1985) was compared to the growth predicted by the Köhler equation. This comparison is continued with figures 4.5 and 4.6 which plot the optical properties and radiative forcing of wet $(NH_4)_2SO_4$ aerosols that is obtained if aerosol growth is modeled with Gerber's equation ($\triangleright$) along with the curves corresponding to the use of Köhler's equation ($\bullet$). The same initial dry size distribution with $r_0 = 0.05\,\mu m$ and $\ln \sigma_0 = 0.7$ is considered. A third curve is also drawn in each of these figures which is obtained by using the Köhler equation

Figure 4.5: The specific extinction coefficient (top panel), single scattering co-albedo (middle), and asymmetry parameter (bottom) of a lognormal size distribution of wet $(NH_4)_2SO_4$ aerosol with $r_0 = 0.05\,\mu m$ and $\ln\sigma_0 = 0.7$ for the wavelength band between 0.20 and $0.69\,\mu m$ as functions of relative humidity. The curve drawn with the • and □ symbols correspond to using a variable i or a constant $i = 3.0$ in the Köhler equation. The results using the Gerber parameter is drawn with ▷ symbols.
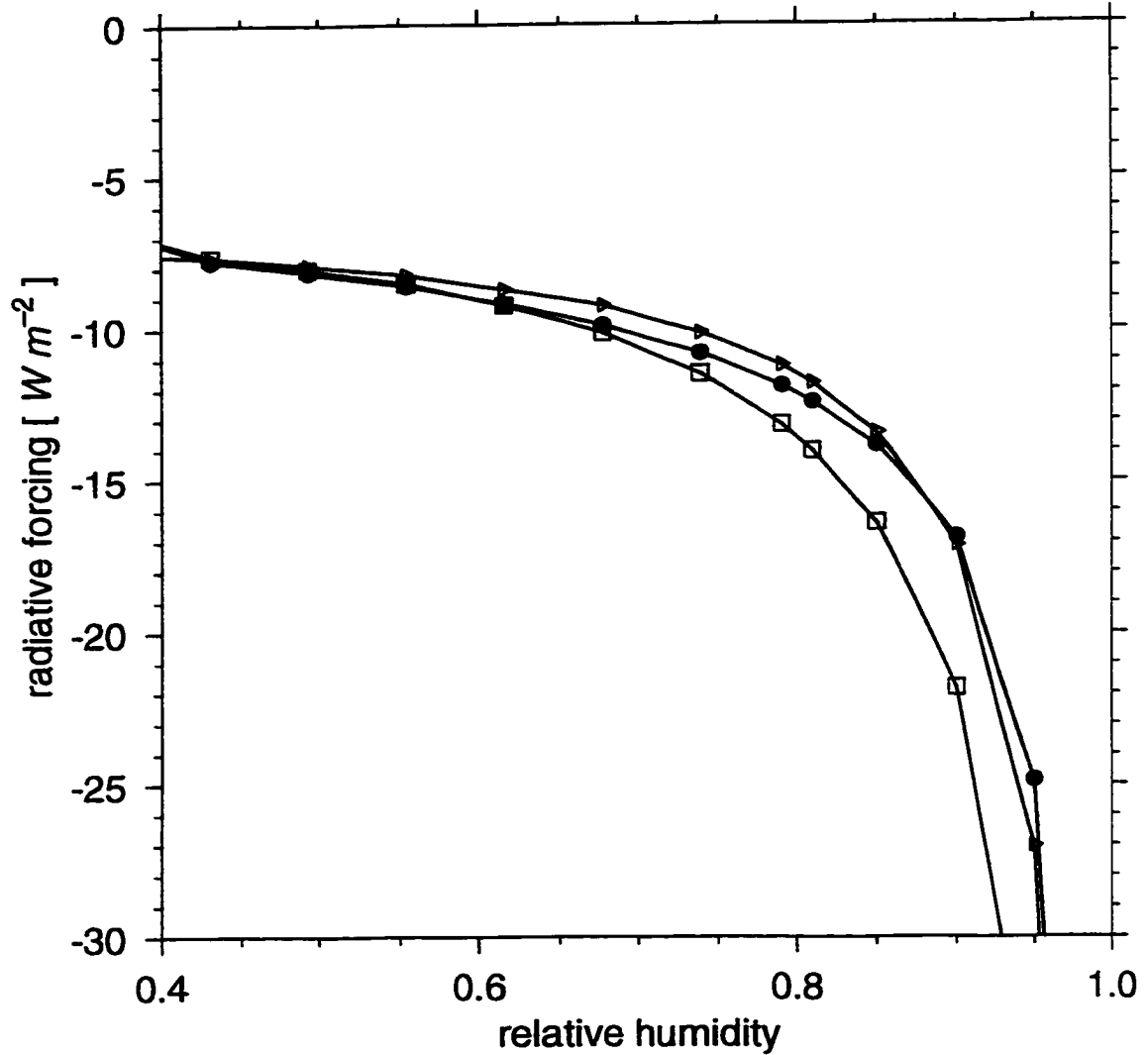
Figure 4.6: The direct top-of-the-atmosphere radiative forcing of a lognormal size distribution of wet $(NH_4)_2SO_4$ aerosol with $r_0 = 0.05\,\mu m$ and $\ln\sigma_0 = 0.7$ as a function of relative humidity. The curve drawn with the • symbol corresponds to using i obtained from Tang and Munkelwitz (1994) in the Köhler equation. The curve with □ symbols corresponds to using a constant $i = 3.0$. The results using the Gerber parameter is drawn with ▷ symbols. The surface albedo is zero, the solar zenith angle is 60°, and the sulfate burden is $10^{-2}\,\mathrm{g\,m^{-2}}$.

with a constant van't Hoff factor of 3.0 ($\square$). The initial dry size distribution has parameters of $r_0 = 0.05\,\mu m$ and $\ln \sigma_0 = 0.7$ and the sulfate burden is $10^{-2}\,g\,m^{-2}$. The difference between using a constant van't Hoff factor and one that is concentration dependent parameter in the Köhler equation is small when the relative humidity is less than 0.65, however, as the humidity increases beyond 0.65, the curves begin to deviate from each other and the curve corresponding to the use of the Gerber parameterization is closer to the curve using a concentration dependent van't Hoff factor. At a relative humidity of 0.90, using a constant $i = 3.0$ in the Köhler equation leads to a radiative forcing that is stronger than that obtained using a concentration dependent i by a relative difference of 29%. Using the Gerber parameterization leads to a relative difference of only 1.5%. Therefore, for accumulation mode size distributions of $(NH_4)_2SO_4$ aerosols, using the Gerber parameterization to model aerosol growth does not lead to a large error whereas using a constant van't Hoff factor does.

The volume average refractive index mixing rule is used to treat the effect of hygroscopic growth on the refractive index of the particle. Figure 4.7 shows the effect of using this mixing rule on the optical properties of the same dry size distribution of ammonium sulfate aerosols considered before as functions of relative humidity. The $\square$ symbols corresponds to the optical properties obtained if the refractive index of the particle is taken to be that of pure ammonium sulfate. The o symbols corresponds to using the refractive index of pure water. The • symbols shows how using the mixing rule produces intermediate values. As relative humidity increases, these intermediate values tend towards those drawn with the o symbols which is consistent with the fact that at high relative humidities a large amount of water is condensed on the particles and it is expected that the optical properties should be similar to that of water. For this case, using the refractive index of $(NH_4)_2SO_4$ leads to a specific extinction that is $8\,m^2\,g^{-1}$ higher than when the refractive index of water is used when the relative humidity is 0.97. Using the refractive index of $(NH_4)_2SO_4$ results in a single scattering co-albedo that is a factor of approximately two larger than when the refractive index of water is used. The asymmetry parameter is between 15% to 20% larger when the
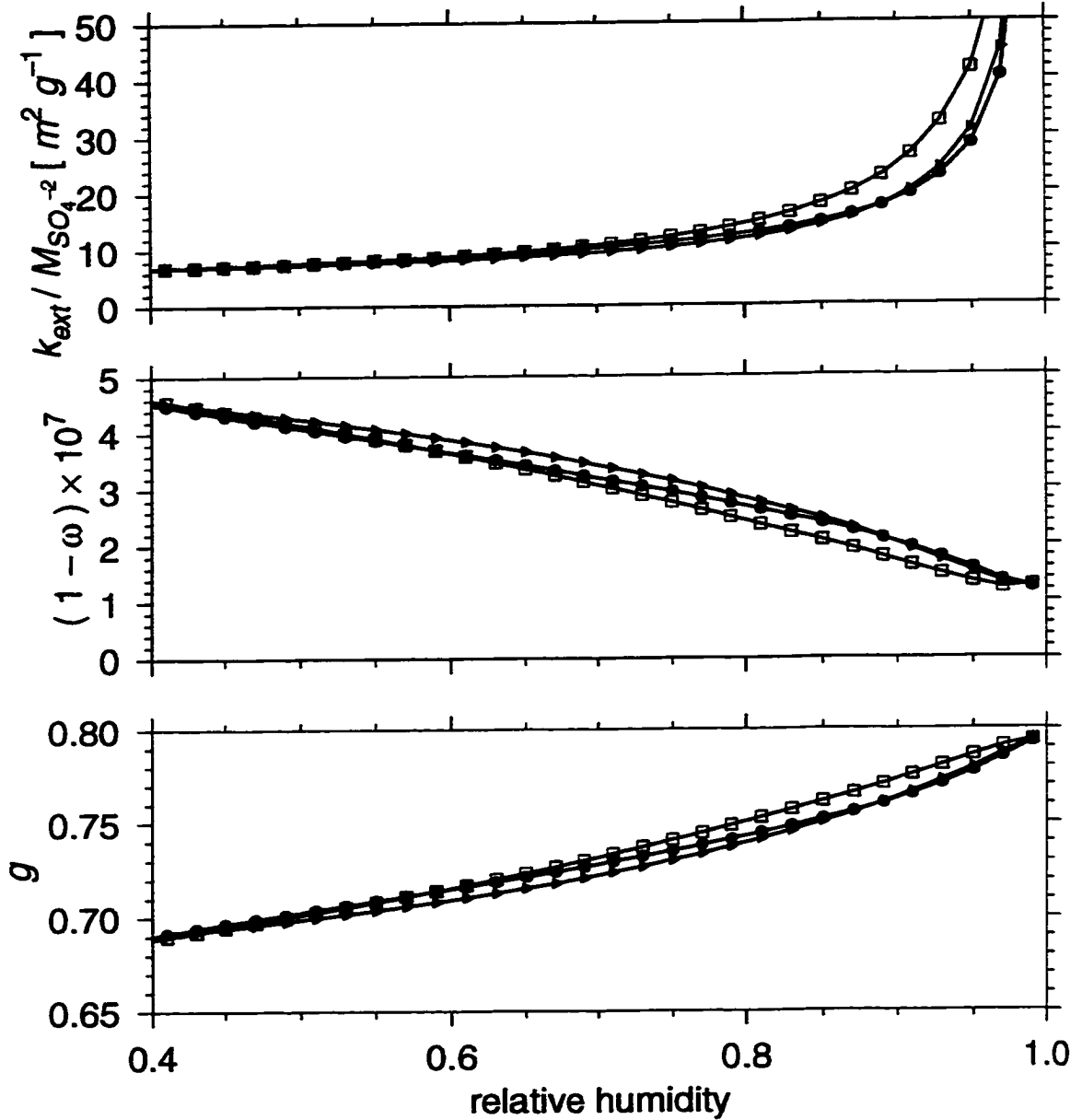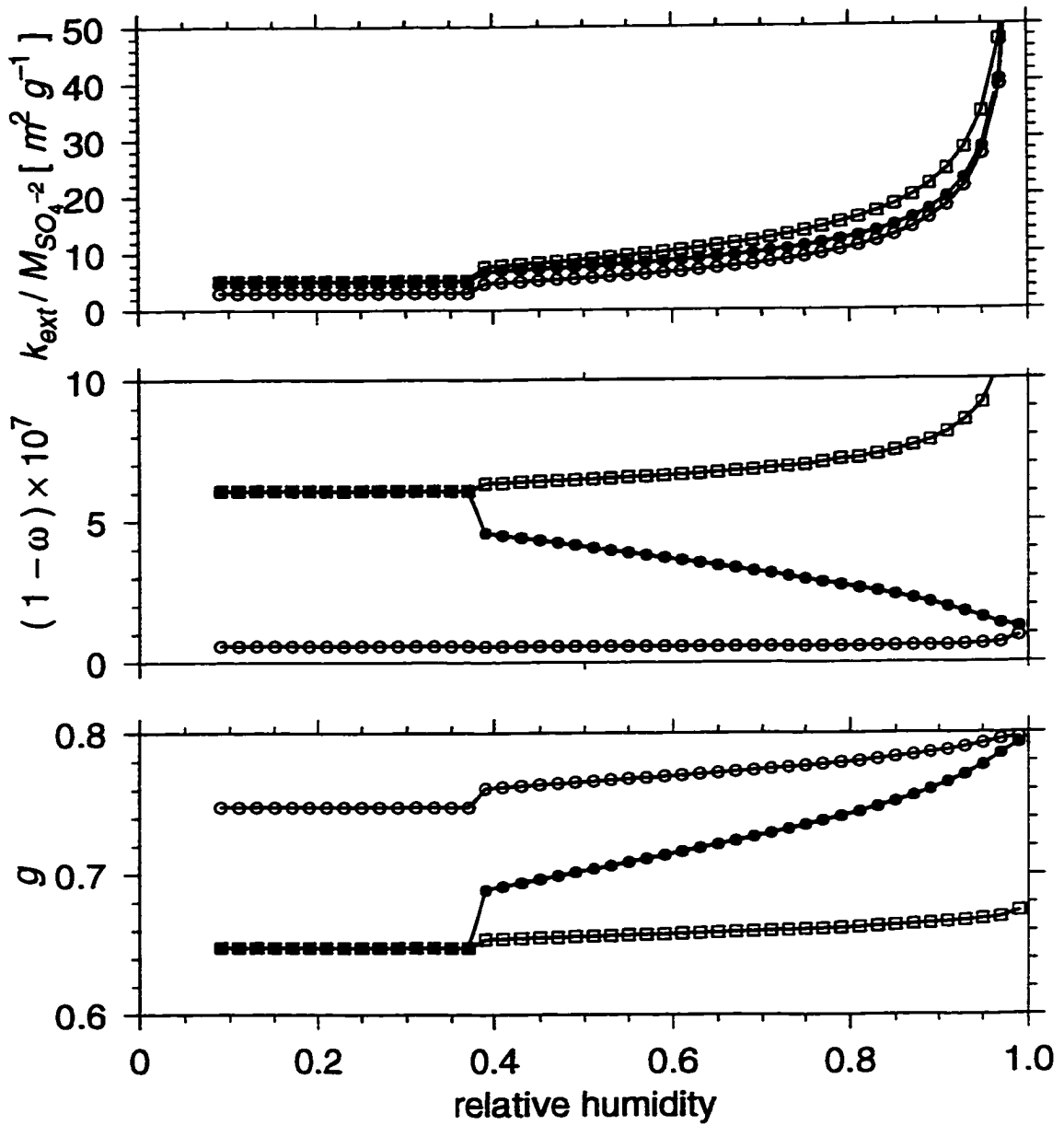
Figure 4.7: The specific extinction (top panel), single scattering co-albedo (middle), and asymmetry parameter (bottom) of a lognormal size distribution of $(NH_4)_2SO_4$ aerosol with $r_0 = 0.05\,\mu m$ and $\ln\sigma_0 = 0.7$ for the wavelength band between 0.20 and 0.69 μm as functions of relative humidity. The curve drawn with the • symbol uses the volume average mixing rule. The □ and o symbols correspond to using the refractive index of $(NH_4)_2SO_4$ and H_2O without using a mixing rule.

refractive index of water is used. In terms of radiative forcing, using the refractive index of $(NH_4)_2SO_4$ results in a forcing (plotted in figure 4.8) that is approximately a factor of two stronger than when the refractive index of water is used to obtain the optical properties of the aerosol. This indicates that the change in the refractive index of the aerosol due to the condensed water should not be ignored.

In chapter 2 the radiative properties and resulting radiative forcing of absorbing aerosols was seen to depend on the assumed size distribution of the aerosol. This is also true for hygroscopic aerosols. Figure 4.9 shows the effect of changing the initial r_0 and $\ln \sigma_0$ of the dry aerosol size distribution on the optical properties using the effective radius (equation 2.21) of the wet size distribution as the independent variable. In chapter 2, it was mentioned that aerosol size distributions with similar effective radii have similar optical properties (Lenoble 1993). Different dry size distributions of hygroscopic aerosols may have the same wet effective radius if they are exposed to different relative humidities. Particles from the distributions with the same radius have different amounts of condensed water which means that they have different refractive indices and optical properties. Figure 4.9 shows that for a given effective radius, the specific extinction and single scattering co-albedo vary by approximately an order of magnitude and the asymmetry parameter can vary by over 10%. Figure 4.10 demonstrates the effect of increasing the geometric mean radius of the lognormal size distribution of dry ammonium sulfate aerosols on the radiative forcing of the aerosol while keeping $\ln \sigma_0 = 0.7$ fixed. For a given relative humidity, the strongest forcing results from the size distribution with $r_0 = 0.05\,\mu m$ which has an effective radius of $0.17\,\mu m$. This is consistent with figure 4.9 where the specific extinction coefficient of the aerosol is a maximum when the effective radius of the dry aerosols is between $0.09\,\mu m$ and $0.20\,\mu m$.

The procedure of calculating the relative humidity dependent optical properties of ammonium sulfate aerosols can be applied in the same manner to other chemical species that are hygroscopic in nature. Differences in the optical properties can be attributed to the different rates at which aerosols of different chemical composition

Figure 4.8: The direct top-of-the-atmosphere radiative forcing of lognormal size distributions of $(NH_4)_2SO_4$ aerosol with $\ln \sigma_0 = 0.7$ as functions of relative humidity. The • symbols corresponds to using the volume average mixing rule. The □ and o uses the refractive index of $(NH_4)_2SO_4$ and H_2O respectively. The surface albedo is zero, the solar zenith angle is 60°, and the sulfate burden is $10^{-2}\,g\,m^{-2}$.

Figure 4.9: The specific extinction (top panel), single scattering co-albedo (middle), and asymmetry parameter (bottom) of lognormal size distributions of $(NH_4)_2SO_4$ aerosol as functions of wet r_{eff} for the wavelength band between 0.20 and 0.69 μm. Distributions with dry $r_0 = 0.05\,\mu$m are plotted with ■, •, and ▲ corresponding to dry $\ln\sigma_0 = 0.3$, 0.5, and 0.7 respectively. Distributions with dry $\ln\sigma_0 = 0.7$ and dry $r_0 = 0.10$ (○), 0.20 (◁), 0.40 (◇), and 0.80 μm (▷) are drawn.
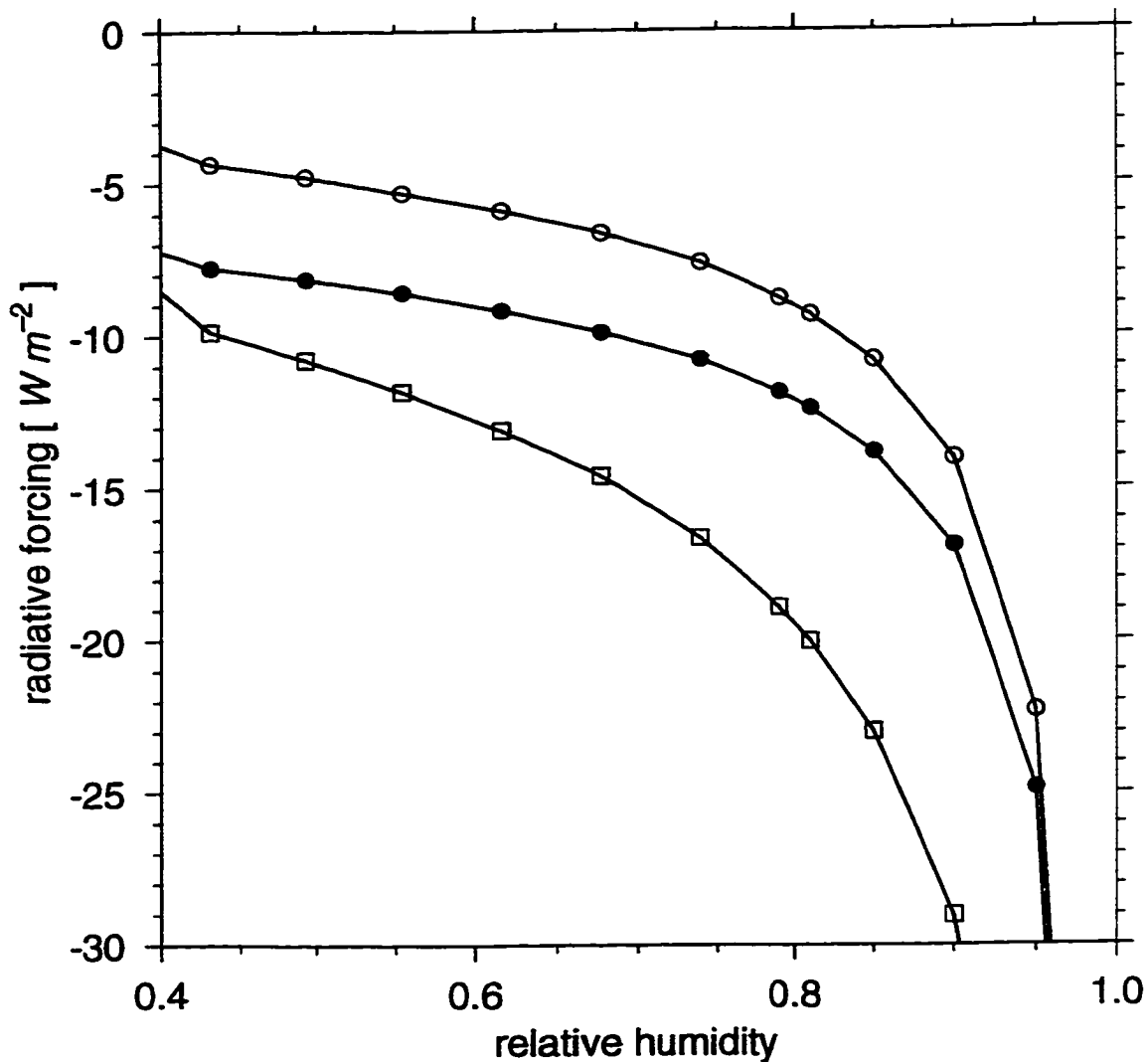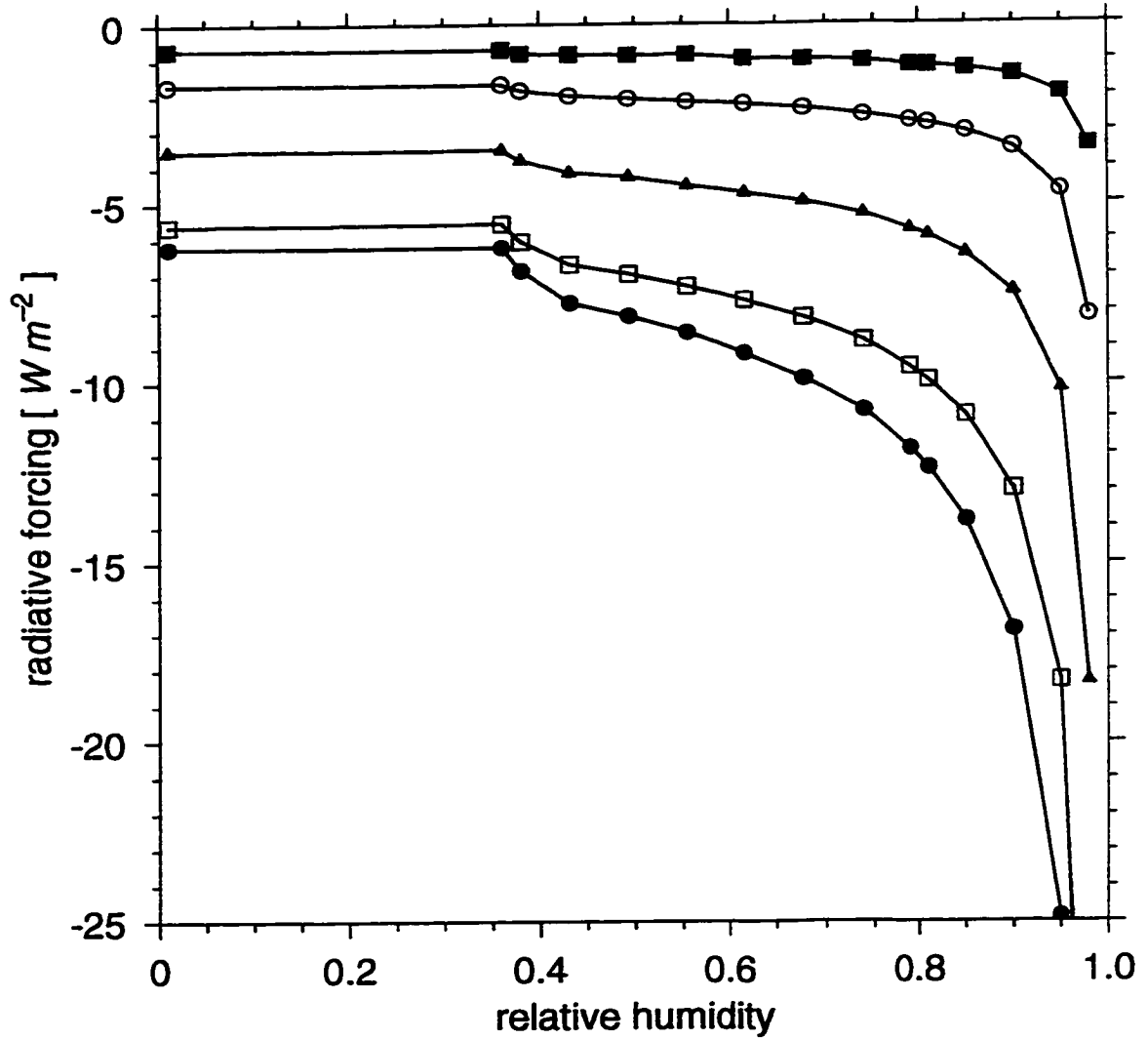
Figure 4.10: The direct top-of-the-atmosphere radiative forcing of lognormal size distributions of $(NH_4)_2SO_4$ aerosol with $\ln \sigma_0 = 0.7$ as functions of relative humidity. Curves with geometric mean radii of 0.05 (•), 0.10 (□), 0.20 (▲), 0.40 (◇), and 0.80 μm (■) are shown. The surface albedo is zero, the solar zenith angle is 60°, and the sulfate burden is $10^{-2}\,g\,m^{-2}$.

grow with relative humidity, and the refractive index of the dry particle.

Figure 4.11 plots the optical properties of the three dominant forms of sulfate aerosols in the atmosphere: sulfuric acid (o), ammonium bisulfate (□), and ammonium sulfate (•). Also plotted are the optical properties of nitric acid (*). Sulfuric acid has the strongest specific extinction of the sulfate aerosols followed by ammonium sulfate and then ammonium bisulfate. Though ammonium sulfate is a stronger absorber of radiation between $0.20\,\mu m$ and $0.69\,\mu m$ wavelengths than the other sulfates, it still does not absorb a significant amount of solar energy since the single scattering co-albedo is less than 10^{-6}. Sulfuric acid aerosols have the largest asymmetry parameter followed by ammonium bisulfate and then ammonium sulfate. Just above the crystallization point of ammonium sulfate, the asymmetry parameter of sulfuric acid is approximately 8% larger than that of ammonium sulfate. Just below the crystallization point, the difference is almost 15%.

The asymmetry parameter of nitric acid aerosols is larger than those of the sulfate aerosols considered. The extinction coefficient of nitric acid normalized by the mass concentration of nitrate (NO_3^-) is larger than the specific extinction coefficient of any of the considered sulfate aerosols. However, direct comparison of the specific extinction of nitrate and sulfate aerosols is misleading because the global annual average burden of sulfate aerosols is larger than the burden of nitrate aerosols (Schimel et al. 1996).

Figure 4.12 plots the normalized radiative forcing due to sulfate aerosols and nitric acid aerosols as functions of relative humidity. The normalized forcing is defined as

$$\Delta G = \frac{\Delta F_R}{B} \tag{4.8}$$

and has units of $W\,g^{-1}$ (Nemesure et al. 1995; Boucher and Anderson 1995). Figure 4.12 indicates that the radiative forcing of sulfate aerosols could vary by almost 30% when the relative humidity is approximately 0.80 depending on the amount of ammonia present in the environment which would influence the dominant form of sulfate. If the hysteresis effect of ammonium sulfate aerosol is considered, the range increases to approximately 60%. Sulfuric acid aerosols have the strongest normalized
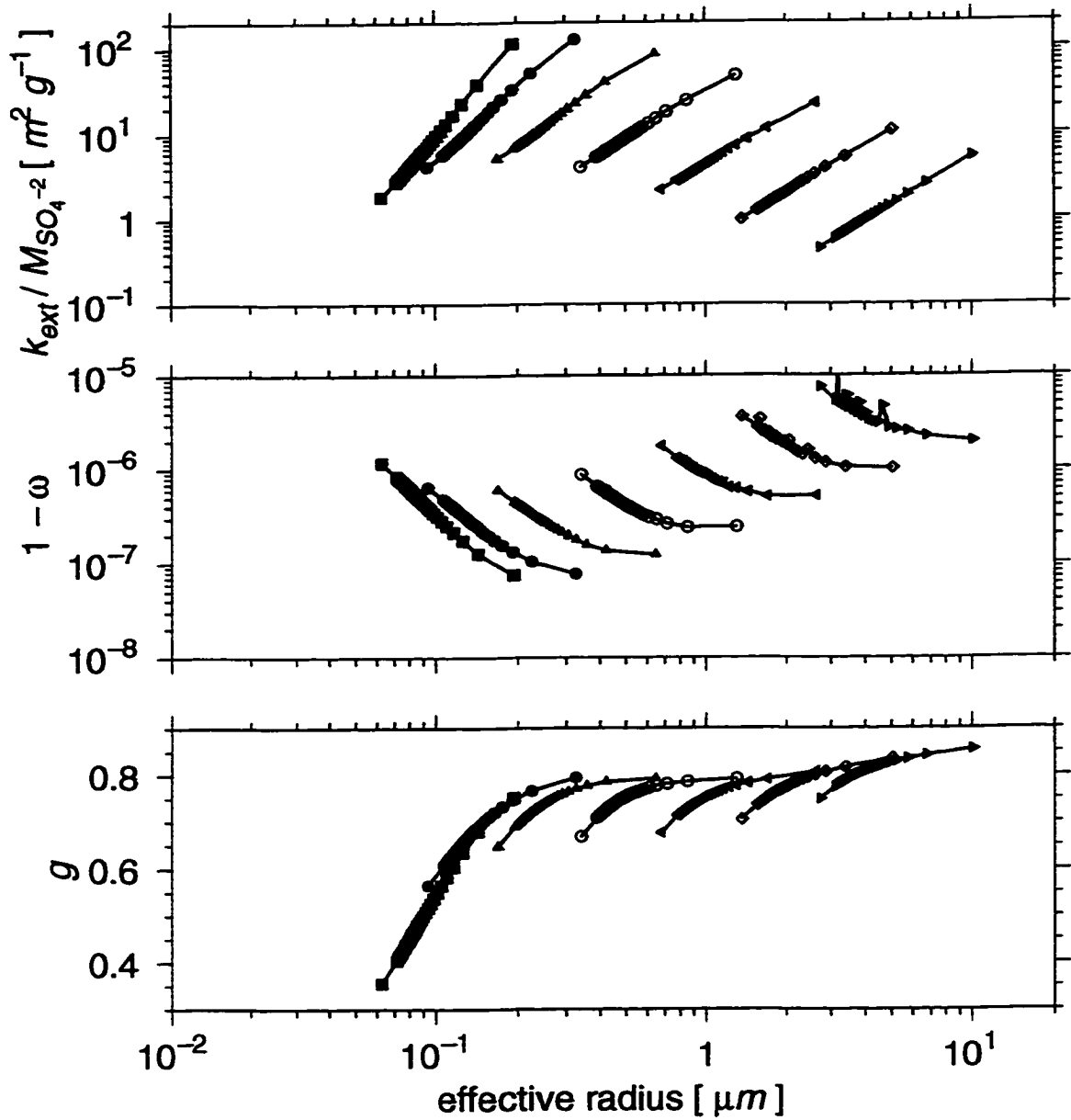
Figure 4.11: The specific extinction coefficient (top panel), single scattering co-albedo (middle), and asymmetry parameter (bottom) of a lognormal size distribution of wet $(NH_4)_2SO_4$ (●), NH_4HSO_4 (□), H_2SO_4 (○), and HNO_3 (∗) aerosol with $r_0 = 0.05\,\mu m$ and $\ln\sigma_0 = 0.7$ for the wavelength band between 0.20 and 0.69 μm as functions of relative humidity.

Figure 4.12: The direct top-of-the-atmosphere normalized radiative forcing of a log-normal size distribution of wet $(NH_4)_2SO_4$ ($\bullet$), NH_4HSO_4 ($\square$), H_2SO_4 ($\circ$), and HNO_3 ($*$) aerosol with $r_0 = 0.05\,\mu m$ and $\ln\sigma_0 = 0.7$ as functions of relative humidity. The surface albedo is zero, the solar zenith angle is $60°$, and the sulfate or nitrate burden is $10^{-2}\,g\,m^{-2}$.

forcing while ammonium bisulfate has the weakest. The normalized forcing due to wet ammonium sulfate aerosols is stronger than that of ammonium bisulfate, but if the ammonium sulfate aerosol is dry, they will have a lower normalized forcing than ammonium bisulfate. Boucher and Anderson (1995) and Nemesure et al. (1995) found similar sensitivities to sulfate composition.

Even though nitric acid aerosols have the strongest normalized forcing when the relative humidity is greater than 0.70, little attention has been paid to the radiative forcing due to nitrate aerosols (Pilinis et al. 1995). This is because the burden of sulfate aerosols is estimated to be a factor of 5 greater than that of nitrate aerosols (Schimel et al. 1996). Therefore the radiative forcing of sulfate aerosols will be larger than the forcing due to nitrate aerosols by approximately the same factor.

The optical properties of sea salt aerosols are shown in figure 4.13. The size distribution considered has the lognormal parameters of $r_0 = 0.40\,\mu m$ and $\ln \sigma_0 = 0.3$ which is the same accumulation mode size distribution considered by Winter and Chýlek (1997). The curve drawn with • symbols is calculated with the Köhler equation with a concentration dependent van't Hoff factor (Tang et al. 1997). Using the Gerber parameterization for aerosol growth results in the curves drawn with the ▷ symbols. In chapter 3 it was shown that the Gerber parameterization underestimates the mass growth factor of sea salt. This leads to an underestimation in the extinction coefficient normalized by the total mass concentration of sea salt and the asymmetry parameter. The effect of these underestimates on the radiative forcing is shown in figure 4.14. At 0.85 relative humidity, the relative difference in the forcing obtained with the Gerber parameterization relative to using a concentration dependent i in the Köhler equation is -26%. This large difference makes the Gerber parameterization for sea salt too inaccurate for use in radiative forcing studies. Using a constant van't Hoff factor of 2.0 leads to a difference of -30% at relative humidities around 0.55 which decreases to -16% at 0.85 relative humidity. Winter and Chýlek (1997) demonstrated that the global annual average radiative forcing values of $-2.0\,\mathrm{W\,m^{-2}}$ are possible when the relative humidity is between 0.70 and 0.85.
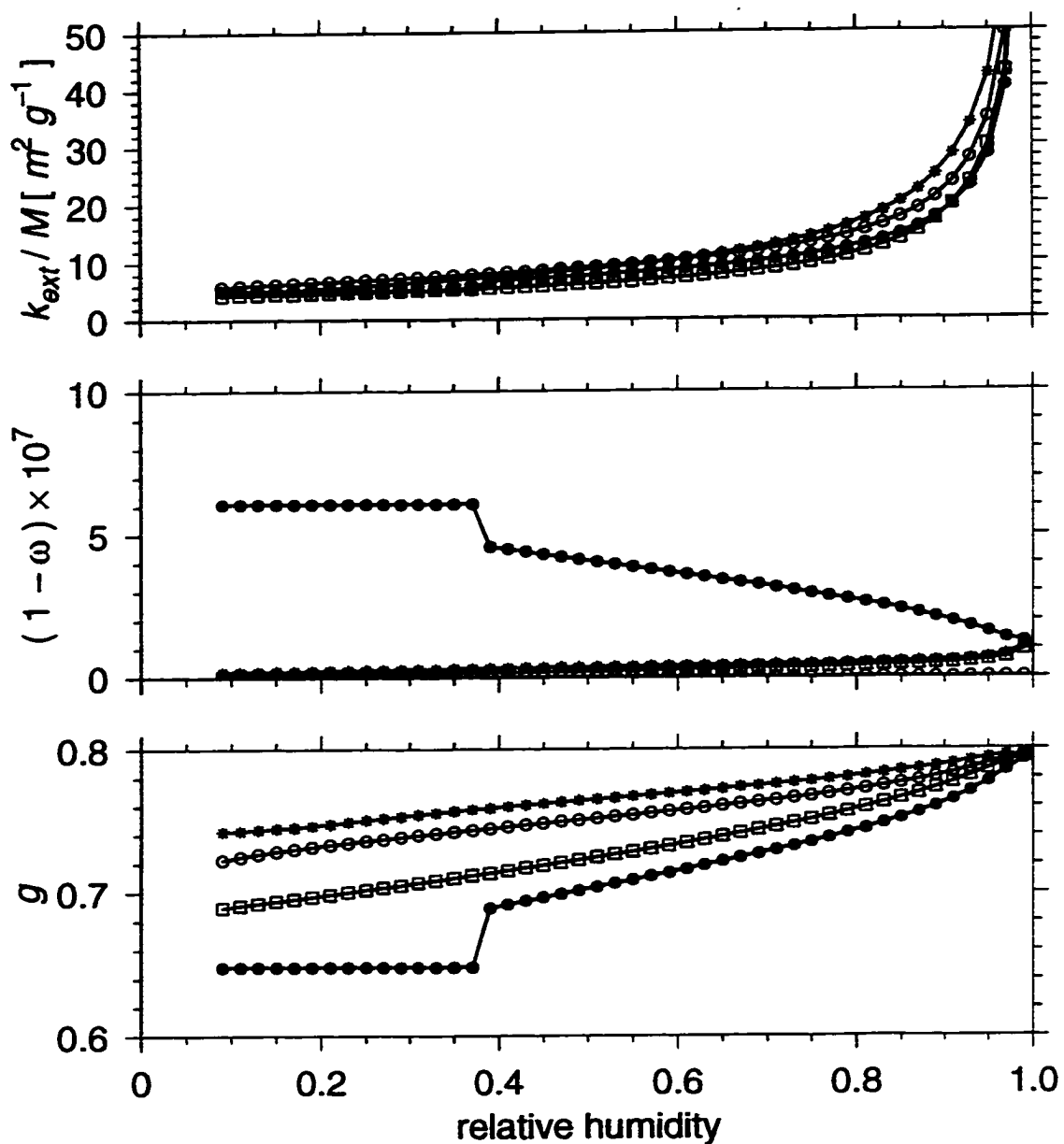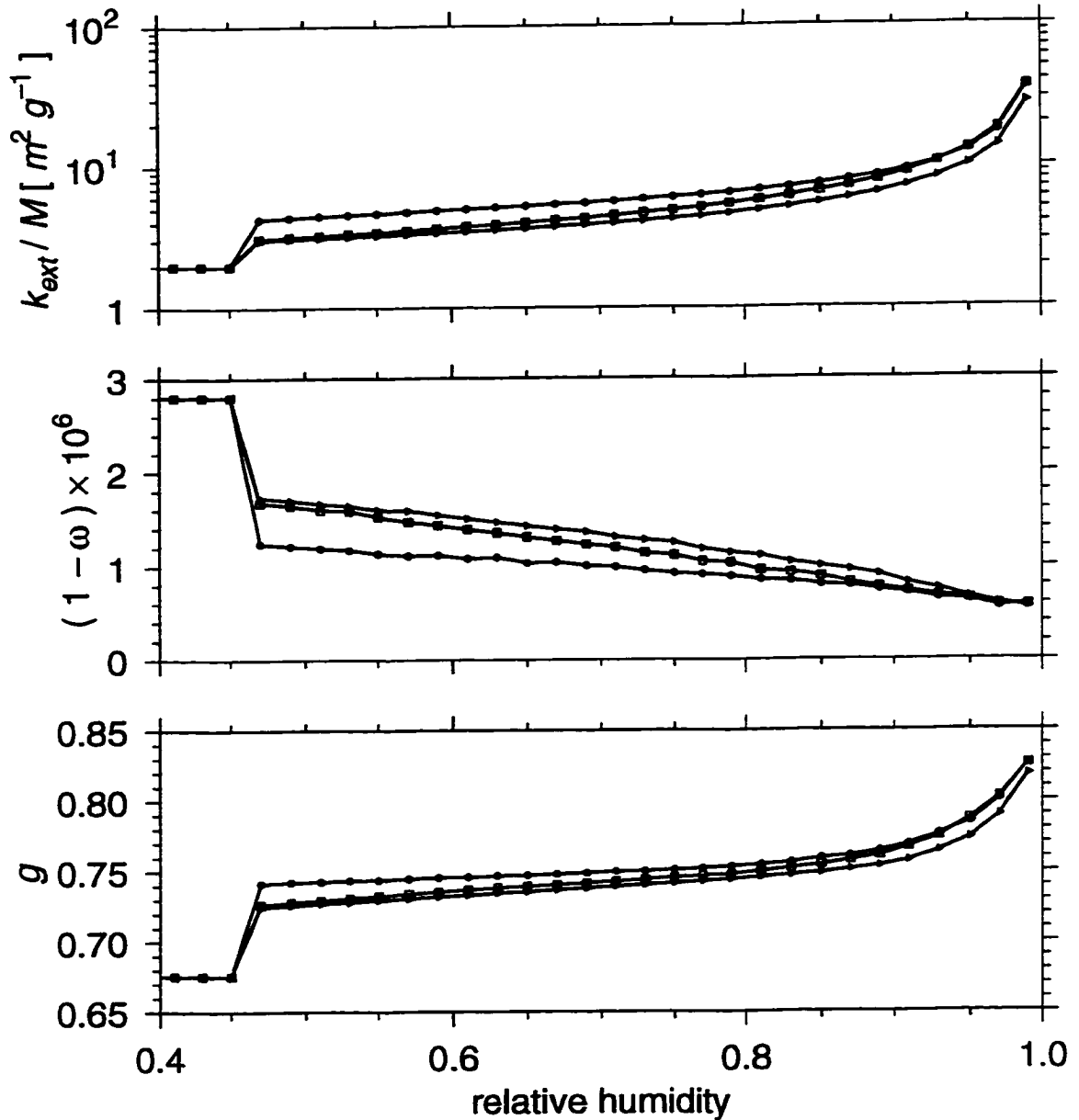
Figure 4.13: The specific extinction coefficient (top panel), single scattering co-albedo (middle), and asymmetry parameter (bottom) of a lognormal size distribution of sea salt ($\triangleright$) aerosol with $r_0 = 0.40\,\mu\text{m}$ and $\ln\sigma_0 = 0.3$ for the wavelength band bet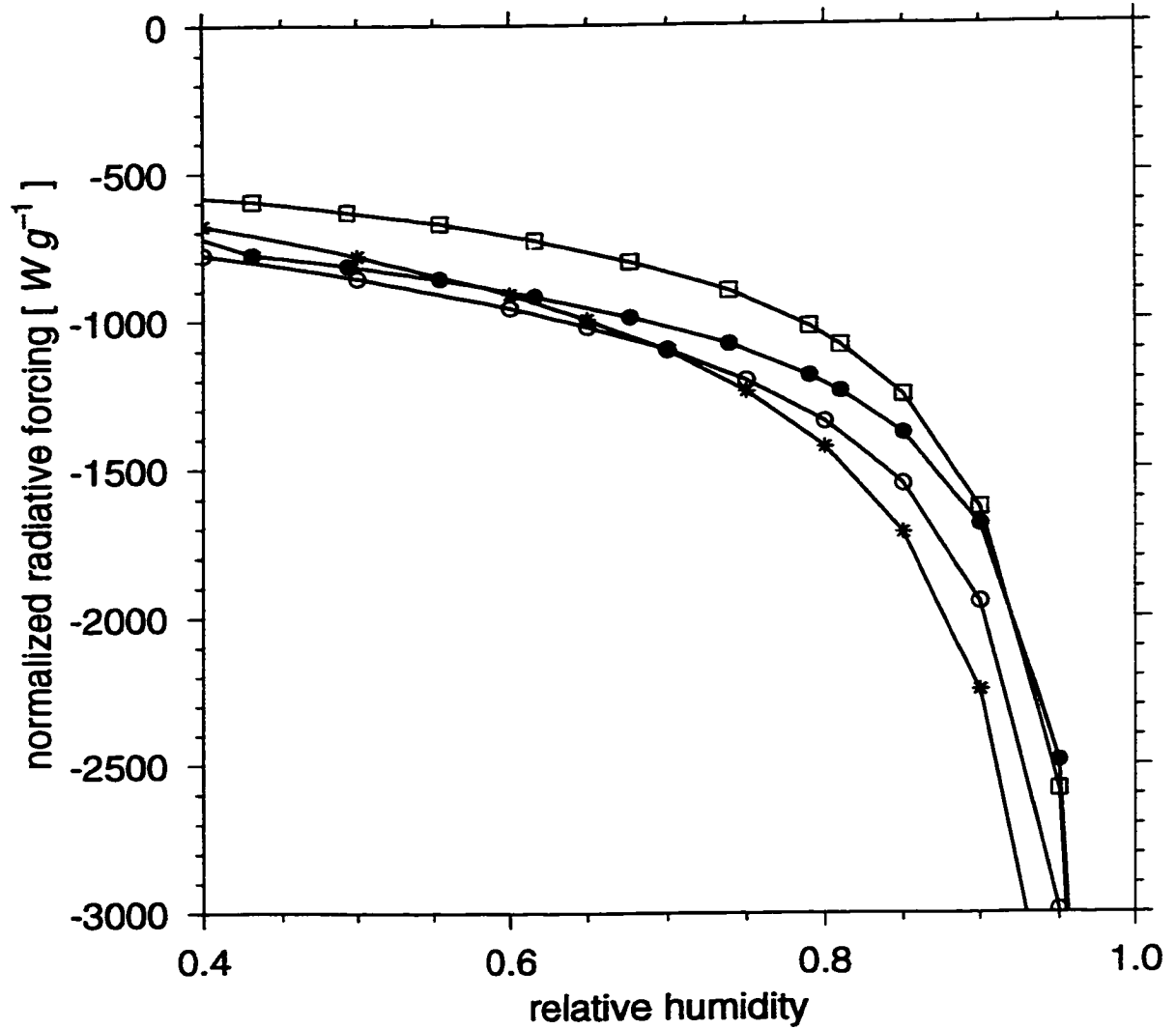ween 0.20 and 0.69 μm as functions of relative humidity. The values are calculated with the Köhler equation with a variable i ($\bullet$), a constant $i = 2.0$ ($\square$), and with the Gerber parameterization ($\triangleright$).
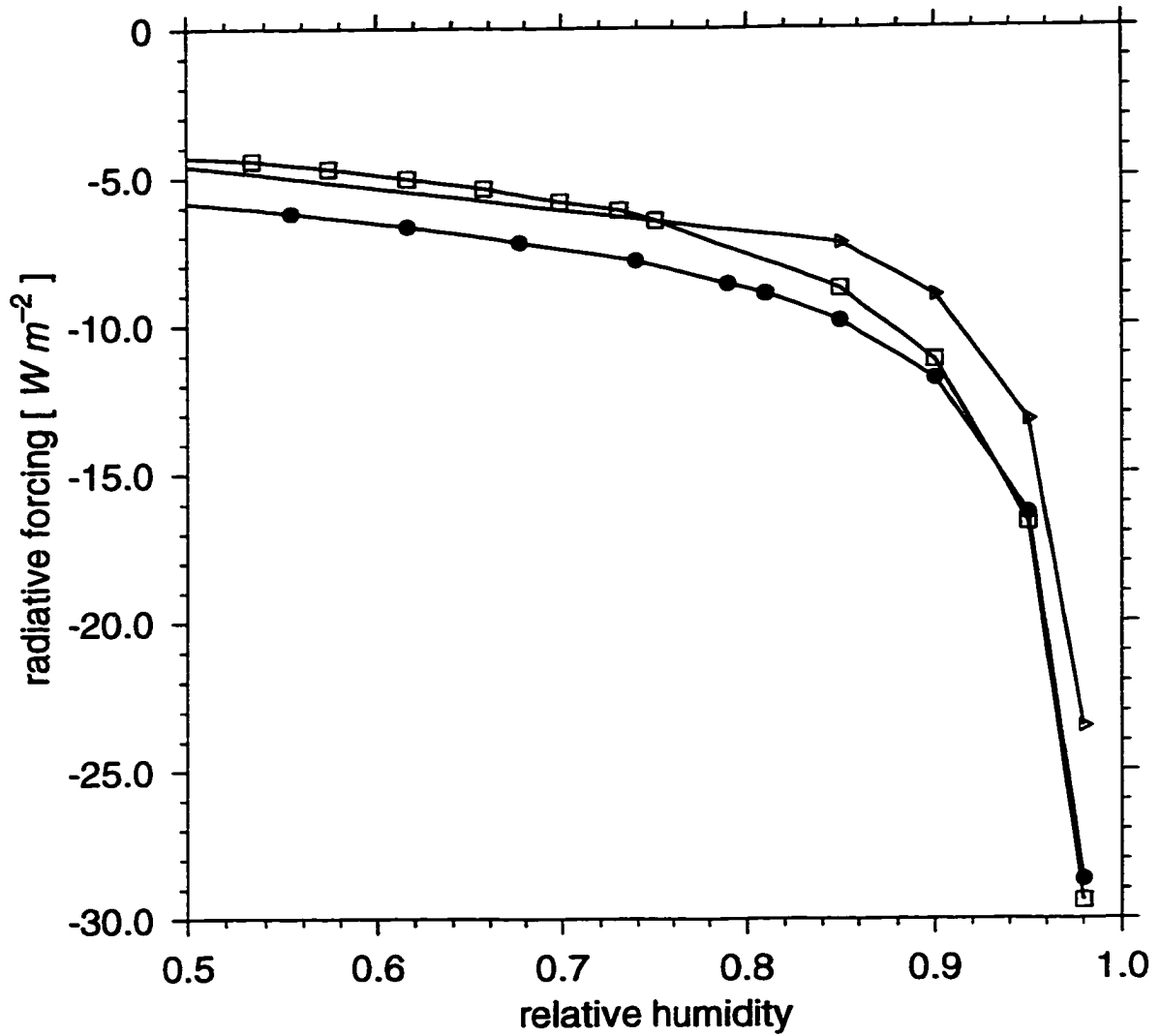
Figure 4.14: The direct top-of-the-atmosphere radiative forcing of a lognormal size distribution of wet sea salt aerosol with $r_0 = 0.40\,\mu m$ and $\ln\sigma_0 = 0.3$ as functions of relative humidity. The values are calculated with the Köhler equation with a variable i (•), a constant $i = 2.0$ (□), and with the Gerber parameterization (▷). The surface albedo is zero, the solar zenith angle is $60°$, and the sea salt aerosol burden is $10^{-2}\,g\,m^{-2}$.

4.3 Latitudinal Distribution of Radiative Forcing

Part of the difficulties in assessing the global climatic impact of sulfate aerosol is that the aerosol is not uniformly distributed over the planet and its atmospheric lifetime varies. Bondietti and Papastefanou (1993) estimate that the atmospheric lifetime is approximately seven days.

At a given time, conditions such as aerosol burden, solar zenith angle, and surface albedo change from location to location. The relative humidity is also different at each point. Figures 4.15, 4.16, and 4.17 show the broadband radiative forcing of sulfate aerosol as a function of sulfate burden, surface albedo, and solar zenith angle respectively for relative humidities ranging from 0.36 to 0.95. The dependence on sulfate burden is approximately linear which is not surprising since it is consistent with radiative forcing equation 2.1 in chapter 2. This equation applies to thin aerosol layers ($\tau \lesssim 1$) and it shows a linear dependence in optical depth. For a sulfate burden of $0.01\,\mathrm{g\,m^{-2}}$, the optical depth is approximately 0.3 when the relative humidity is 0.95. This equation also indicates that the forcing should decrease in magnitude as the surface albedo increases due to multiple scattering between the surface and aerosol layer. This trend is seen in figure 4.16. The radiative forcing is also dependent on the solar zenith angle — which is related to the time of day. These figures demonstrate that the radiative forcing due to aerosol will vary considerably with time and location.

Kiehl and Rodhe (1995) calculated the annual global distribution of direct radiative forcing of sulfate aerosol. Their model used the same radiative transfer routines as in the second version of the Community Climate Model (CCM2) produced by the National Center for Atmospheric Research (NCAR). This three dimensional model used a horizontal grid with a resolution of $2.8° \times 2.8°$ and 18 vertical atmospheric layers to represent the surface and atmosphere system. The radiative forcing was calculated using monthly mean data of quantities such as aerosol concentration for each grid box. The monthly radiative forcing were then averaged to obtain the annual average.

The distribution of sulfate aerosol was simulated using the Pham et al. (1995)

Figure 4.15: The broadband radiative forcing as a function of sulfate burden of a size distribution of $(NH_4)_2SO_4$ aerosol with $r_0 = 0.05\,\mu m$ and $\ln\sigma_0 = 0.7$. The surface albedo is zero and the solar zenith angle is 60°. Curves are drawn for relative humidities of 0.36 (■), 0.62 (●), 0.74 (◆), 0.81 (▲), 0.90 (□), and 0.95 (○).
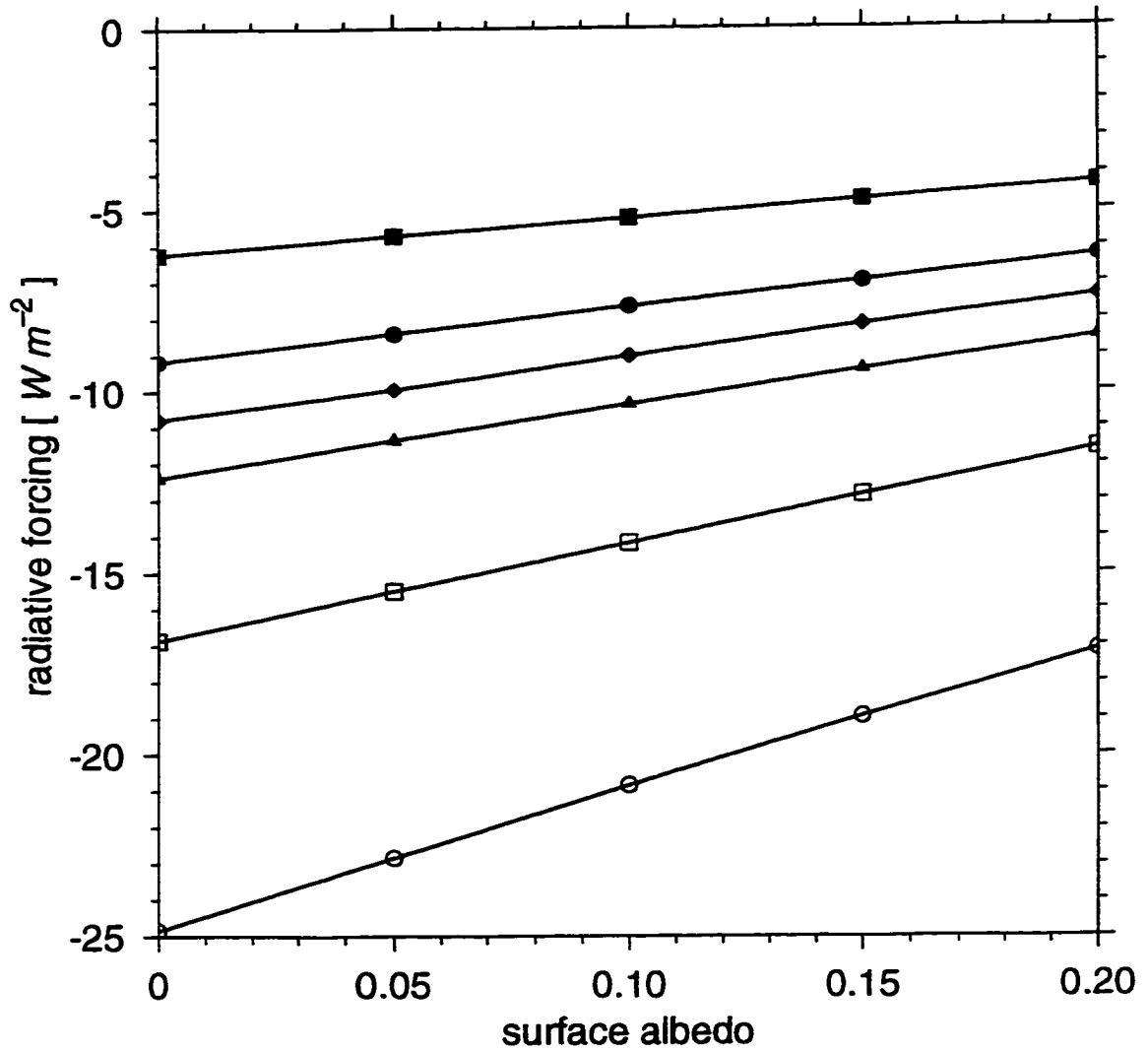
Figure 4.16: The broadband radiative forcing as a function of surface albedo of a size distribution of $(NH_4)_2SO_4$ aerosol with $r_0 = 0.05\,\mu m$ and $\ln\sigma_0 = 0.7$. The sulfate aerosol burden is $10^{-2}\,g\,m^{-2}$ and the solar zenith angle is $60°$. Curves are drawn for relative humidities of 0.36 (■), 0.62 (●), 0.74 (♦), 0.81 (▲), 0.90 (□), and 0.95 (○).
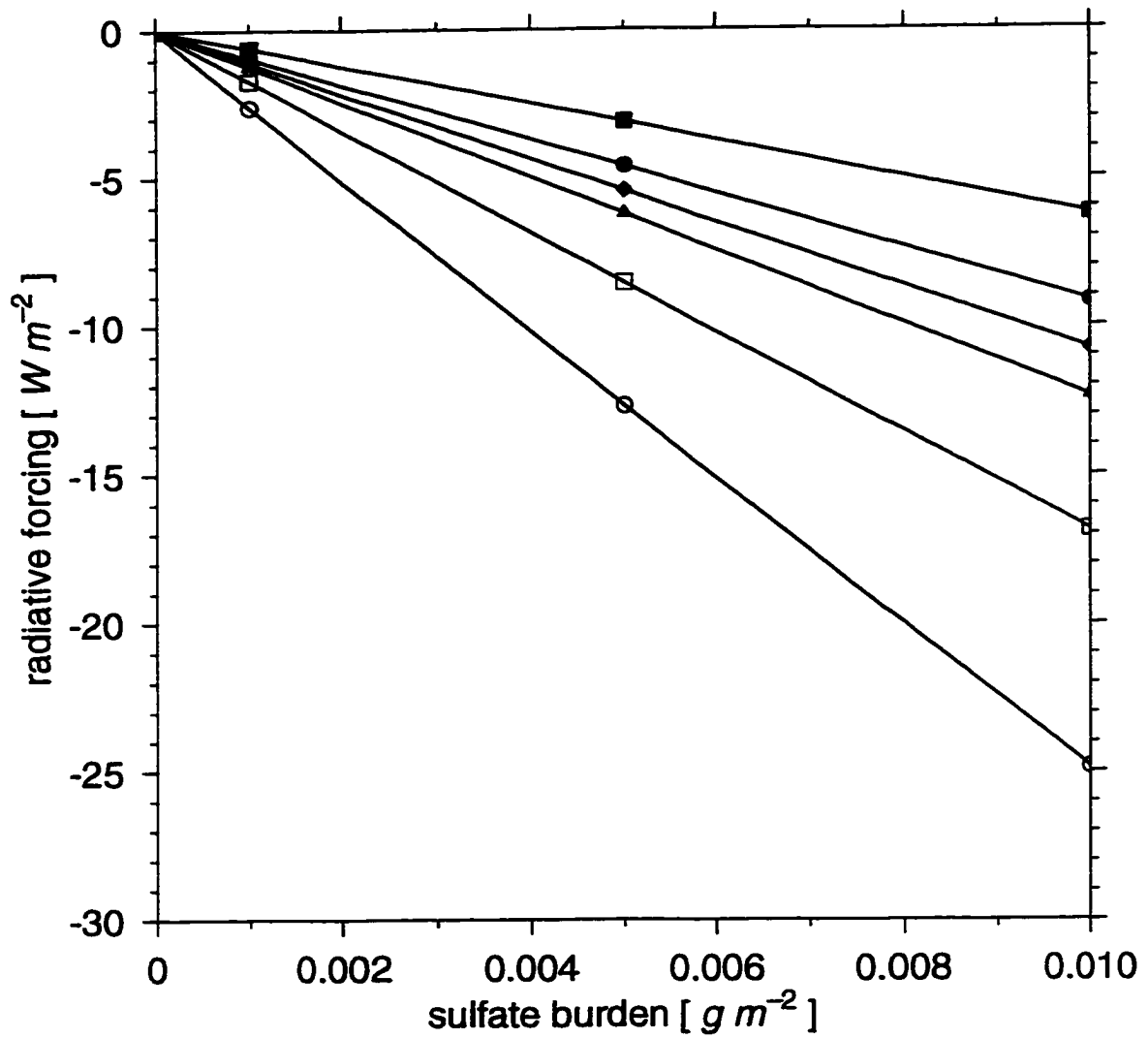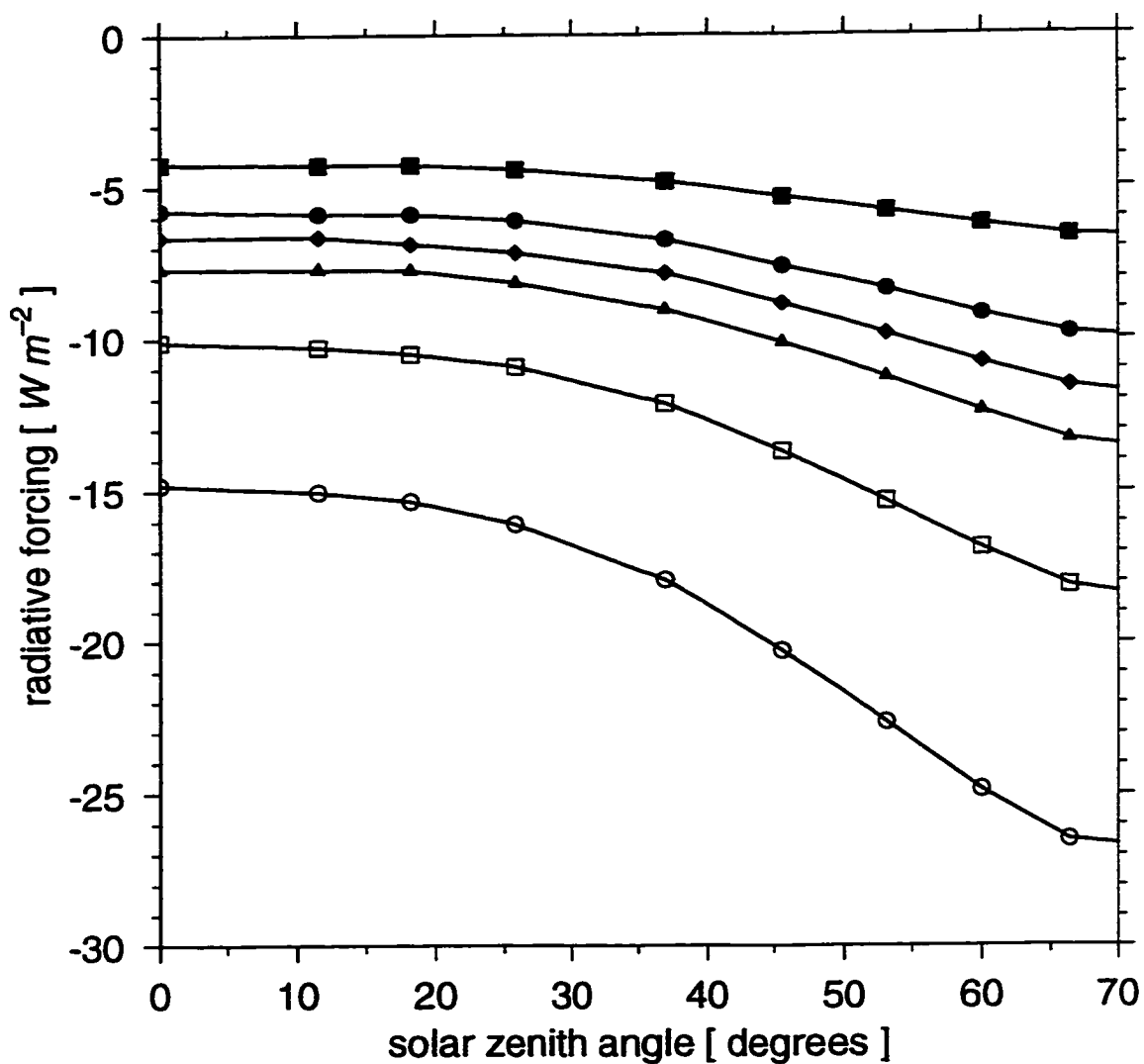
Figure 4.17: The broadband radiative forcing as a function of solar zenith angle of a size distribution of $(NH_4)_2SO_4$ aerosol with $r_0 = 0.05\,\mu m$ and $\ln \sigma_0 = 0.7$. The sulfate aerosol burden is $10^{-2}\,g\,m^{-2}$ and the surface albedo is zero. Curves are drawn for relative humidities of 0.36 (■), 0.62 (●), 0.74 (♦), 0.81 (▲), 0.90 (□), and 0.95 (○).

chemical transport model. Figure 4.18 illustrates the annual average global distribution of anthropogenic sulfate predicted by this model. The global average burden is $3.7 \times 10^{-3}\,\mathrm{g\,m^{-2}}$. It was assumed that sulfate aerosols are sulfuric acid particles with a lognormal size distribution with $r_0 = 0.05\,\mu\mathrm{m}$ and $\ln \sigma_0 = 0.7$. The relative humidity for each grid point was derived from monthly mean temperature and moisture data for the year 1989 from the European Centre for Medium Range Weather Forecasting. Figure 4.19 shows the annual average relative humidity at the surface.

The spatial distribution of radiative forcing due to anthropogenic sulfate aerosols is shown in figure 4.20. The strongest radiative forcing occurs over eastern China, central Europe, and the east coast of North America which are also the regions with high concentrations of sulfate. The relative humidity in those regions are also high.

The extinction coefficient, single scattering albedo, and asymmetry parameter are all affected by relative humidity. But in the studies by Kiehl and Briegleb (1993) and Kiehl and Rodhe (1995), only the extinction coefficient is treated for relative humidity effects. An improvement over previous results can be obtained by using the relative humidity dependent optical properties presented in the previous section. Figure 4.21 plots the specific extinction coefficient for the wavelength band between 0.35 and $0.70\,\mu\mathrm{m}$ used in the original Kiehl and Briegleb (1993) calculations ($\square$) along with the new values ($\bullet$) obtained using the relative humidity effect described in the previous sections. The relative humidity dependence of the new specific extinction coefficient is stronger than those used previously by Kiehl and Briegleb (1993) which was based on empirical observations of atmospheric aerosols (Charlson et al. 1984).

The optical properties are parameterized with the following functional form:

$$\ln\left(\frac{\zeta(rh)}{\zeta(rh=0)}\right) = a_0 + \frac{a_1}{rh + a_2} + \frac{a_3}{(rh + a_4)^2} \tag{4.9}$$

where $\zeta(rh)$ represents the specific extinction, single scattering co-albedo, or asymmetry parameter when the relative humidity is rh. The fitted coefficients, a, are obtained by a non-linear least squares minimization routine for each wavelength band. Table 4.2 tabulates the wavelength bands used by the NCAR CCM2 radiation model (Briegleb 1992). The fitted coefficients are different for each chemical form and initial
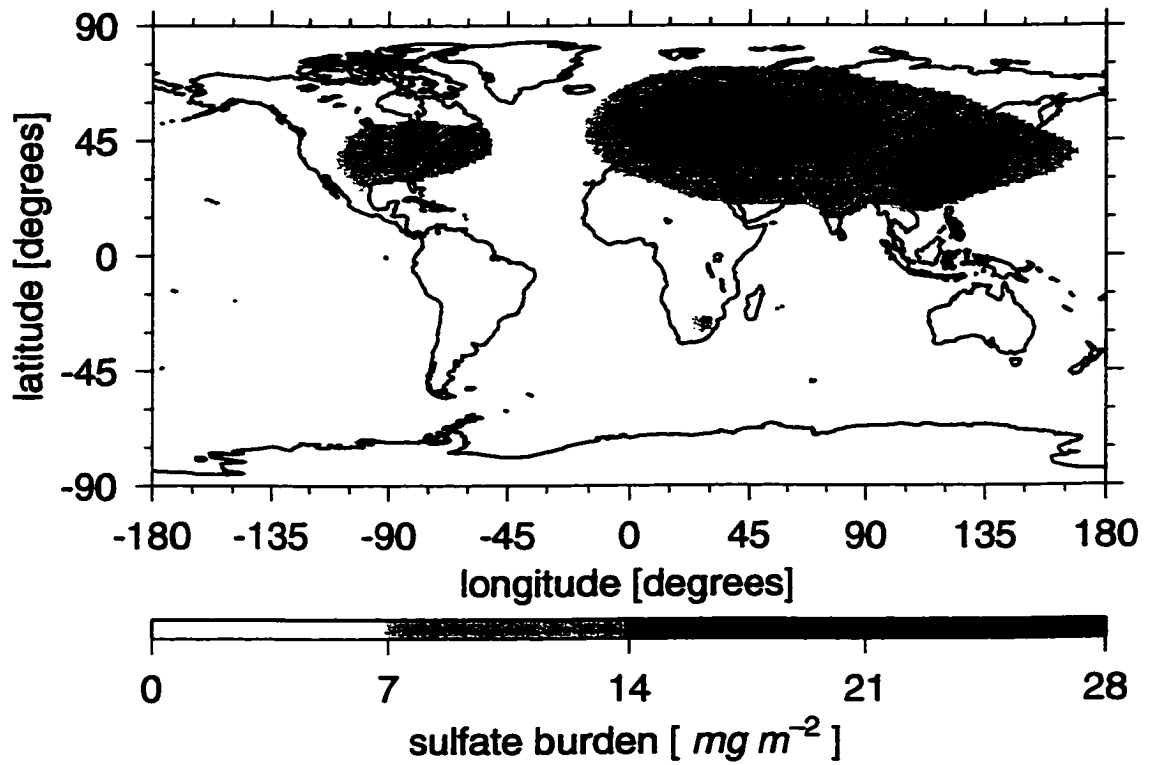
Figure 4.18: The annual average global distribution of anthropogenic sulfate aerosol predicted from the Pham et al. (1995) model. The global annual average burden is $3.7 \times 10^{-3}\,\mathrm{g\,m^{-2}}$.
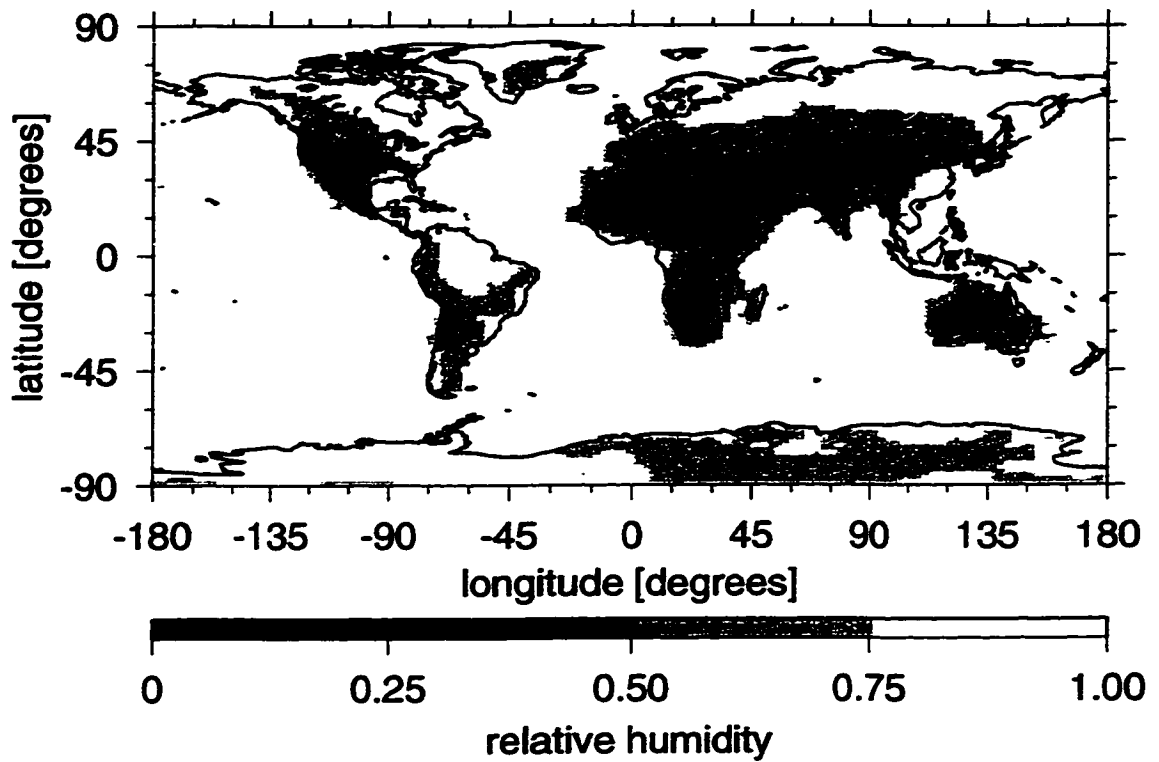
Figure 4.19: The annual average global relative humidity at the surface derived from temperature and moisture data for the year 1989 from the European Centre for Medium Range Weather Forecasting. The global annual average relative humidity is 0.80.
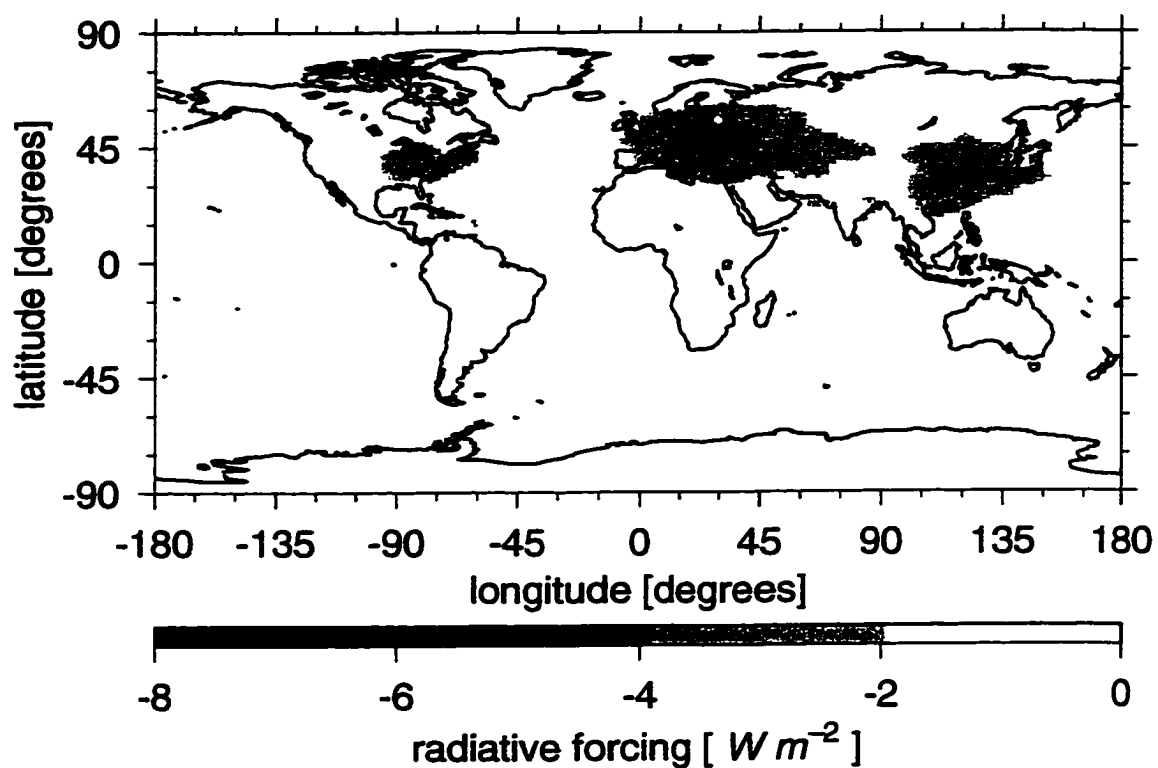
Figure 4.20: The annual average global distribution of anthropogenic sulfate aerosol forcing obtained using relative humidity dependent optical properties (Kiehl and Rodhe 1995). The global annual average forcing is $-0.56\,\mathrm{W\,m^{-2}}$.
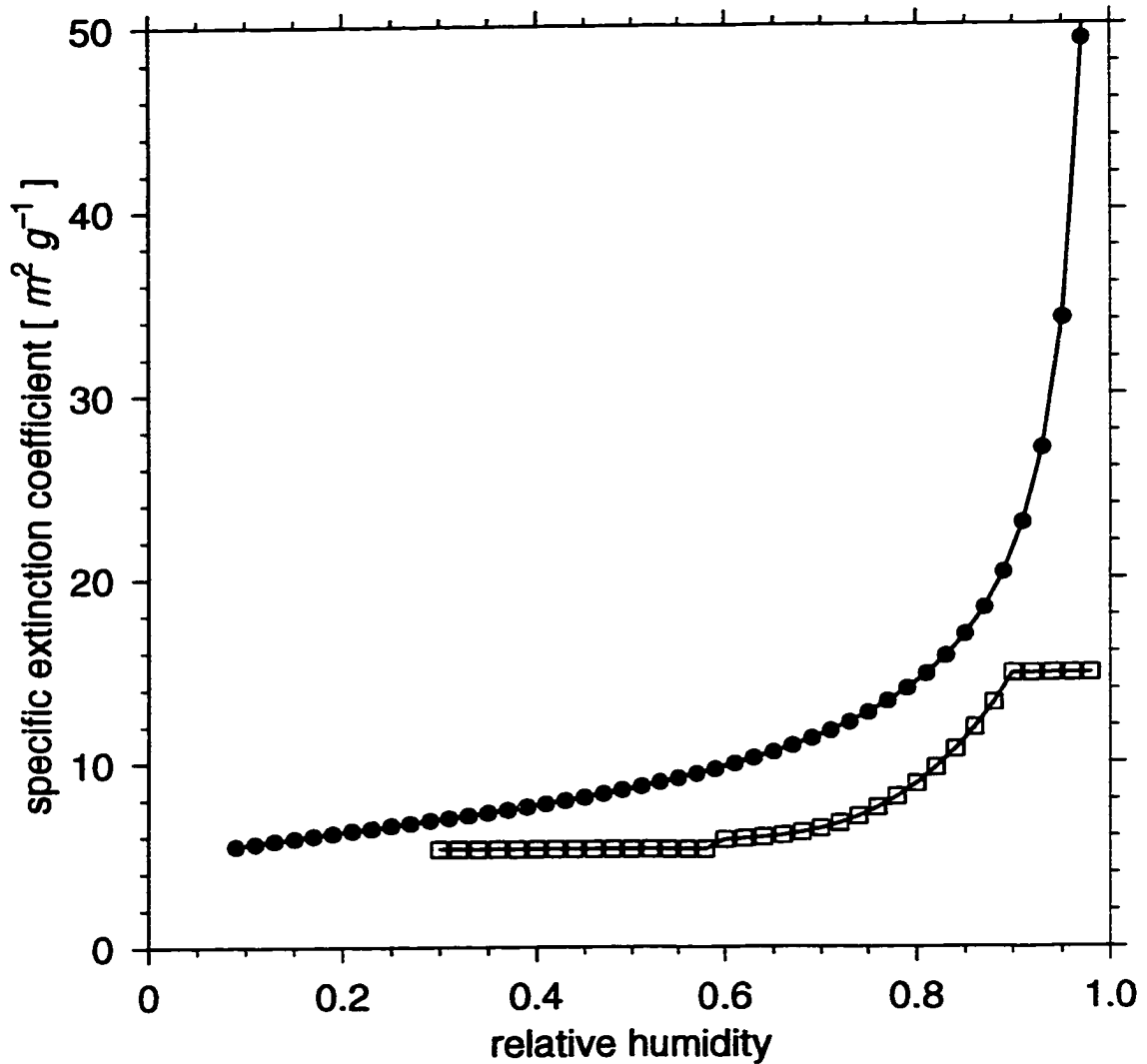
Figure 4.21: The new relative humidity dependent specific extinction coefficient of sulfuric acid aerosols (●) compared with the treatment used in the original Kiehl and Briegleb (1993) calculations (□) for the wavelength band between 0.35 and 0.70 μm. The size distribution of the aerosol has the lognormal parameters of $r_0 = 0.05$ μm and $\ln \sigma_0 = 0.7$.

band	minimum wavelength [μm]	maximum wavelength [μm]
1	0.200	0.245
2	0.245	0.265
3	0.265	0.275
4	0.275	0.285
5	0.285	0.295
6	0.295	0.305
7	0.305	0.350
8	0.350	0.700
9	0.700	1.089
10	1.089	1.408
11	1.408	1.749
12	1.749	2.152
13	2.152	2.714
14	2.714	3.457
15	3.457	5.000
16	2.630	2.860
17	4.160	4.475
18	4.475	4.550

Table 4.2: Solar wavelength bands of the NCAR CCM2 model.

dry size distribution. This parameterization is incorporated into the radiation model used in the previous calculations (NCAR CCM) and the global distribution of sulfate aerosol direct radiative forcing in an annual average is re-calculated.

The pattern of the spatial distribution of radiative forcing is slightly changed when the new relative humidity dependent optical properties are used. The difference in the two calculations is more easily seen when radiative forcing is zonally integrated. The zonally integrated radiative forcing of both calculations are plotted together in figure 4.22 as functions of latitude. The solid curve corresponds to the calculations that use optical properties that are all relative humidity dependent and the dotted line corresponds to the results when only the extinction coefficient is dependent on relative humidity. Figure 4.22 shows that use of the new aerosol optical properties that are all relative humidity dependent results in stronger radiative forcing at all latitudes. In both cases, the strongest forcing occurs at latitudes around $45°$ North latitude where the average sulfate burden is $12.3 \, \mathrm{g \, m^{-2}}$. Using the new optical properties results in an increase of 17% in the average forcing at that latitude to $-2.3 \, \mathrm{W \, m^{-2}}$. At $80°$ North latitude, the average radiative forcing is $-0.44 \, \mathrm{W \, m^{-2}}$ which is a factor of approximately 3 larger than the results obtained when the old specific extinction is used. The reason for this large change is that the average relative humidity is 0.94 at this latitude and Kiehl and Briegleb (1993) did not further increase the specific extinction when the relative humidity was greater than 0.80 (figure 4.21). Most of the anthropogenic aerosol is located in the northern hemisphere where the average burden is $6.5 \, \mathrm{g \, m^{-2}}$ compared to $0.9 \, \mathrm{g \, m^{-2}}$ for the southern hemisphere. Table 4.3 lists the global annual average direct radiative forcing of anthropogenic sulfate aerosol when the new and original optical properties are used. The northern and southern hemispheric averages are also listed. Results obtained by other research groups are also tabulated for comparison. Direct comparison of the results obtained by the different research groups is difficult due to the different assumptions in the chemical form and size distribution of the aerosol, the different treatments of hygroscopic growth, differences in the spatial and temporal distribution of the aerosol, and the different
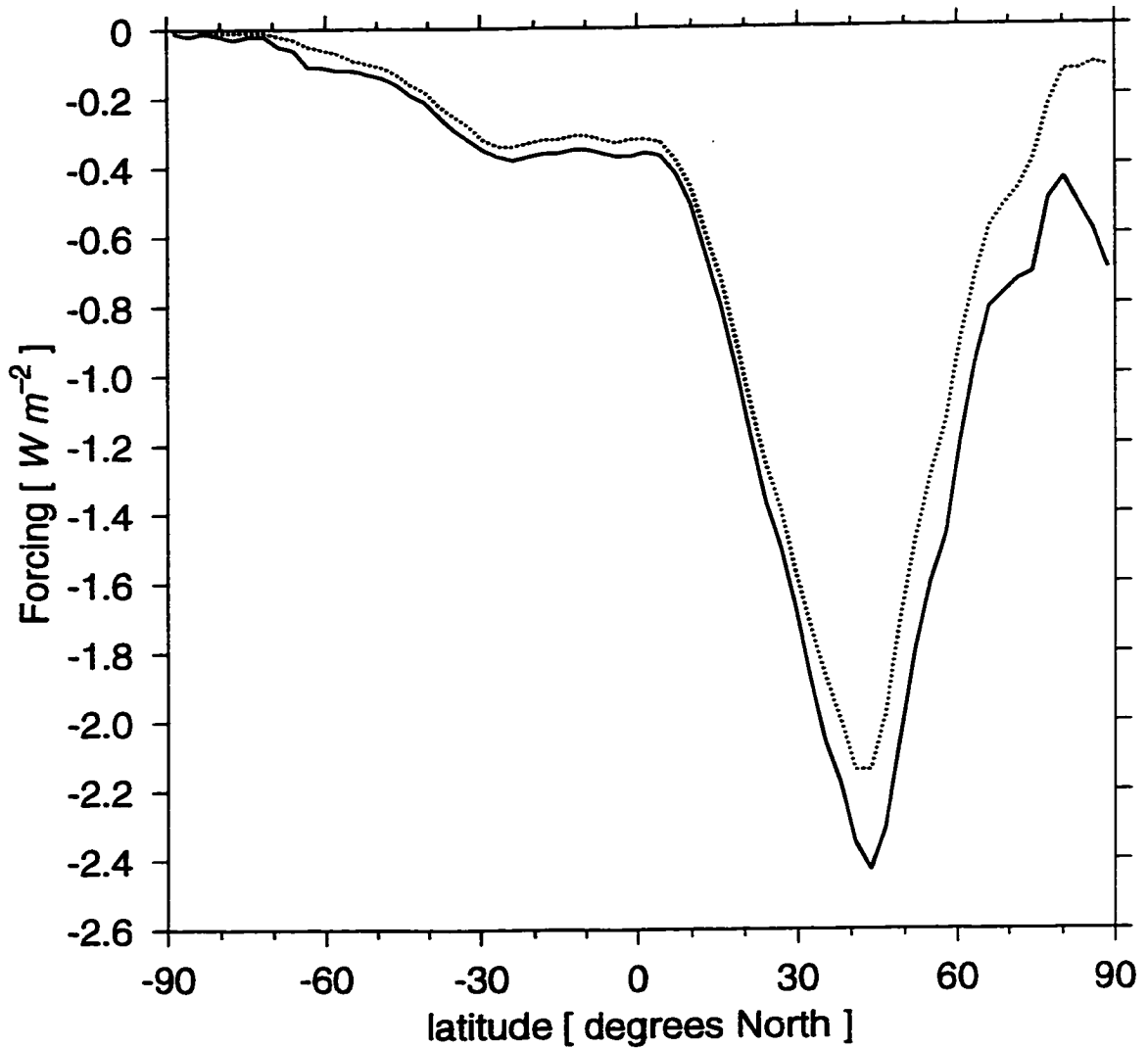
Figure 4.22: The annual average zonal sulfate aerosol forcing as a function of latitude. The dotted line corresponds to the forcing obtained using the original treatment of the optical properties (Kiehl and Briegleb 1993). Using the new relative humidity dependent optical properties results in the curve drawn with the solid line.

	northern hemisphere	southern hemisphere	global
new optical properties	-1.18	-0.20	-0.69
old optical properties	-0.96	-0.17	-0.56
Boucher and Anderson (1995)	-0.50	-0.12	-0.31
Chuang et al. (1997)	-0.71	-0.15	-0.43
Feichter et al. (1997)	-0.55	-0.13	-0.35
Haywood et al. (1997)	-0.66	-0.17	-0.41
Kiehl and Briegleb (1993)	-0.43	-0.13	-0.28
Taylor and Penner (1994)	-1.60	-0.30	-0.95

Table 4.3: Comparison of the average radiative forcing [$W\,m^{-2}$] of anthropogenic sulfate aerosols obtained by different research groups.

methods used to solve the radiative transfer equation 2.3. Schimel et al. (1996) suggest that the global annual average direct radiative forcing of sulfate aerosols to be $-0.4\,W\,m^{-2}$ with an uncertainty factor of 2.0. Current estimates of the indirect radiative forcing of sulfate aerosols is as high as $-4.8\,W\,m^{-2}$ (Lohmann and Feichter 1997).

Due to the spatial variability of the sulfate burden, the direct radiative forcing varies with location. Over highly polluted regions, the radiative forcing reaches as high as $-7\,W\,m^{-2}$. This is almost 3 times larger than the estimated radiative forcing of $2.45\,W\,m^{-2}$ due to the increase in greenhouse gas concentration since the beginning of the industrial age (Schimel et al. 1996), and it is almost 2 times the radiative forcing of $4\,W\,m^{-2}$ that is estimated to result if the carbon dioxide concentration in the atmosphere is doubled (Trenberth et al. 1996). This means that in highly polluted regions, the sulfate aerosol cooling effect dominates over the radiative forcing due to the increase in greenhouse gas concentrations since the industrial age and it may offset the effects of doubling CO_2 concentration.

Temperature measurements have been made for many decades at weather stations all over the world (Jones and Briffa 1992). These data sets provide information on the

trends in temperature changes that have taken place. Engardt and Rodhe (1993) compare the spatial pattern of anthropogenic sulfate aerosol burden with the geographical pattern of surface temperature changes. They find that the two patterns are consistent with model calculations that sulfate aerosols result in a cooling effect on climate. Hegerl and Cubasch (1996) statistically compare the observed temperature changes with predicted changes due to increases in greenhouse gas and aerosol concentrations. They find a 5% probability that the observed surface temperature increases over the past 30 years is due to natural variability. This means that the observed warming is caused by external influences such as changes in solar radiation, volcanic activity, and anthropogenic increases in greenhouse gas and aerosol concentrations. Hegerl et al. (1996) note that the correlation between observed and simulated patterns are better when the models include the effect of aerosols than when only carbon dioxide forcing alone is considered.

4.4 Summary

The radiative forcing of hygroscopic aerosols was shown to vary considerably with relative humidity due to the increase in size and by changing the refractive index. For ammonium sulfate aerosols, the radiative forcing increased by over a factor of four when the relative humidity was increased to 0.95. The radiative forcing varied considerably depending on the assumptions that were made. For example, when the relative humidity was between the crystallization and deliquescence points, the radiative forcing changed by a factor of approximately two when the aerosol was assumed to be in a wet state instead of a dry state. If the volume fraction mixing rule was not used to obtain an effective refractive index, a difference of a factor of two was seen between the extreme cases of using just the refractive index of water or of ammonium sulfate. A variation of approximately 30% was shown if the sulfate aerosol was assumed to be in the form of sulfuric acid or ammonium bisulfate instead of ammonium sulfate.

An overestimate in the radiative forcing due to ammonium sulfate aerosols of approximately 30% was shown if a constant van't Hoff factor is used in the Köhler equation. This illustrated the importance of using a concentration dependent van't Hoff factor to model aerosol growth. Using the Gerber parameterization resulted in a difference of only 1.5% making it accurate enough for radiation studies of $(NH_4)_2SO_4$ aerosols. Unfortunately, the coefficients used in the Gerber parameterization are not available for H_2SO_4 or NH_4HSO_4 aerosols. The Gerber parameterization applied to sea salt aerosols led to a difference in radiative forcing of over -30%. Therefore this parameterization should not be used for sea salt aerosols.

The global annual average direct radiative forcing due to sulfate aerosols was calculated with a radiation model that accounts for the spatial and temporal variations in sulfate burden and relative humdity. Use of relative humidity dependent optical properties led to a global annual average direct radiative forcing of anthropogenic sulfate aerosols of $-0.69\,W\,m^{-2}$ which was an increase of approximately 25% compared to previous studies using the same model. This value was small compared to the radiative forcing of $2.45\,W\,m^{-2}$ due to the increase in greenhouse gas concentrations since the beginning of the industrial age, and to radiative forcing of $4\,W\,m^{-2}$ that would have resulted if CO_2 concentration in the atmosphere was doubled. However, the direct radiative forcing of sulfate aerosol varied strongly with location and over highly polluted regions the radiative forcing dominated over greenhouse gas forcing. However the uncertainty in the radiative forcing of sulfate aerosols remained large when the global annual average forcing results obtained by other research teams was considered. Even if the optical properties of the sulfate aerosol was prescribed, a recent study found that the uncertainty in direct radiative forcing estimates are uncertain by approximately 20% due to differences in radiative transfer models (Boucher et al. 1998).

The radiative forcing of aerosols discussed in this chapter were for cloud free skies and aerosol mixtures were not considered. Boucher and Anderson (1995) estimated that the ratio of the direct radiative forcing of sulfate aerosols in cloudy skies to that

in clear skies is 0.25. In contrast, Haywood et al. (1997) found that the contribution of sulfate aerosol radiative forcing from cloudy skies was only 3%. The effect of strongly absorbing soot aerosols mixed with sulfate aerosols has been investigated by Haywood and Ramaswamy (1998) and Chýlek et al. (1995). Both found that the cooling effect of sulfate aerosols was reduced by the presence of soot. The radiative effect of organic and soil dust aerosols has not been considered since their hygroscopic nature and refractive index are uncertain.

Chapter 5

Cloud Radiative Forcing

5.1   Introduction

The absorption of solar radiation by the atmosphere, oceans, and land surfaces is a source of energy for atmospheric and oceanic processes. The total amount of solar radiation absorbed by the earth-atmosphere system can be deduced from satellite observations (Hartmann 1993; Harrison et al. 1990). The fraction of the total energy absorbed individually by the atmosphere, land surfaces, and oceans is less certain. The major source of uncertainty is due to clouds (Kiehl 1994; Wielicki et al. 1995). Clouds reflect a large fraction of solar radiation back to space making it unavailable for absorption by the atmosphere below the clouds, and by the surface. Clouds also absorb a portion of solar radiation themselves. The total effect of clouds can be an increase or a decrease of solar radiation absorbed by an atmospheric column.

From NASA Earth Radiation Budget Experiment (ERBE) satellite measurements, Hartmann (1993) found that the change in shortwave radiation absorbed by the atmospheric column due to the presence of clouds is $-48\,\mathrm{W\,m^{-2}}$ in an annual global average. When longwave radiation is included, the net cloud forcing is $-18\,\mathrm{W\,m^{-2}}$. The negative value of the net cloud forcing means that clouds have an overall cooling influence on the planet.

The cloud radiative forcing at a given level in the atmosphere is the change in the

net downward radiative flux at that level due to the presence of clouds. The ratio of the cloud radiative forcing at the surface to the cloud radiative forcing at the top of the atmosphere, denoted $\Re$, has been recently deduced from a set of satellite and surface measurements. Values of $\Re > 1$ imply that cloudy atmospheres absorb more radiation than clear atmospheres and $\Re < 1$ imply that cloudy atmospheres absorb less radiation than clear skies. By considering the energy budget measured on ships in the warm pool of the Pacific, located between 140°E to 170°E longitude and 10°N and 10°S latitude, Ramanathan et al. (1995) find that $\Re$ is approximately 1.5. Cess et al. (1995) analyze satellite and collocated surface measurements and found values of $\Re = 1.4$. Due to the different geographical locations that they considered, they conclude that this extra absorption does not vary much with location and season and that the absorption is not due to aerosols. From coordinated aircraft measurements above and below clouds, Pilewskie and Valero (1995) obtain a value of $\Re = 1.58$.

Li et al. (1997) compare the solar energy budget determined from four different global climate models (GCMs) and three satellite observational data sets. They find considerable variation in the amount of solar radiation that is reflected back to space and the amount that is absorbed individually by the atmosphere and surface. The cloud radiative forcing at the top of the atmosphere is between -45.9 and $-63.2\,\mathrm{W\,m^{-2}}$ which is consistent with Hartmann (1993)'s result. The cloud radiative forcing at the surface is between -44.5 and $-66.4\,\mathrm{W\,m^{-2}}$. The cloud radiative forcing ratio obtained lies in a range between 0.92 and 1.11.

The observed high values of $\Re \approx 1.5$ imply that more solar radiation is absorbed by cloudy atmospheres than expected because GCMs predict values of $\Re \approx 1.0$. This difference corresponds to approximately $25\,\mathrm{W\,m^{-2}}$ of excess absorption in a global annual average (Cess et al. 1996). This large difference has led to a strong debate concerning what the value of $\Re$ should be (Chou et al. 1995; Hayasaka et al. 1995; Li et al. 1995; Stephens 1996; Pilewskie and Valero 1996; Cess and Zhang 1996).

Kiehl et al. (1995) investigated the effect of increased cloud absorption in the GCM used by the National Center for Atmospheric Research (NCAR). They found

significant changes in atmospheric heating rates, atmospheric circulations, and surface wind speeds. Certain biases that are known to exist in their GCM are actually reduced when enhanced cloud absorption is introduced. However they warn that other GCMs may respond differently to enhanced cloud absorption.

In this chapter a simplified model is presented that allows an analytical solution depending on the radiative properties of the surface, the cloud layer, and the atmospheric layers above and below the cloud. An adding method and a plane parallel model are used to derive an analytical expression for the cloud radiative forcing ratio, $\mathfrak{R}$, as a function of various atmospheric parameters. The adding method (van de Hulst 1980; Goody and Yung 1989) is a suitable formulation of energy conservation for a plane parallel atmosphere. If the optical properties of individual atmospheric layers are known, energy conservation can be used to calculate the optical properties of the combined layers. For radiative fluxes the adding method is equivalent to solving the radiative transfer equation.

5.2   An Analytic Model

In the plane parallel atmospheric model, the atmosphere is homogeneous and infinite in its horizontal extent and its physical properties are allowed to change only in the vertical direction. To treat the problem of partial cloudiness, the radiative fluxes for clear and cloudy sky conditions are calculated separately and the radiative fluxes for partial cloudiness are obtained as an weighted average of the clear and cloudy sky cases.

Consider a three layer plane parallel atmosphere with clouds confined to the middle layer (see figure 5.1). Let the transmittance and the reflectance of the layer above the cloud be T_a and R_a, and the transmittance and reflectance of the layer below the cloud be T_b and R_b. Let the transmittance, reflectance, and absorptance of the cloud layer be denoted by T_c, R_c, and A_c. Let us further assume that the transmittance,

F_0 R_a

T_a T_a'' T_a' T_a'

T_b T_b'

Surface Albedo, a
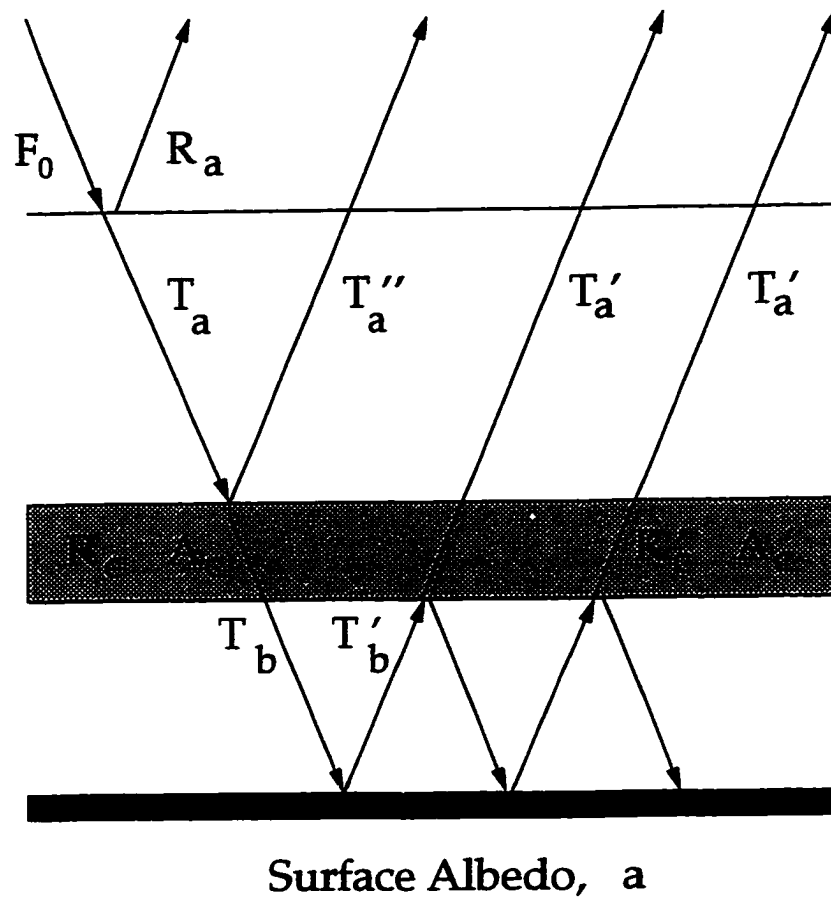
Figure 5.1: The plane parallel cloudy atmosphere model. T, R, and A stand for the transmittance, reflectance, and absorptance of individual layers. The subscripts a, b, and c refer to the atmospheric layer above, below, and containing the clouds. The primed symbols refer to the radiation reflected by the ground and the double primed symbols refer to the radiation that does not reach the surface and is reflected by clouds. The surface albedo is a.

reflectance, and absorptance functions of these layers are known. For a given atmospheric composition, the vertical position of the cloud layer within the atmosphere determines T_a and T_b. Each of the T_a, T_b, T_c, R_a, R_b, R_c, and A_c is a function of the solar zenith angle and includes direct and diffuse components. The surface albedo is denoted by a, and F_0 is the incident solar flux. All of the above defined quantities are functions of wavelength. The corresponding broadband quantities can be obtained by appropriate averages using the spectrum of incoming solar flux as a weighting function.

The broad band transmittance and reflectance differ from each other due to the different composition of the appropriate atmospheric layers, and to the different spectral distribution of the solar radiation entering the layer. Therefore, the transmittance through the same layer will be different for each multiple path of radiation through the layer. In the first approximation, the first path through the layer can be described by the T_a, T_b, T_c, R_a, R_b, and R_c as specified above. The upper layer transmittance for radiation that does not reach the surface and is reflected by the cloud layer is denoted by T_a''. The transmittance and reflectance for radiation that is reflected at least once by the surface are denoted by primed symbols T_a', T_b', T_c', R_a', R_b', and R_c'.

With the above notation the downward solar flux, F_{-S}^{cld}, at the surface with the presence of a cloud layer, can be written as

$$
\begin{aligned}
F_{-S}^{cld} &= F_0 T_a T_c T_b + F_0 T_a T_c T_b a T_b' R_c' T_b' + F_0 T_a T_c T_b a T_b' R_c' T_b' a T_b' R_c' T_b' + \cdots \\
&= F_0 T_a T_b T_c [\, 1 + a R_c' T_b'^2 + (a R_c' T_b'^2)^2 + \cdots] \\
&= F_0 T_a T_b T_c \lim_{N \to \infty} \frac{1 - (a R_c' T_b'^2)^N}{1 - (a R_c' T_b'^2)} \\
&= \frac{F_0 T_a T_b T_c}{1 - a R_c' T_b'^2}
\end{aligned}
\tag{5.1}
$$

since a, R_c', and T_b' are all less than one.

Similar expressions can be obtained for the upward flux at the surface, F_{+S}^{cld}, and the downward and upward fluxes at the top of the atmosphere, F_{-T}^{cld} and F_{+T}^{cld},

$$
F_{+S}^{cld} = \frac{a F_0 T_a T_b T_c}{1 - a R_c' T_b'^2}
\tag{5.2}
$$

$$F^{cld}_{-T} = F_0 \tag{5.3}$$

$$F^{cld}_{+T} = F_0 R_a + F_0 R_c T_a T''_a + \frac{a F_0 T_a T_b T_c T'_a T'_b T'_c}{1 - a R'_c T'^2_b} \tag{5.4}$$

where the minus and plus symbols stand for the downward and upward directions and the S and T subscript denote the surface and the top of the atmosphere, respectively. In the derivation of these expressions multiple reflections between individual layers are neglected with the exception of the multiple reflections between the surface and cloud layer. The terms that are not included in the summations are all proportional to the reflectance of the atmospheric layers above and below the cloudy layer which are both small.

For the clear sky case illustrated in figure 5.2, t and r denote the clear sky transmittance and reflectance for the incoming solar radiation. The upward transmittance of radiation reflected by the surface is denoted by t'. The multiple reflections by the surface and the clear atmosphere are neglected. The surface and the top of the atmosphere fluxes under the clear sky conditions are now given by

$$F^{clr}_{-S} = F_0 t \tag{5.5}$$

$$F^{clr}_{+S} = a F_0 t \tag{5.6}$$

$$F^{clr}_{-T} = F_0 \tag{5.7}$$

$$F^{clr}_{+T} = F_0 r + a F_0 t t' \tag{5.8}$$

To evaluate the broad band clear sky atmospheric transmittance a model described by Brine and Iqbal (1983) that includes Rayleigh scattering, water vapor, ozone, and carbon dioxide absorption is used with an atmospheric profile close to the midlatitude summer atmosphere. The solar spectrum is divided into 14 spectral bands (Winter and Chýlek 1997) and the transmittance is calculated within each band separately.
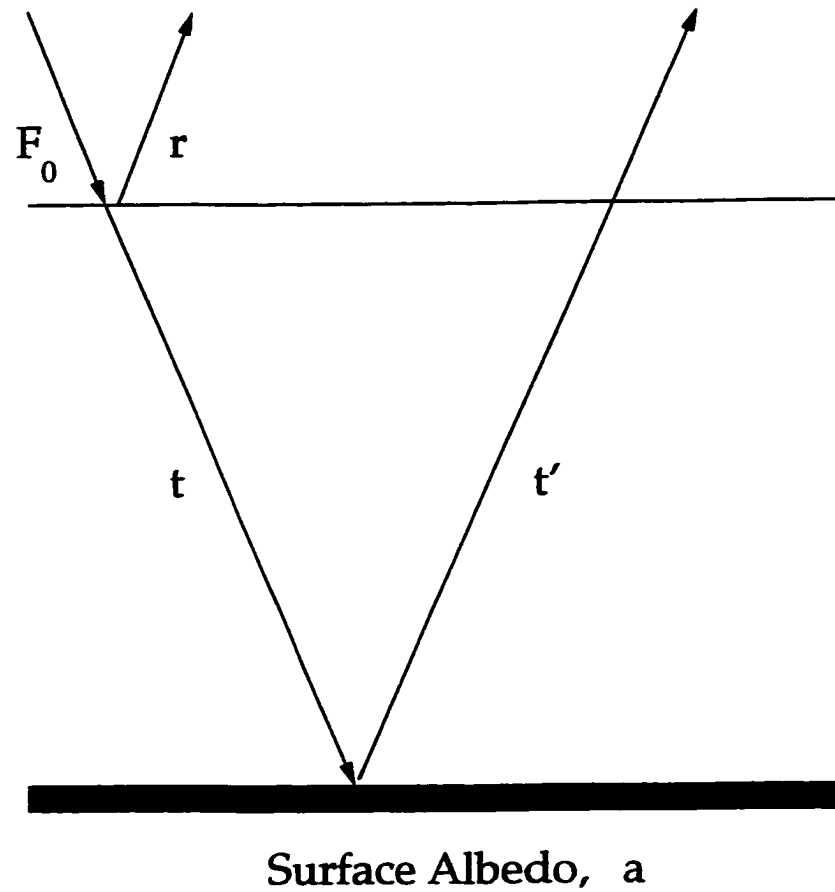
Figure 5.2: The plane parallel clear atmosphere. t and r stand for the transmittance and reflectance of the atmospheric layer. t' is the transmittance of radiation that is reflected by the ground. The surface albedo is a.

The total broad band transmittance is obtained by averaging spectral band transmittance using the incoming solar flux within each band as a weighting function. For the clear atmosphere the downward transmittance at zero solar zenith angle is $t = 0.78$ For the upward transmittance $t' = 0.90$ is obtained, assuming that the water vapor absorption bands are saturated after the first pass.

The cloud radiative forcing is defined as $CRF = F^{all} - F^{clr}$ where F denotes the net downward flux ($F = F_- - F_+$). The average all sky radiative fluxes are approximated, in the plane parallel atmosphere, by an average of the cloudy and clear sky fluxes: $F^{all} = NF^{cld} + (1 - N)F^{clr}$ where N is fractional cloud cover. The surface cloud radiative forcing, CRF_S, is obtained using equations 5.1 to 5.4

$$
\begin{aligned}
CRF_S &= F_S^{all} - F_S^{clr} \\
&= [NF_S^{cld} + (1 - N)F_S^{clr}] - F_S^{clr} \\
&= N[F_S^{cld} - F_S^{clr}] \\
&= N[(F_{-S}^{cld} - F_{+S}^{cld}) - (F_{-S}^{clr} - F_{+S}^{clr})] \\
&= N\left\{ \left[\left(\frac{F_0 T_a T_b T_c}{1 - aR_c' T_b'^2}\right) - \left(\frac{aF_0 T_a T_b T_c}{1 - aR_c' T_b'^2}\right) \right] - \left[(F_0 t) - (aF_0 t) \right] \right\} \\
&= F_0 N (1 - a)\left(\frac{T_a T_b T_c}{1 - aR_c' T_b'^2} - t \right)
\end{aligned}
$$

(5.9)

Similarly the top of the atmosphere cloud radiative forcing, CRF_T, is

$$
CRF_T = F_0 N \left(r - R_a + att' - R_c T_a T_a'' - \frac{aT_a T_b T_c T_a' T_b' T_c'}{1 - aR_c' T_b'^2} \right)
$$

(5.10)

The cloud radiative forcing ratio is defined by (Cess et al. 1995; Ramanathan et al. 1995; Li and Moreau 1996)

$$
\Re = \frac{CRF_S}{CRF_T}
$$

(5.11)

The significance of this ratio can be seen when the cloud radiative forcing on the atmospheric column, CRF_A, is considered

$$
CRF_A = N(A^{cld} - A^{clr})
$$

(5.12)

where the absorption of the cloudy and clear atmospheric column are denoted by A^{cld} and A^{clr} respectively. This quantity can be expressed in terms of $\Re$.

$$
\begin{aligned}
CRF_A &= N[(F_T^{cld} - F_S^{cld}) - (F_T^{clr} - F_S^{clr})] \\
&= N(F_T^{cld} - F_T^{clr}) - N(F_S^{cld} - F_S^{clr}) \\
&= CRF_T - CRF_S \\
&= CRF_T - (\Re \times CRF_T) \\
&= (1 - \Re) \times CRF_T
\end{aligned}
\tag{5.13}
$$

Comparing equations 5.12 and 5.13 it can be seen that the ratio, $\Re$, characterizes the change in the amount of solar radiation absorbed by a clear sky and cloudy atmospheric column. Harrison et al. (1990) found that $CRF_T < 0$ based on their analysis of satellite measurements. This means that if $\Re > 1$ then a cloudy atmospheric column absorbs more solar radiation than the corresponding clear sky column. If $\Re < 1$, then the cloudy atmospheric column absorbs less radiation.

Using equations 5.9 and 5.10 and multiplying the numerator and denominator by $1 - aR_c'T_b'^2$, $\Re$ can be written as

$$
\Re = \frac{(1 - a)[T_a T_b T_c - t(1 - aR_c'T_b'^2)]}{(1 - aR_c'T_b'^2)(att' + r - R_a - R_c T_a T_a'') - aT_a T_b T_c T_a'T_b'T_c'}
\tag{5.14}
$$

From the form of equation 5.14 it is apparent that the cloud radiative forcing ratio $\Re$ is independent of the amount of cloudiness, N. This is a direct consequence of how partial cloudiness is treated in the plane parallel atmosphere model. Numerical results obtained from detailed radiative transfer models (Li and Moreau 1996) are in agreement with this conclusion.

The dependence of $\Re$ on the solar zenith angle, cloud microphysics, cloud top and base heights, surface albedo and other parameters is implicit within the various symbols used in equations 5.9–5.10.

For small values of surface albedo the cloud radiative forcing ratio can be approximated, using the binomial expansion of the denominator, by

$$
\Re^{Lalb} = \left[\frac{T_b}{T_a''}\left(1 + \frac{A_c}{R_c}\right) - \frac{T_a T_b - t}{R_c T_a T_a''} \right]\left(1 + \frac{r - R_a}{R_c T_a T_a''} + ad\right)
\tag{5.15}
$$

where ad represents a small correction term with

$$d = \frac{tt'}{R_c T_a T_a''} - \frac{T_b T_b' T_c T_c'}{R_c} - 1 - \frac{R_c' T_b'^2 T_a T_b T_c}{t - T_a T_b T_c} \tag{5.16}$$

The terms proportional to $(T_a T_b - t)$, $(r - R_a)$, and the ad term in equation 5.15 are all small compared to one (for clouds that are not geometrically too thick). Consequently, the cloud radiative forcing ratio can be, in the first approximation, written as

$$\Re^{approx} = \frac{T_b}{T_a''}\left(1 + \frac{A_c}{R_c}\right) \tag{5.17}$$

Equation 5.17 is a crude approximation which reduces the physics of the problem into a simple transparent form. In the first approximation, the cloud radiative forcing ratio depends on the *ratio* of cloud absorptance to cloud reflectance — not just on cloud absorptance. It also depends on the ratio of the broad band atmospheric transmittance below the cloud layer to that of the above the cloud layer. The first factor, T_b/T_a'', depends on a location of the cloud in the atmosphere, on the distribution of gases and aerosols in the atmosphere and on the solar zenith angle. The second factor, $1 + A_c/R_c$, depends on cloud microphysics, geometrical parameters of a cloud and on the solar zenith angle.

5.3 Thick clouds

First consider the case of a thick cloud. Assume that most of the atmospheric mass is within the cloud layer. Consequently the atmospheric layer above the cloud is assumed to be completely transparent to incoming solar radiation and $T_a \approx T_a' \approx T_a'' \approx 1$. Most of the absorption due to water vapor and carbon dioxide as well as most of the Rayleigh molecular scattering takes place within the cloudy layer. Consequently, the atmospheric layer below the cloud will have a transmittance also close to one, leading to the approximation $T_b \approx T_b' \approx 1$. It is also assumed that all of the absorption by the cloudy layer occurs during the first pass through that layer so that $A_c' = 0.0$ and

layer	parameter	thick clouds	low clouds
clear	t	0.78	0.78
sky	r	0.06	0.06
	t'	0.90	0.90
upper	T_a	1.0	varied
	R_a	0.0	0.06
	T_a'	1.0	varied
	T_a''	1.0	varied
lower	T_b	1.0	1.0
	T_b'	1.0	1.0

Table 5.1: Atmospheric parameters used in the analytic expression of the cloud radiative forcing ratio for the thick and low cloud cases.

$R_c' = 0.50$ is assumed. Finally, the reflectance of the atmospheric layer above the cloud will be small and the approximation $R_a \approx 0$ is used. Thus, for a thick cloud $\Re$ is approximated by

$$\Re^{thick} = \left(1 + \frac{A_c}{R_c} - \frac{1-t}{R_c}\right)\left(1 + \frac{r}{R_c} + ad\right) \tag{5.18}$$

To calculate the range of possible numerical values for cloud radiative forcing ratio, $\Re$, we consider the cloud layer reflectance in the range from 0.4 to 0.8 and the cloud layer absorptance in the range from zero to 0.4. The clear atmosphere downward transmittance, t, for the incoming solar radiation is taken to be $t = 0.78$ and the clear atmosphere reflectance $r = 0.06$ (Lenoble 1993).

Table 5.1 summarizes the assumed values for various atmospheric parameters for the thick cloud situation. Values for the low cloud situation, which will be discussed in the following section, are also listed.

Numerical results are displayed in figure 5.3 for three values of surface albedo ($a = 0.0$, 0.15, and 0.50). In general, the cloud radiative forcing ratio, $\Re$, shows a strong dependence on the cloud layer absorptance and only weak dependence on the cloud layer reflectance. For the range of cloud layer absorptance between 0.10 and 0.16, $\Re$ is between 0.8 and 1.0.
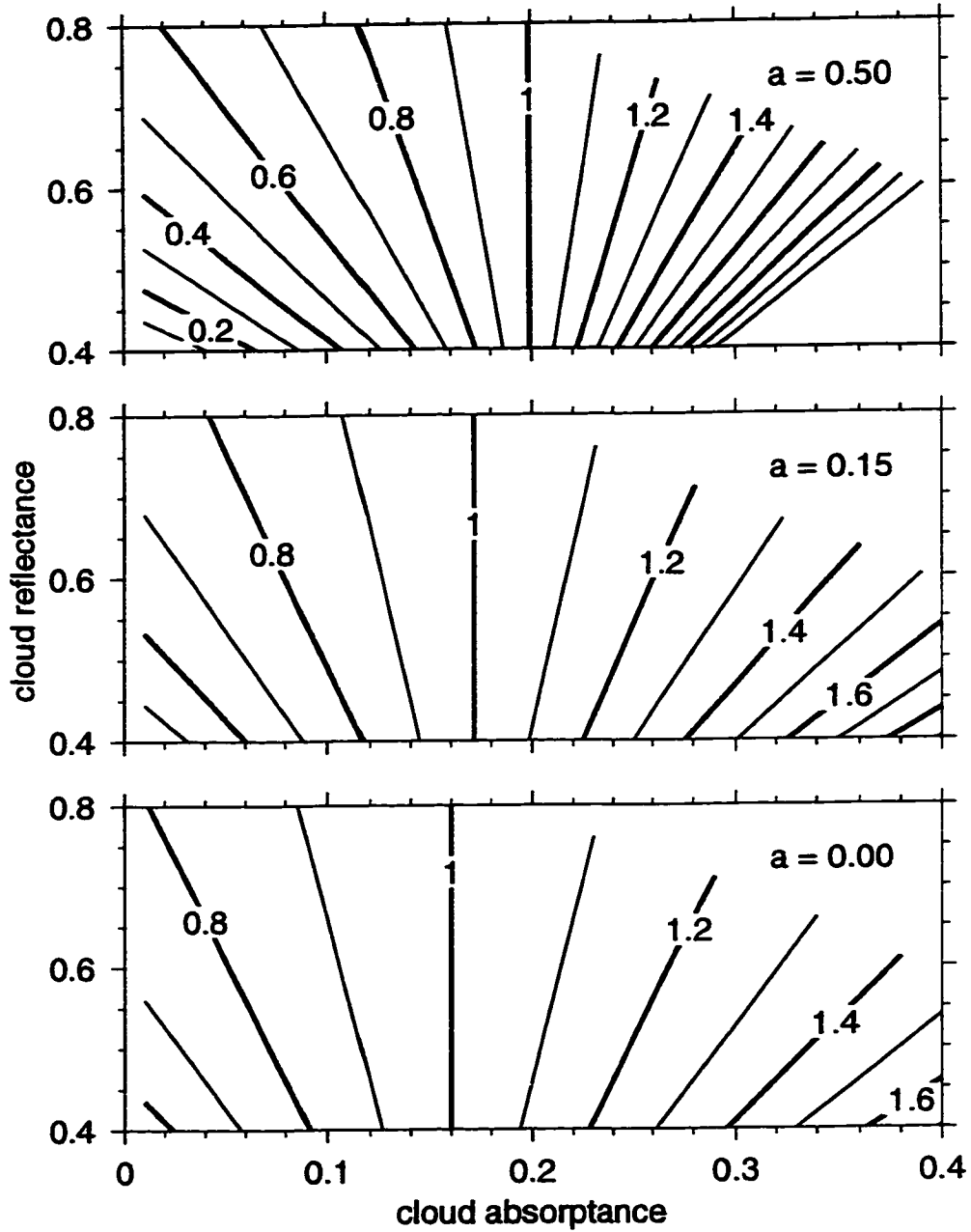
Figure 5.3: The cloud radiative forcing ratio, $\Re$, for a geometrically thick cloud and zero solar zenith angle, as a function of cloud layer absorptance and reflectance for surface albedos of 0.50 (top panel), 0.15 (middle panel), and zero (bottom panel). Only contours with $\Re \leq 2$ are plotted.

Changes in the value of $\Re$ due to small nonzero surface albedo are relatively small, as expected from equations 5.15 and 5.17. The functional dependence of $\Re$ on surface albedo is shown in figure 5.4 for clouds with $R_c = 0.50$ and $A_c = 0.10, 0.20,$ and 0.30. The relative difference between $\Re$ obtained by equation 5.14 and by the approximate equation 5.18 is within 10% for surface albedos less than approximately 0.30 (shown in figure 5.5).

To obtain values around 1.5 (as deduced from observational data analysis for the southern Pacific by Ramanathan et al. (1995)), cloud layer absorptance above 0.30 is needed. The maximum value of a thick cloud layer absorptance obtained in plane parallel atmosphere models is around 0.20. To increase this value to 0.30 requires some unaccounted for mechanism, like finite inhomogeneous cloud effects (Lubin et al. 1996), the presence of large drops, black carbon, or water vapor clusters (Chýlek and Geldart 1997).

5.4 Low clouds

The height of the cloud top determines the transmittance of the atmospheric layer above the cloud. The exact value of T_a, T_a', and T_a'' depends on atmospheric composition. For a low cloud, the transmittance of the atmospheric layer below the cloud can be taken as $T_b \approx 1$. The reflectance of the atmospheric layer above the cloud is approximated by the reflectance of the clear sky atmosphere $R_a \approx r$. In this case the cloud radiative forcing ratio is simplified as

$$\Re^{Ldd} = \frac{1}{T_a''}\left(1 + \frac{A_c}{R_c} - \frac{T_a - t}{R_c T_a T_a''}\right)(1 + ad) \tag{5.19}$$

Figure 5.6 plots contours of $\Re$ as a function of cloud reflectance and absorptance for low clouds with the upper atmospheric layer transmittance of $T_a \approx T_a' \approx T_a'' \approx 1.0$. In comparison to the thick cloud situation shown in figure 5.3, corresponding contours of $\Re$ are shifted more to the left in the figure. This means that higher values of $\Re$ are obtained with lower cloudy layer absorptances in the low cloud case.
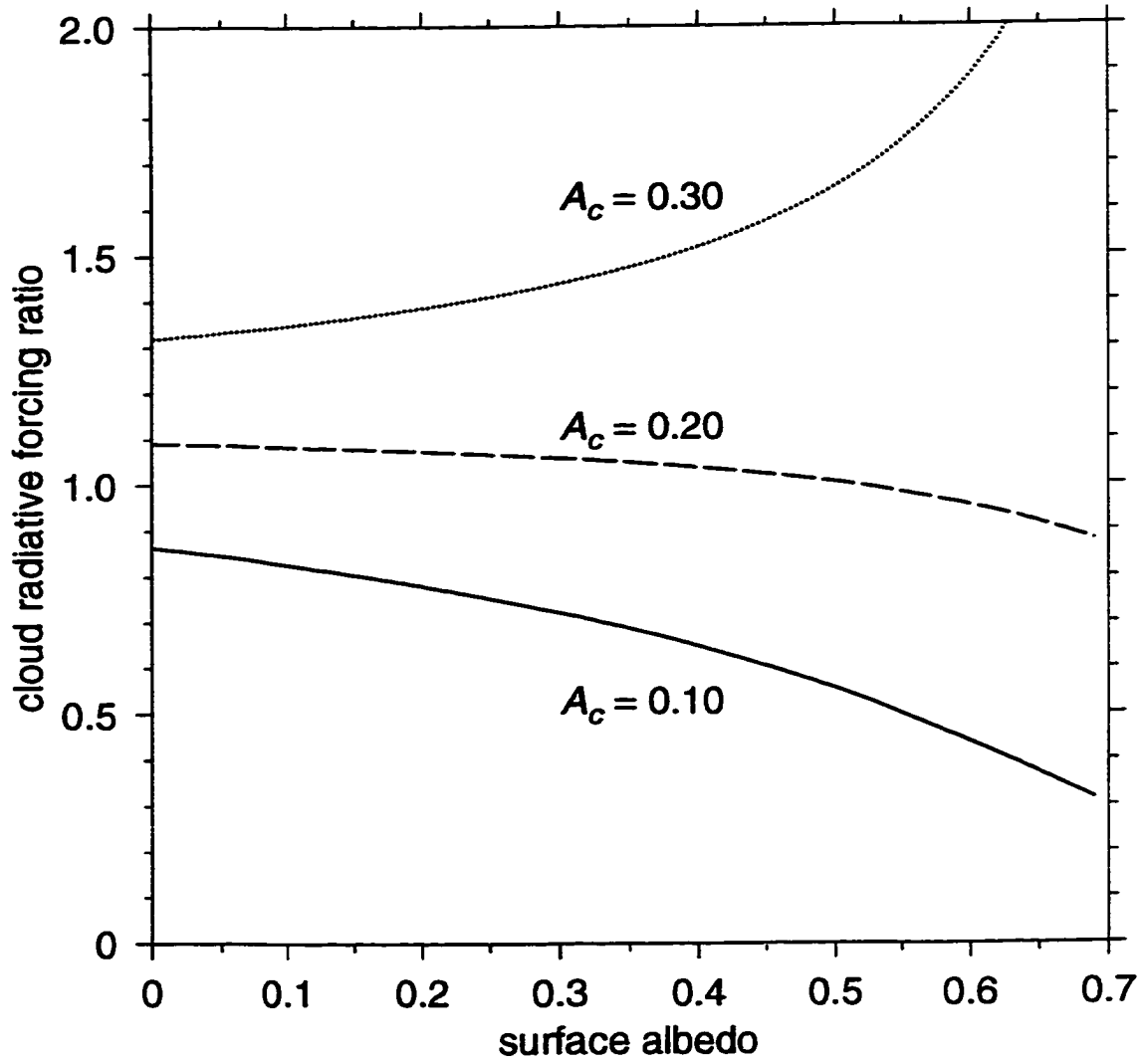
Figure 5.4: The cloud radiative forcing ratio, $\Re$, for a thick cloud as a function of surface albedo with $R_c = 0.50$ and $A_c = 0.10$ (solid line), 0.20 (dashed line), and 0.30 (dotted line).
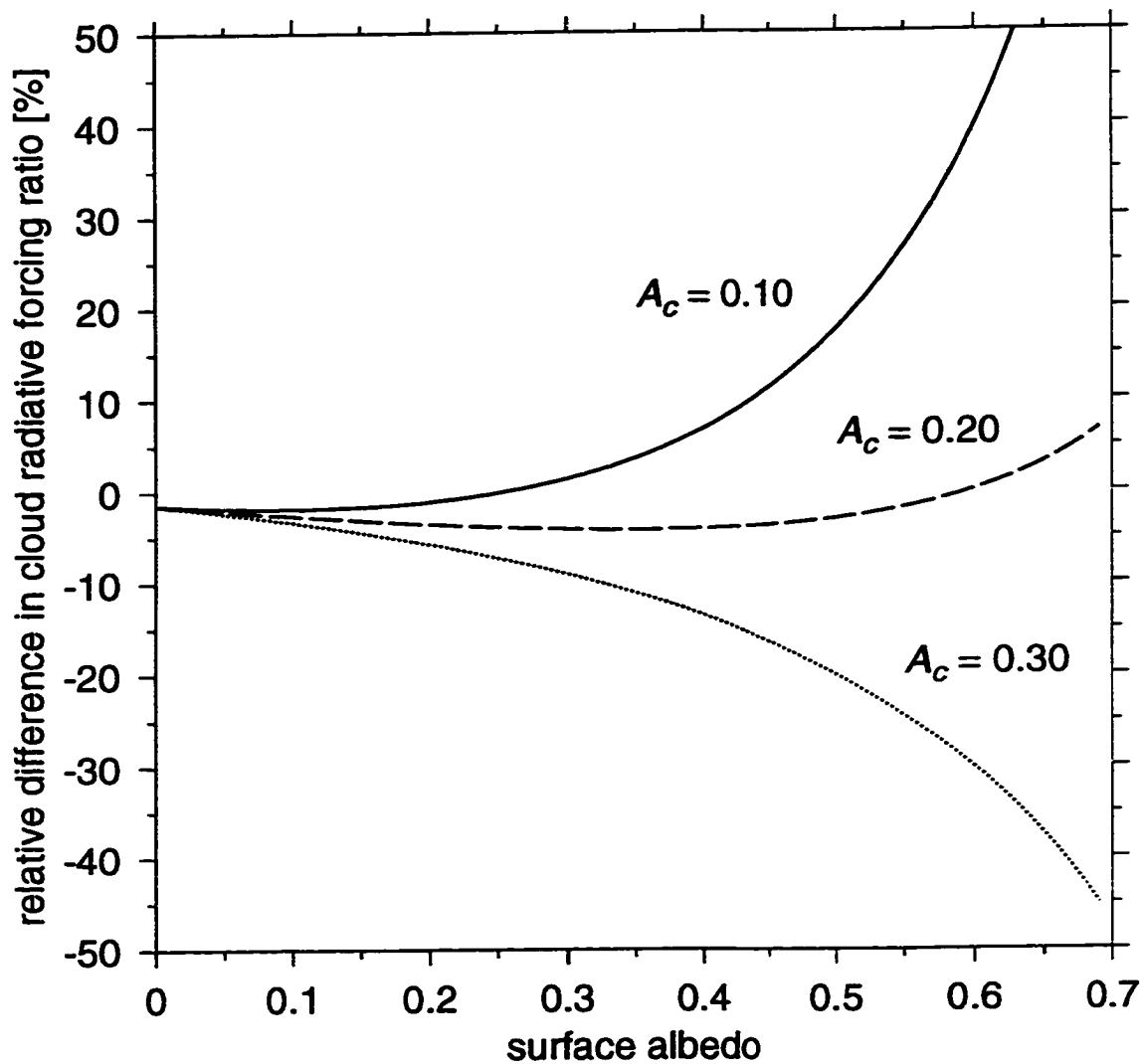
Figure 5.5: The relative difference in cloud radiative forcing ratio, $\mathfrak{R}$, calculated by equation 5.14 and 5.18 for a thick cloud as a function of surface albedo with $R_c = 0.50$ and $A_c = 0.10$ (solid line), 0.20 (dashed line), and 0.30 (dotted line).
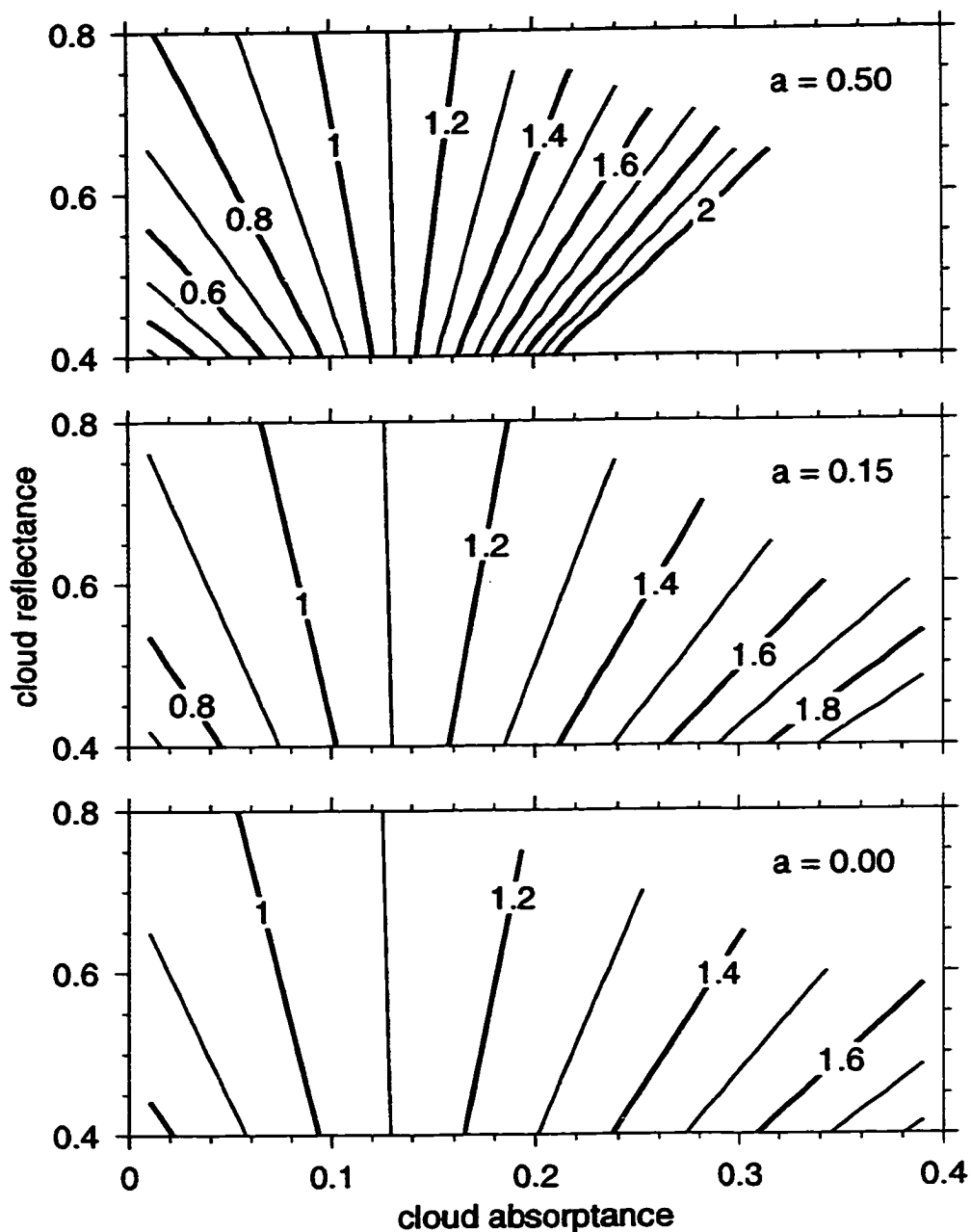
Figure 5.6: The cloud radiative forcing ratio, $\mathfrak{R}$, for a low cloud and zero solar zenith angle, as a function of cloud layer absorptance and reflectance for surface albedos of 0.50 (top panel), 0.15 (middle panel), and zero (bottom panel). The upper atmospheric layer transmittance is taken as $T_a \approx T_a' \approx T_a'' \approx 1$. Only contours with $\mathfrak{R} \leq 2$ are plotted.

Values of $\Re$ are shown in figure 5.7 as a function of the above the cloud layer transmittance of T_a for cloudy layers with $R_c = 0.50$ and $A_c = 0.10$, 0.20, and 0.30 above a zero surface albedo. There is an inverse relationship between $\Re$ and T_a. This means that $\Re \approx 1.5$ can be obtained by decreasing the transmittance of the atmospheric layer above the cloudy layer as well as by increasing the absorptance of the cloudy layer.

The low level cloud with the above the cloud layer atmospheric transmittance $T_a = 0.9$ and a cloud layer absorptance between 0.10 and 0.20 leads to values of $\Re$ between 0.9 and 1.2. On the other hand, if the atmospheric transmittance above the cloudy layer is reduced to $T_a = 0.80$, the $\Re$ increases to values between 1.5 and 1.7.

If smoke from tropical biosphere burning gets into and above the low level cloud layer, it will increase the cloud layer absorptance and at the same time decrease the transmittance, T_a, of the above the cloud layer. Both of these effects will cause $\Re$ to increase. Smoke above the cloud layer cannot be easily removed by washout and may stay in the atmosphere for some time. Thus tropical region biosphere burning may contribute significantly to the increase of $\Re$ for low level clouds.

5.5 Comparisons to a Radiation Model

5.5.1 Values of $\Re$

To examine the accuracy of the analytical model, consider the case when the surface albedo is zero. Equation 5.14 reduces to

$$\Re(a = 0) = \frac{T_a T_b T_c - t}{r - R_a - R_c T_a T_a''} \tag{5.20}$$

which reduces further to

$$\Re(a = 0) \approx -\frac{T_a T_b T_c - t}{R_c T_a^2} \tag{5.21}$$

if it is assumed that $r - R_a \approx 0$ and $T_a \approx T_a''$.

Figure 5.7: The cloud radiative forcing ratio, $\mathfrak{R}$, for a low cloud over a zero surface albedo as a function of transmittance of the layer above the cloud. The cloud reflectance is $R_c = 0.50$ and the cloud absorptance $A_c = 0.10$ (solid line), 0.20 (dashed line) and 0.30 (dotted line).
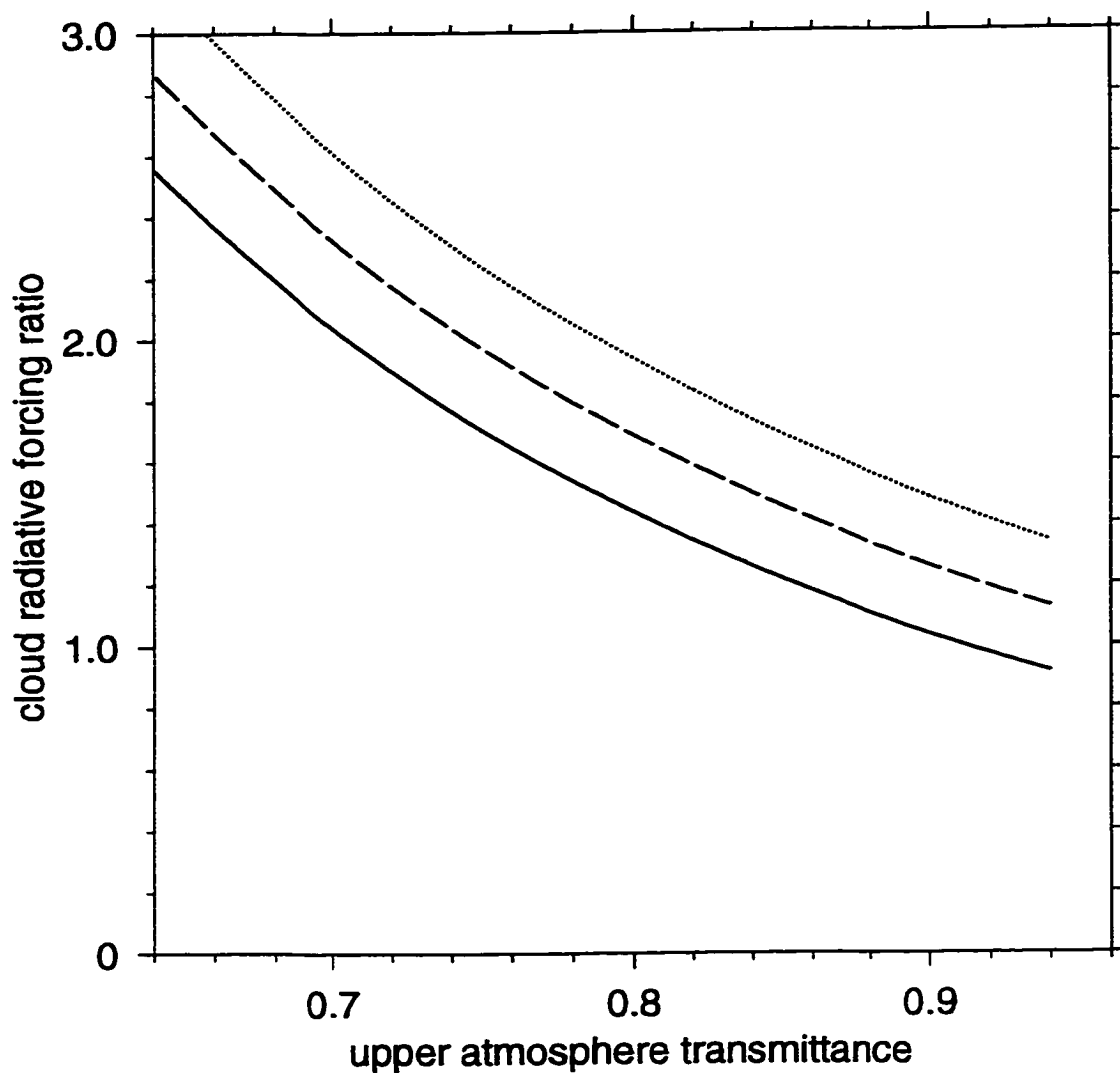
layer	downward flux [$\mathrm{W\,m^{-2}}$]	upward flux [$\mathrm{W\,m^{-2}}$]
top of the atmosphere	314.5	249.3
just above cloud	286.3	255.0
just below cloud	31.7	0.54
surface	31.1	0.0

Table 5.2: Radiative flux profile in a mid-latitude summer atmosphere with a 1 km thick stratus cloud layer with $r_{eff} = 5.89\,\mu\mathrm{m}$ and $LWC = 0.22\,\mathrm{g\,m^{-3}}$ obtained with the Fu-Liou radiation model. The cloud base is at a height of 1 km, the surface albedo is zero, and the solar zenith angle is 60°.

The Fu-Liou radiation model, described in chapter 4, is used to obtain the total upward and downward radiative fluxes at the top of the atmosphere, at the surface, and above and below a cloudy layer in a mid-latitude summer atmosphere. From these fluxes, $\Re$ can be obtained and values for all the parameters in equation 5.20 can be approximated. The solar zenith angle is set to 60° and only the spectral band between 0.20 to 0.69 $\mu\mathrm{m}$ is considered.

For the clear atmosphere, the downward flux at the top of the atmosphere is 314.5 $\mathrm{W\,m^{-2}}$ and at the surface it is 245.2 $\mathrm{W\,m^{-2}}$. The upward flux at the top of the atmosphere is 43.7 $\mathrm{W\,m^{-2}}$. This means that the clear atmosphere transmittance and reflectance are approximately $t = 0.78$ and $r = 0.14$.

The case of a low level cloud is considered. To obtain the reflectance and transmittance of a cloudy layer, a stratus cloud approximately 1 km thick is placed immediately above a zero surface albedo. The effective radius of the cloud droplets is $r_{eff} = 5.89\,\mu\mathrm{m}$ and the liquid water content is set to $LWC = 0.22\,\mathrm{g\,m^{-3}}$ (Stephens 1978). The downward fluxes just above and just below the cloud are 285.3 and 31.0 $\mathrm{W\,m^{-2}}$ respectively. This leads to a transmittance of 0.109. The upward flux just above the cloud is 254.2 $\mathrm{W\,m^{-2}}$ so that the cloud reflectance is 0.891.

The cloud is then moved to the atmospheric layer between 1 and 2 km and the flux results are shown in table 5.2. These values suggests that the upper atmospheric layer's transmittance is 0.910 and the lower atmospheric layer's transmittance is 0.983.

layer	downward flux $[\text{W}\,\text{m}^{-2}]$	upward flux $[\text{W}\,\text{m}^{-2}]$
top of the atmosphere	314.5	277.9
just above cloud	292.3	288.6
just below cloud	1.3	0.02
surface	1.3	0.0

Table 5.3: Radiative flux profile in a mid-latitude summer atmosphere with a thick cloud layer with $r_{eff} = 31.23\,\mu\text{m}$ and $LWC = 2.5\,\text{g}\,\text{m}^{-3}$ obtained with the Fu-Liou radiation model. The cloud base is at a height of 1 km, the cloud top is at 10 km, the surface albedo is zero, and the solar zenith angle is $60°$.

Substituting the transmittances and reflectances into equation 5.21, the cloud radiative forcing ratio obtained is 0.92. If the flux results from the Fu-Liou model is used directly into equation 5.11, then $\Re = 1.04$. The relative difference between the two values is -11.3% with respect to the Fu-Liou model's results.

The same calculations are carried out for the case of thick clouds. The effective radius of the cloud drops is set to $31.2\,\mu\text{m}$ and the liquid water content to $2.5\,\text{g}\,\text{m}^{-3}$ (Stephens 1978). These cloud properties are kept constant from 1 km to 10 km. The flux profile is shown in table 5.3. From this radiative flux profile, the transmittance of the atmospheric layer above the cloud is $T_a \approx 0.93$ and below the cloud it is $T_b \approx 0.98$. The transmittance of the cloudy layer is only 0.0045 and the reflectance is 0.987. With these values the cloud radiative forcing ratio obtained from equation 5.21 is 0.91. Using the flux results in equation 5.11 leads to $\Re = 1.04$. The relative difference of the analytical model is -13%.

Based on these cases, the accuracy of the analytical model is estimated to be between 10% and 15%.

5.5.2 Effect of Absorbing Aerosols

From using the analytic model, it was seen that one possible mechanism by which the cloud radiative forcing ratio could be increased was by decreasing the transmittance of the atmospheric layer above a low level cloud. A lower transmittance can be caused

by introducing a layer of aerosols above the low level cloud.

The Fu-Liou model is now used to calculate the radiative fluxes in a mid-latitude summer atmospheric profile with the stratus cloud considered in the previous section. A layer of absorbing aerosols is placed in the layer just above the layer containing the stratus cloud. The optical properties of absorbing aerosols calculated in chapter 2 are used. The radiative forcing ratio for this situation is plotted in figure 5.8 as a function aerosol optical depth.

Four sets of data are shown in this figure. The effect of aerosols with a refractive index of $1.39 + i\, 0.0075$ is shown with the $\triangle$ and $\square$ symbols which corresponds to aerosols with effective radii of 0.06 and $1.02\,\mu\mathrm{m}$ respectively. Even for optical depths of 0.1 the radiative forcing ratio has only increased to approximately 1.1. Increasing the absorbing ability of the aerosol so that the refractive index of the particles is $1.75 + i\, 0.44$ corresponding to black carbon does result in high values of $\Re$. Figure 5.8 shows the forcing ratio for these aerosols with $\blacktriangle$ and $\blacksquare$ symbols corresponding to size distributions with $r_{eff} = 0.06$ and $1.02\,\mu\mathrm{m}$. However the optical depth of approximately 0.1 are required to obtain $\Re \approx 1.5$ which is higher than the estimated global mean optical depth of primary soot aerosols of 0.003 (Schimel et al. 1996). This suggests that high values of $\Re$ are possible with this mechanism only in highly polluted regions. Li (1998) also came to this conclusion. However, Cess et al. (1995) concluded that aerosols are not responsible for their high values of $\Re$ because they did not see strong spatial and temporal variation in their analyses that would correlate with high aerosol concentrations.

Another mechanism that would lead to higher values of $\Re$ is the incorporation of absorbing aerosols into the cloudy layer. Chýlek et al. (1996) calculated the optical properties of cloud droplets containing black carbon aerosols. They found that this mechanism could not account for the excess absorption of $25\,\mathrm{W\,m^2}$ that $\Re \approx 1.5$ implied.
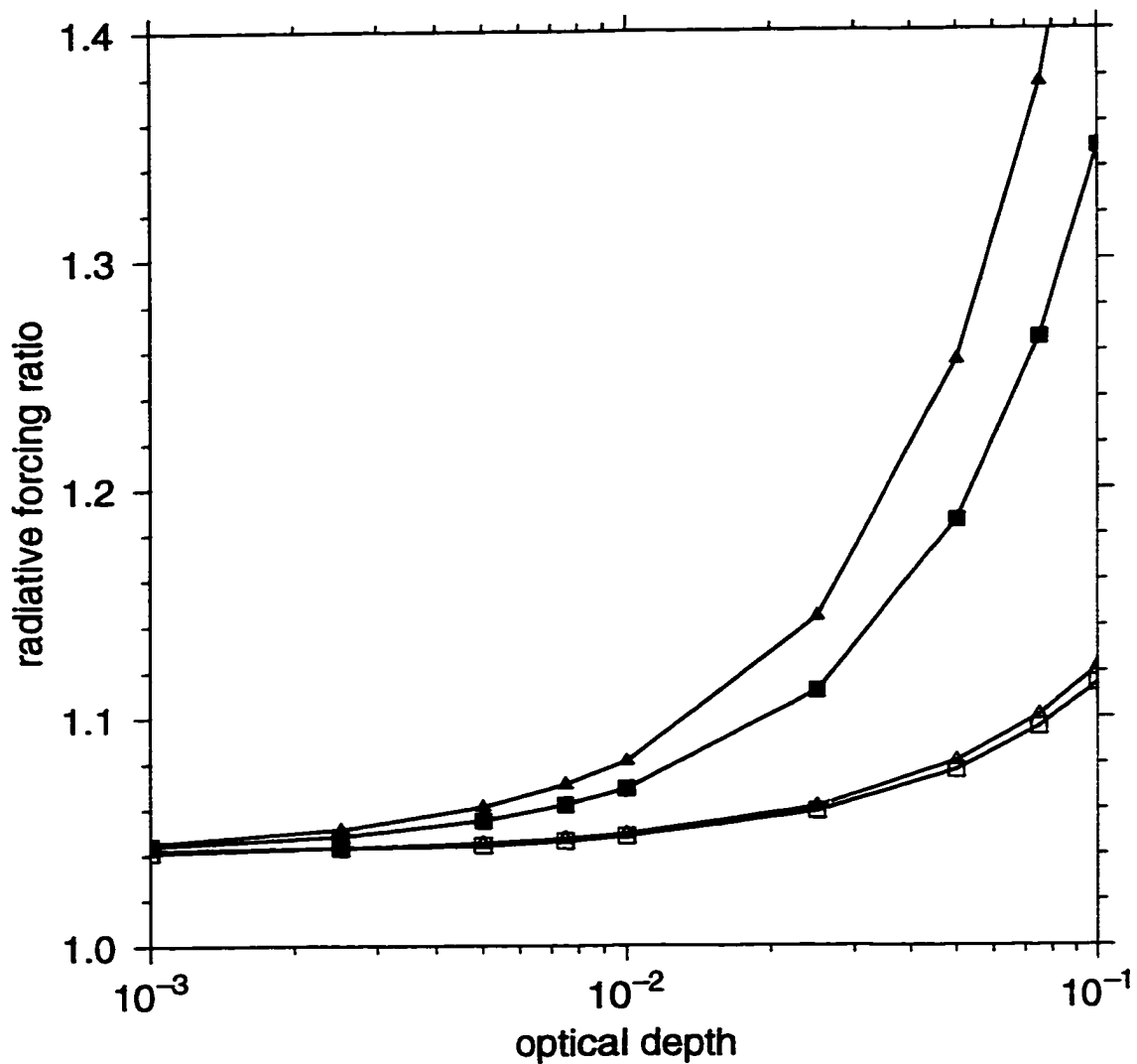
Figure 5.8: The radiative forcing ratio for a stratus cloud with a layer of absorbing aerosols above it as a function of aerosol optical depth. The cloud is situated between 1 to 2 km with $r_{eff} = 5.89\,\mu m$ and $LWC = 0.22\,\mathrm{g\,m^{-3}}$. The $\triangle$ and $\square$ correspond to aerosols with $r_{eff} = 0.06$ and $1.02\,\mu m$ respectively with a refractive index of $1.39 + i\,0.0075$. The $\blacktriangle$ and $\blacksquare$ corresponds to aerosols with $r_{eff} = 0.06$ and $1.02\,\mu m$ respectively with a refractive index of $1.75 + i\,0.44$.

5.6 Summary

By using a three layer plane parallel model atmosphere over a reflecting surface, analytical expressions (5.14 to 5.17) for the cloud radiative forcing ratio, $\Re$, are derived. The ratio $\Re$ has an especially simple form for the case of small surface albedo (equations 5.15 and 5.17). The advantage of these analytical expressions is their simplicity. Comparisons of $\Re$ obtained with the analytical model with values obtained from the Fu-Liou radiation model suggests that the accuracy of the analytical model is between 10% and 15%. Effects of cloud radiative properties, surface albedo, and atmospheric transmission can be separated and their individual effects on the ratio $\Re$ can be evaluated. Such sensitivity studies are more difficult to perform using radiative transfer models or with large satellite data sets. The results are similar to those obtained by Li and Moreau (1996).

Though the analytic expression of $\Re$ does not resolve the debate concerning the possibility of excess absorption, it is still a useful tool. By considering various cases of cloud situations, it was determined that values of $\Re \approx 1.5$ are obtainable with the presence of low level clouds if the transmittance of the atmospheric layer above the cloudy layer is reduced to $T_a \approx 0.8$. A mechanism that could do that is a layer of absorbing aerosols above the cloudy layer. By considering a low level stratus cloud with absorbing aerosols in a layer above the cloud, high values of $\Re \approx 1.5$ are obtained for strongly absorbing aerosols with refractive indices of $1.75 + i\,0.44$ in polluted regions where the optical depth of the strongly absorbing aerosol approaches 0.1.

Chapter 6

Conclusions

The purpose of this work was to study how tropospheric aerosols and clouds affect Earth's solar radiation budget. Two current atmospheric problems were considered: the direct radiative forcing due to tropospheric aerosols, and the enhanced shortwave radiation absorption by clouds.

The direct radiative effect of tropospheric aerosols was considered where the particles absorbed and scattered solar radiation back to space, resulting in an overall cooling influence on climate. Charlson et al. (1992) used a simple analytical expression to estimate the direct radiative effect of sulfate aerosols. The proper extension of Charlson et al. (1992)'s equation for absorbing aerosols was derived and used to study the sensitivity of the direct radiative forcing of absorbing smoke aerosols to size distribution and refractive index. The radiative forcing depended on the backscattering fraction of the aerosols. This quantity was strongly dependent on the effective radius of the aerosol size distribution. The dependence on the refractive index of the aerosol, within observed bounds, was weak in comparison. The direct radiative forcing of the aerosol ranged from approximately $-0.2\,\mathrm{W\,m^{-2}}$ for size distributions with effective radii greater than $0.4\,\mu\mathrm{m}$ to $-1.0\,\mathrm{W\,m^{-2}}$ when the effective radius was less than $0.1\,\mu\mathrm{m}$. Therefore estimates of the direct radiative forcing of smoke aerosols varied by a factor of 2.0 just from assumptions concerning the aerosol size distribution.

The direct radiative forcing of hygroscopic aerosols such as sulfate, nitrate, and

sea salt aerosols were considered. The optical properties and resulting radiative forcing of these aerosols varied with ambient relative humidity. This was due to the condensation of water onto the particles which resulted in increases in particle size and changes in the concentration of the chemical components that the particle consisted of. Before the optical properties of hygroscopic aerosols could be calculated, the equilibrium size of the particles had to be determined. This was described by the Köhler equation (Köhler 1936). Some of the parameters in the Köhler equation, such as the van't Hoff factor, depended on the concentration of the particles' chemical components. Because of this dependence modifications to the Köhler equation have been suggested by Young and Warren (1992) which was derived from considerations of a thermodynamic potential. But the equilibrium radius of an aerosol predicted by the modified Köhler equation was found to be in error when compared with measured observations of an ammonium sulfate aerosol by Tang and Munkelwitz (1994). Using the original Köhler equation with a concentration dependent van't Hoff parameter was in agreement with the measurements. The reason for this discrepancy was that the modified Köhler equation was thermodynamically inconsistent. A thermodynamically consistent treatment of the Gibbs free energy would have led to the original Köhler equation. To obtain the equilibrium radius of a hygroscopic aerosol given the ambient relative humidity was an iterative procedure using the Köhler equation. Because of the computing time involved with iterative procedures, parameterizations such as Gerber (1985)'s parameterization that expressed the relationship between size and relative humidity explicitly were useful. It was found that for ammonium sulfate aerosols, the error in using Gerber's parameterization was small compared to using the Köhler equation. However, the relative difference in the equilibrium radius of sea salt aerosols predicted by Gerber's parameterization was found to be greater than 30% which made it unsuitable for use in aerosol radiative forcing studies. Unfortunately, the coefficients used in the Gerber parameterization were not available for sulfuric acid and ammonium bisulfate aerosols.

The change in an aerosol size distribution with relative humidity was determined

by assuming that the number of particles was conserved, that there was no competition for the water vapor that was in the ambient environment, and there was enough time for each particle to grow to its equilibrium size described by the original Köhler equation. With the equilibrium aerosol size distribution determined, calculation of the extinction coefficient, single scattering albedo, and asymmetry parameter of the aerosols became possible. These three quantities were needed to estimate the radiative forcing due to the aerosols. For ammonium sulfate aerosols, the radiative forcing derived from using a constant van't Hoff factor was overestimated by 29% compared to using a concentration dependent van't Hoff factor when the relative humidity was 0.90. Using the Gerber parameterization to model aerosol growth resulted in a difference of only 1.5%. For sea salt aerosols, the radiative forcing derived from the use of a constant value of the van't Hoff factor was underestimated by more than 15% and the forcing derived from using the Gerber parameterization was underestimated by 25%. These errors indicated the importance of using the Köhler equation with a concentration dependent van't Hoff factor to obtain the equilibrium size of the aerosol. The change in the refractive index of the aerosol was treated by using an average refractive index that was weighted by the volume fraction of each component. A factor of 2.0 difference in the radiative forcing was found if the refractive index of pure water or highly concentrated ammonium sulfate solution was used instead of a volume weighted average. A factor of 2.0 decrease in radiative forcing of ammonium sulfate aerosol occurred at 0.80 relative humidity if the effective radius of the initial dry size distribution was changed from $0.17\,\mu m$ to $0.68\,\mu m$. There was a strong dependence of the radiative forcing of ammonium sulfate aerosols with relative humidity. The magnitude of the forcing increased by over a factor of 4.0 when the relative humidity was increased from 0.00 to 0.90. The forcing of ammonium sulfate aerosols was further complicated because its growth with relative humidity depended on its history. A factor of up to 2.0 difference resulted if the aerosol was considered to be in a wet state than if it was considered to be its dry state when the relative humidity was between the aerosol's crystallization and deliquescence point relative humidities. In

agreement with Boucher and Anderson (1995), the radiative forcing of sulfate aerosols was larger if the sulfate was in the chemical form of sulfuric acid instead of ammonium sulfate (see figure 4.12). Ammonium bisulfate aerosols resulted in the smallest radiative forcing. Nitric acid aerosols had the strongest normalized radiative forcing. Nevertheless the radiative forcing of these aerosols would have been weaker than that of sulfate aerosols because the global annual mean burden of nitrate aerosols has been estimated to be 5 times smaller than the sulfate burden (Pilinis et al. 1995).

The radiative effect of a thin layer of sulfate aerosol varied linearly with sulfate burden and surface albedo and there was a strong dependence on solar zenith angle. Due to the spatial and temporal variability of sulfate aerosol burden (Pham et al. 1995), the radiative forcing of the aerosol varied from location to location and varied during the course of a day. A radiation model that accounted for the spatial and temporal distribution of sulfate and the variation of relative humidity was used to obtain an estimate of the global annual mean direct radiative forcing of anthropogenic sulfate aerosol. Originally, this model did not properly treat the effects of hygroscopic growth on the optical properties of sulfate aerosols. With the new relative humidity dependent optical properties, the predicted radiative forcing increased by almost 25% to a global annual average value of $-0.69\,\mathrm{W\,m^{-2}}$. This value was between the high value predicted by Taylor and Penner (1994) of $-0.95\,\mathrm{W\,m^{-2}}$ and the low value of $-0.28\,\mathrm{W\,m^{-2}}$ of Kiehl and Briegleb (1993). Though these values may seem small, the direct radiative forcing of sulfate aerosol varied strongly with location. Over polluted regions the forcing was as high as $-7\,\mathrm{W\,m^{-2}}$. This was almost 3 times higher than the estimated radiative forcing due to the increase in greenhouse gas concentrations since the industrial age (Schimel et al. 1996). Furthermore, the indirect effect of sulfate aerosols has been suggested to be even larger than the direct effect (Schimel et al. 1996). The total radiative forcing of sulfate aerosols was not insignificant. Statistical comparisons by Hegerl et al. (1996) indicated that correlations between observed and modeled climate changes over the past 30 years were better when anthropogenic aerosol effects were included.

The results from these studies demonstrate the uncertainties associated with Earth's shortwave radiation budget due to aerosols. Kiehl and Trenberth (1997) estimated that a decrease in absorbed shortwave radiation by the planet of $3\,\mathrm{W\,m^{-2}}$ was due to all aerosols. The radiative effect of aerosols was shown to be dependent on the chemical composition of the aerosols and on their size distribution. For hygroscopic aerosols, the radiative effect depended on the ambient relative humidity. Due to the spatial and temporal variation of sulfate aerosols, the decrease in absorbed shortwave radiation over polluted regions was estimated to be a factor of 2.0 larger. Field measurement efforts such as the Tropospheric Aerosol Radiative Forcing Observational Experiment (TARFOX) and the Aerosol Characterization Experiment (ACE) should be continued in order to constrain the assumptions that are made concerning aerosol size distribution, aerosol chemical composition, and aerosol burden. Pan et al. (1997) indicated that the majority of the uncertainty of the radiative forcing of sulfate aerosols is associated with the uncertainties in the sulfate distribution. Aerosol mixtures were not considered in this work. Chýlek et al. (1995) and Haywood et al. (1997) demonstrated that the cooling effect of sulfate aerosols would be reduced by the presence of black carbon aerosols.

An analytic expression for the ratio of the cloud radiative forcing at the surface to the cloud radiative forcing at the top of the atmosphere, denoted by $\mathfrak{R}$, was derived using a simple plane-parallel atmospheric model. The advantage of this expression was that the effect of various atmospheric parameters on the cloud radiative forcing ratio could be seen from the equation. Sensitivity studies could be performed quickly and were in general agreement with most studies that were based on the analysis of large data sets from satellite measurements or from the output of complex radiation or global climate models (Li and Moreau 1996; Li et al. 1995). Despite its simplicity, values of the ratio were within 15% of those obtained from the Fu-Liou radiation model. Ramanathan et al. (1995) suggested that high values of $\mathfrak{R}$ was obtained by enhanced cloud absorption. By considering the case of thick clouds with the analytical expression, cloudy layer absorptance of approximately 0.30 were required to achieve

values of $\Re \approx 1.5$. This was greater than the maximum cloudy layer absorptance of 0.20 that was obtained from current radiation and climate models. This was not the only mechanism that was found to result in high values of $\Re$. Consideration of low level clouds resulted in high values of $\Re$ if the transmittance of the atmospheric layer above the cloudy layer was decreased to approximately 0.80. Such a decrease could be obtained by the introduction of a layer of absorbing aerosols above the cloudy layer. This possibility was investigated with the Fu-Liou radiation model. Above a low level stratus cloud, various amounts of absorbing aerosols were placed in a layer above the cloud. Extinction optical depths approaching 0.1 of strongly absorbing aerosols were required to obtain $\Re \approx 1.5$. Such high optical depths would only occur over highly polluted regions. The global annual mean optical depth of soot aerosols has been estimated to be only 0.003 (Schimel et al. 1996).

The issue concerning enhanced shortwave absorption of clouds was studied using a three layer atmospheric model. One of the limitations of this approach was that it applied to plane-parallel clouds. Clouds are finite in extent and microphysical properties are not constant within them. Studies into the finite inhomogeneous cloud effects should be continued (Lubin et al. 1996: Li et al. 1994: Li 1994).

Bibliography

Adkins, C. J. (1983). *Equilibrium Thermodynamics* (Third ed.). Cambridge, England: Cambridge University Press.

Ashkin, A. and J. M. Dziedzic (1977, June). Observation of resonances in the radiation pressure on dielectric spheres. *Phys. Rev. Lett. 38*(23), 1351–1354.

Bohren, C. F. and D. R. Huffman (1983). *Absorption and Scattering of Light by Small Particles.* New York, New York, U.S.A.: John Wiley & Sons, Inc.

Bondietti, E. A. and C. Papastefanou (1993). Estimates of residence times of sulfate aerosols in ambient air. *Science of the Total Environment 136*(1–2), 25–31.

Boucher, O. (1995, May). GCM estimate of the indirect aerosol forcing using satellite-retrieved cloud droplet effective radii. *J. Climate 8*, 1403–1409.

Boucher, O. and T. L. Anderson (1995, December). General circulation model assessment of the sensitivity of direct climate forcing by anthropogenic sulfate aerosols to aerosol size and chemistry. *J. Geophys. Res. 100*(D12), 26117–26134.

Boucher, O. and U. Lohmann (1995). The sulfate-CCN-cloud albedo effect: A sensitivity study with two general circulation models. *Tellus 47B*(3), 281–300.

Boucher, O., S. E. Schwartz, T. L. Ackerman, T. P. Anderson, B. Bergstrom, B. Bonnel, P. Chýlek, A. Dahlback, Y. Fouquart, Q. Fu, R. N. Halthore, T. Iversen, J. M. Haywood, S. Kato, S. Kinne, A. Kirkevåg, K. R. Knapp, A. Lacis, I. Laszlo, S. Nemesure, V. Ramaswamy, D. L. Roberts, P. Russell, M. E. Schlesinger, G. L. Stephens, R. Wagener, M. Wang, J. Wong, and F. Yang

(1998, July). Intercomparison of models representing direct shortwave radiative forcing by sulfate aerosols. *J. Geophys. Res. 103*(D14), 16979–16998.

Briegleb, B. P. (1992, May). Delta-Eddington approximation for solar radiation in the NCAR Community Climate Model. *J. Geophys. Res. 97*(D7), 7603–7612.

Brine, D. T. and M. Iqbal (1983). Diffuse and global solar spectral irradiance under cloudless skies. *Solar Energy 30*(5), 447–453.

Cachier, H., J. Ducret, M.-P. Brémond, V. Yoboué, J.-P. Lacaux, A. Gaudichet, and J. Baudet (1991). Biomass burning aerosols in a Savanna region of the Ivory Coast. In J. S. Levine (Ed.), *Global Biomass Burning: Atmospheric, Climatic, and Biospheric Implications*, Chapter 23, pp. 174–180. Cambridge, Massachusetts, U.S.A.: The MIT Press.

Callen, H. B. (1985). *Thermodynamics and an Introduction to Thermostatistics* (Second ed.). New York, New York: John Wiley & Sons, Inc.

Cess, R. D. and M. H. Zhang (1996, February). Response. *Science 271*, 1133–1134.

Cess, R. D., M. H. Zhang, P. Minnis, L. Corsetti, E. G. Dutton, B. W. Forgan, D. P. Garber, W. L. Gates, J. J. Hack, E. F. Harrison, X. Jing, J. T. Kiehl, C. N. Long, J.-J. Morcrette, G. L. Potter, V. Ramanathan, B. Subasilar, C. H. Whitlock, D. F. Young, and Y. Zhou (1995, January). Absorption of solar radiation by clouds: Observations versus models. *Science 267*, 496–499.

Cess, R. D., M. H. Zhang, Y. Zhou, X. Jing, and V. Dvortsov (1996, October). Absorption of solar radiation by clouds: Interpretations of satellite, surface, and aircraft measurements. *J. Geophys. Res. 101*(D18), 23299–23309.

Chan, C. K., R. C. Flagan, and J. H. Seinfeld (1992). Water activities of $NH_4NO_3/(NH_4)_2SO_4$ solutions. *Atmos. Environ. 26A*(9), 1661–1673.

Charlson, R. J., D. S. Covert, and T. V. Larson (1984). Observation of the effect of humidity on light scattering by aerosols. In L. H. Ruhnke and A. Deepak (Eds.), *Hygroscopic Aerosols*, pp. 35–44. Hampton, VA: A. Deepak Publishing.

Charlson, R. J., D. S. Covert, T. V. Larson, and A. P. Waggoner (1978). Chemical properties of tropospheric sulfur aerosols. *Atmos. Environ. 12*, 39–53.

Charlson, R. J., J. E. Lovelock, M. O. Andreae, and S. G. Warren (1987, April). Oceanic phytoplankton, atmospheric sulfur, cloud albedo and climate. *Nature 326*, 655–661.

Charlson, R. J., S. E. Schwartz, J. M. Hales, R. D. Cess, J. A. Coakley, Jr., J. E. Hansen, and D. J. Hofmann (1992, January). Climate forcing by anthropogenic aerosols. *Science 255*, 423–430.

Charlson, R. J. and T. M. L. Wigley (1994, February). Sulfate aerosol and climatic change. *Sci. Amer. 270*(2), 48–57.

Chou, M.-D., A. Arking, J. Otterman, and W. L. Ridgway (1995, July). The effect of clouds on atmospheric absorption of solar radiation. *Geophys. Res. Lett. 22*(14), 1885–1888.

Chuang, C. C., J. E. Penner, K. E. Taylor, A. S. Grossman, and J. J. Walton (1997, February). An assessment of the radiative effects of anthropogenic sulfate. *J. Geophys. Res. 102*(D3), 3761–3778.

Chýlek, P. and J. A. Coakley, Jr. (1974, January). Aerosols and climate. *Science 183*, 75–77.

Chýlek, P. and D. J. W. Geldart (1997, August). Water vapor dimers and atmospheric absorption of electromagnetic radiation. *Geophys. Res. Lett. 24*(16), 2015–2018.

Chýlek, P., J. T. Kiehl, and M. K. W. Ko (1978, November). Optical levitation and partial-wave resonances. *Phys. Rev. A 18*(5), 2229–2233.

Chýlek, P., G. B. Lesins, G. Videen, J. G. D. Wong, R. G. Pinnick, D. Ngo, and J. D. Klett (1996, October). Black carbon and absorption of solar radiation by clouds. *J. Geophys. Res. 101*(D18), 23365–23371.

Chýlek, P., V. Ramaswamy, A. Ashkin, and J. M. Dziedzic (1983, August). Simultaneous determination of refractive index and size of spherical dielectric particles from light scattering data. *Appl. Opt. 22*(15), 2302–2307.

Chýlek, P., V. Srivastava, R. G. Pinnick, and R. T. Wang (1988, June). Scattering of electromagnetic waves by composite spherical particles: experiment and effective medium approximations. *Appl. Opt. 27*(12), 2396–2404.

Chýlek, P., G. Videen, D. Ngo, R. G. Pinnick, and J. D. Klett (1995, August). Effect of black carbon on the optical properties and climate forcing of sulfate aerosols. *J. Geophys. Res. 100*(D8), 16325–16332.

Coakley, Jr., J. A., R. D. Cess, and F. B. Yurevich (1983, January). The effect of tropospheric aerosols on the Earth's radiation budget: A parameterization for climate models. *J. Atmos. Sci. 40*, 116–138.

Cohen, M. D., R. C. Flagan, and J. H. Seinfeld (1987). Studies of concentrated electrolyte solutions using the electrodynamic balance. 1. water activities for single-electrolyte solutions. *J. Phys. Chem. 91*(17), 4563–4574.

d'Almeida, G. A., P. Koepke, and E. P. Shettle (1991). *Atmospheric Aerosols: Global Climatology and Radiative Characteristics*. Hampton, Virginia, U.S.A.: A. Deepak Publishing.

Damiano, P. and P. Chýlek (1994, May). Shortwave radiative properties of clouds: Numerical study. *J. Atmos. Sci. 51*(9), 1223–1233.

Downing, H. D. and D. Williams (1975, April). Optical constants of water in the infrared. *J. Geophys. Res. 80*(12), 1656–1661.

Doyle, G. J. (1961, September). Self-nucleation in the sulfuric acid-water system. *J. Chem. Phys. 35*(3), 795–799.

Einfeld, W., D. E. Ward, and C. Hardy (1991). Effects of fire behavior on prescribed fire smoke characteristics: A case study. In J. S. Levine (Ed.), *Global Biomass Burning: Atmospheric, Climatic, and Biospheric Implications*, Chapter 50, pp. 412–419. Cambridge, Massachusetts, U.S.A.: The MIT Press.

Engardt, M. and H. Rodhe (1993, January). A comparison between patterns of temperature trends and sulfate aerosol pollution. *Geophys. Res. Lett.* *20*(2), 117–120.

Erickson III, D. J., R. J. Oglesby, and S. Marshall (1995, August). Climate response to indirect anthropogenic sulfate forcing. *Geophys. Res. Lett.* *22*(15), 2017–2020.

Feichter, J., U. Lohmann, and I. Schult (1997). The atmospheric sulfur cycle in ECHAM-4 and its impact on the shortwave radiation. *Climate Dynamics 13*, 235–246.

Finlayson-Pitts, B. J. and J. N. Pitts, Jr. (1986). *Atmospheric Chemistry: Fundamentals and Experimental Techniques.* New York, New York, U.S.A.: John Wiley & Sons.

Flageollet, C., M. D. Cao, and P. Mirabel (1980, January). Experimental study of nucleation in binary mixtures: The methanol-water and n-propanol-water systems. *J. Chem. Phys. 72*(1), 544–549.

Fu, Q. (1991). *Parameterization of radiative processes in vertically nonhomogeneous multiple scattering atmospheres.* Meteorology, University of Utah, Utah, U.S.A.

Fung, K. H., I. N. Tang, and H. R. Munkelwitz (1987, April). Study of condensational growth of water droplets by Mie resonance spectroscopy. *Appl. Opt. 26*(7), 1282–1287.

Gerber, H. E. (1985, December). Relative-humidity parameterization of the navy aerosol model (NAM). NRL Report 8956, U.S. Naval Research Laboratory, Washington, D.C., U.S.A.

Gong, S. L., L. A. Barrie, and J.-P. Blanchet (1997, February). Modeling sea-salt aerosols in the atmosphere i. model development. *J. Geophys. Res. 102*(D3), 3805–3818.

Goody, R. M. and Y. L. Yung (1989). *Atmospheric Radiation* (Second ed.). New York, New York, U.S.A.: Oxford University Press, Inc.

Gosse, S. F., M. Wang, D. Labrie, and P. Chýlek (1997, June). Imaginary part of the refractive index of sulfates and nitrates in the 0.7 - 2.6 μm spectral region. *Appl. Opt.* *36*(16), 3622–3634.

Hale, G. and M. Querry (1984). Optical constants of water in the 200 nm to 200 μm wavelength region. *Appl. Opt.* *23*, 1206–1225.

Hansen, J. E. and L. D. Travis (1974). Light scattering in planetary atmospheres. *Space Sci. Rev.* *16*, 527–610.

Harrison, E. F., P. Minnis, B. R. Barkstrom, V. Ramanathan, R. D. Cess, and G. G. Gibson (1990, October). Seasonal variation of cloud radiative forcing derived from the Earth Radiation Budget Experiment. *J. Geophys. Res.* *95*(D11), 18687–18703.

Hartmann, D. L. (1993). Radiative effect of clouds on earth's climate. In P. V. Hobbs (Ed.), *Aerosol-Cloud-Climate Interactions*, Volume 54 of *International Geophysics Series*, Chapter 6, pp. 151–173. San Diego, California, U.S.A.: Academic Press, Inc.

Hayasaka, T., N. Kikuchi, and M. Tanaka (1995, May). Absorption of solar radiation by stratocumulus clouds: Aircraft measurements and theoretical calculations. *J. Appl. Meteor.* *34*, 1047–1055.

Haywood, J. M. and V. Ramaswamy (1998, March). Global sensitivity studies of the direct radiative forcing due to anthropogenic sulfate and black carbon aerosols. *J. Geophys. Res.* *103*(D6), 6043–6058.

Haywood, J. M., D. L. Roberts, A. Slingo, J. M. Edwards, and K. P. Shine (1997, July). General circulation model calculations of the direct radiative forcing by anthropogenic sulfate and fossil-fuel soot aerosol. *J. Climate* *10*, 1562–1577.

Haywood, J. M. and K. P. Shine (1995, March). The effect of anthropogenic sulfate and soot aerosol on the clear sky planetary radiation budget. *Geophys. Res. Lett.* *22*(5), 603–606.

Hegerl, G. C. and U. Cubasch (1996). Greenhouse gas induced climate change. *Environ. Sci. & Pollut. Res.* *3*(2), 99–102.

Hegerl, G. C., H. von Storch, K. Hasselmann, B. D. Santer, U. Cubasch, and Jon (1996, October). Detecting greenhouse-gas-induced climate change with an optimal fingerprint method. *J. Climate* *9*(10), 2281–2306.

Helsper, C., H. J. Fissan, J. Muggli, and A. Scheidweiler (1980). Particle number distributions of aerosols from test fires. *J. Aerosol Sci.* *11*, 439–446.

Hobbs, P. V. (1995). *Basic Physical Chemistry for the Atmospheric Sciences.* Cambridge, England: Cambridge University Press.

Holben, B. N., Y. J. Kaufman, A. W. Setzer, D. D. Tanre, and D. E. Ward (1991). Optical properties of aerosol emissions from biomass burning in the tropics, BASE-A. In J. S. Levine (Ed.), *Global Biomass Burning: Atmospheric, Climatic, and Biospheric Implications*, Chapter 49, pp. 403–411. Cambridge, Massachusetts, U.S.A.: The MIT Press.

Howell, W. E. (1949, April). The growth of cloud drops in uniformly cooled air. *J. Meteorol.* *6*, 134–149.

Jaenicke, R. (1993). Tropospheric aerosols. In P. V. Hobbs (Ed.), *Aerosol-Cloud-Climate Interactions*, Volume 54 of *International Geophysics Series*, Chapter 1, pp. 1–31. San Diego, California: Academic Press, Inc.

Jones, A., D. L. Roberts, and A. Slingo (1994, August). A climate model study of indirect radiative forcing by anthropogenic sulphate aerosols. *Nature* *370*(6489), 450–453.

Jones, P. D. and K. R. Briffa (1992). Global surface air temperature variations during the twentieth century: Part 1, spatial, temporal and seasonal details. *The Holocene* *2*(2), 165–179.

Kiehl, J. T. (1994, November). Clouds and their effect on the climate system. *Phys. Today* *47*(11), 36–42.

Kiehl, J. T. and B. P. Briegleb (1993, April). The relative roles of sulfate aerosols and greenhouse gases in climate forcing. *Science 260*, 311–314.

Kiehl, J. T., J. J. Hack, M. H. Zhang, and R. D. Cess (1995, September). Sensitivity of a GCM climate to enhanced shortwave cloud absorption. *J. Climate 8*(9), 2200–2212.

Kiehl, J. T. and H. Rodhe (1995). Modeling geographical and seasonal forcing due to aerosols. In R. J. Charlson and J. Heintzenberg (Eds.), *Aerosol Forcing of Climate*, Chapter 15, pp. 281–296. John Wiley & Sons Ltd.

Kiehl, J. T. and K. E. Trenberth (1997, February). Earth's annual global mean energy budget. *Bull. Amer. Meteor. Soc. 78*(2), 197–208.

Köhler, H. (1936). The nucleus in and the growth of hygroscopic droplets. *Trans. Faraday Society 32*, 1152–1161.

Konopka, P. (1996, November). A reexamination of the derivation of the equilibrium supersaturation curve for soluble particles. *J. Atmos. Sci. 53*(21), 3157–3163.

Kou, L., D. Labrie, and P. Chýlek (1993, July). Refractive indices of water and ice in the 0.65– to 2.5– μm spectral range. *Appl. Opt. 32*(19), 3531–3540.

Langner, J. and H. Rodhe (1991). A global three-dimensional model of the tropospheric sulfur cycle. *J. Atmos. Chem. 13*, 255–263.

Lenoble, J. (1993). *Atmospheric Radiative Transfer*. Studies in Geophysical Optics and Remote Sensing. Hampton, Virginia, U.S.A.: A. Deepak Publishing.

Li, J. (1994). *Radiative transfer in clouds with internal inhomogeneity*. Physics, Dalhousie University, Halifax, Nova Scotia, Canada.

Li, J., D. J. W. Geldart, and P. Chýlek (1994, September). Solar radiative transfer in clouds with vertical internal inhomogeneity. *J. Atmos. Sci. 51*(17), 2542–2552.

Li, Z. (1998, January). Influence of absorbing aerosols on the inference of the solar surface radiation budget and cloud absorption. *J. Climate* *11*(1), 5–17.

Li, Z., H. W. Barker, and L. Moreau (1995, August). The variable effect of clouds on atmospheric absorption of solar radiation. *Nature* *376*, 486–490.

Li, Z. and L. Moreau (1996, May). Alteration of atmospheric solar absorption by clouds: Simulation and observation. *J. Appl. Meteor.* *35*(5), 653–670.

Li, Z., L. Moreau, and A. Arking (1997, January). On solar energy disposition: A perspective from observation and modeling. *Bull. Amer. Meteor. Soc.* *78*(1), 53–70.

Liang, Z. and C. K. Chan (1997, March). A fast technique for measuring water activity of atmospheric aerosols. *Aerosol Sci. Technol.* *26*(3), 255–268.

Lide, D. R. (Ed.) (1997). *CRC Handbook of Chemistry and Physics* (Seventy-Eighth ed.). Boca Raton, Florida, U.S.A.: CRC Press, Inc.

Liou, K.-N. (1980). *An Introduction to Atmospheric Radiation*, Volume 26 of *International Geophysics Series*. New York, New York, U.S.A.: Academic Press, Inc.

Liou, K. N. (1992). *Radiation and Cloud Processes in the Atmosphere*. New York, New York, U.S.A.: Oxford University Press, Inc.

Liou, K.-N. and Q. Fu (1988, July). A simple formulation of the delta-four-stream approximation for radiative transfer parameterizations. *J. Atmos. Sci.* *45*(13), 1940–1947.

Lohmann, U. and J. Feichter (1997, June). Impact of sulfate aerosols on albedo and lifetime of clouds: A sensitivity study with the ECHAM4 GCM. *J. Geophys. Res.* *102*(D12), 13685–13700.

Low, R. D. H. (1969, May). A generalized equation for the solution effect in droplet growth. *J. Atmos. Sci.* *26*, 608–611.

Lubin, D., J.-P. Chen, P. Pilewskie, V. Ramanathan, and F. P. J. Valero (1996, July). Microphysical examination of excess absorption in the tropical atmosphere. *J. Geophys. Res.* *101*(D12), 16961–16972.

McClatchey, R. A., R. W. Fenn, J. E. A. Selby, F. E. Volz, and J. S. Garing (1971). Optical properties of the atmosphere. Technical Report AFCRL-71-0279, Air Force Cambridge Research Laboratory, Bedford, Massachusetts, U.S.A.

McDonald, J. E. (1953, February). Erroneous cloud-physics applications of Raoult's law. *J. Meteorol.* *10*, 68–70.

Meehl, G. A., W. M. Washington, D. J. Erickson III, B. P. Briegleb, and P. J. Jaumann (1996, December). Climate change from increased CO_2 and direct and indirect effects of sulfate aerosols. *Geophys. Res. Lett.* *23*(25), 3755–3758.

Mulholland, G. and T. J. Ohlemiller (1982). Aerosol characterization of a smoldering source. *Aerosol Sci. Technol.* *1*, 59–71.

Nemesure, S., R. Wagener, and S. E. Schwartz (1995, December). Direct shortwave forcing of climate by anthropogenic sulfate aerosol: Sensitivity to particle size, composition, and relative humidity. *J. Geophys. Res.* *100*(D12), 26105–26116.

Palmer, K. F. and D. Williams (1974, August). Optical properties of water in the near infrared. *J. Opt. Soc. Amer.* *64*(8), 1107–1110.

Palmer, K. F. and D. Williams (1975, January). Optical constants of sulfuric acid; application to the clouds of Venus? *Appl. Opt.* *14*(1), 208–219.

Pan, W., M. A. Tatang, G. J. McRae, and R. G. Prinn (1997, September). Uncertainty analysis of direct radiative forcing by anthropogenic sulfate aerosols. *J. Geophys. Res.* *102*(D18), 21915–21924.

Penner, J. E., R. E. Dickinson, and C. A. O'Neill (1992, June). Effects of aerosol from biomass burning on the global radiation budget. *Science* *256*, 1432–1434.

Pham, M., J.-F. Müller, G. P. Brasseur, C. Granier, and G. Mégie (1995, December). A three-dimensional study of the tropospheric sulfur cycle. *J. Geophys.*
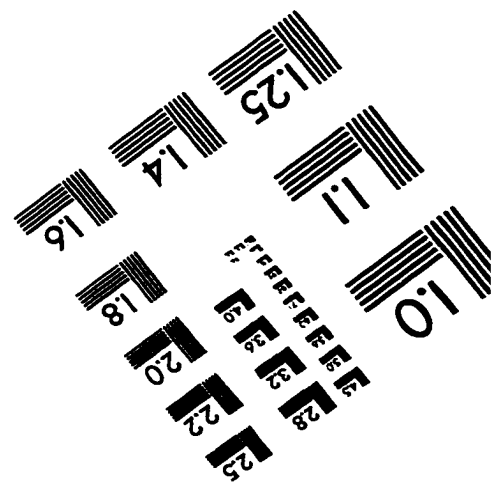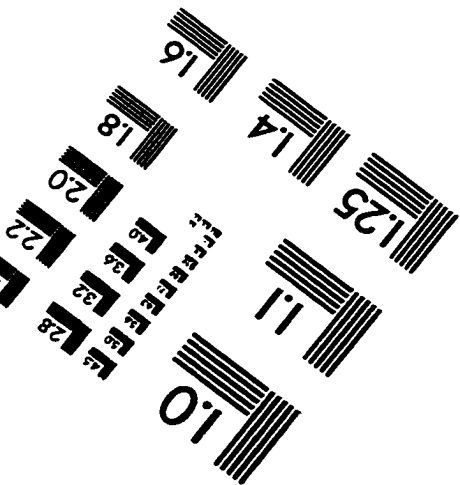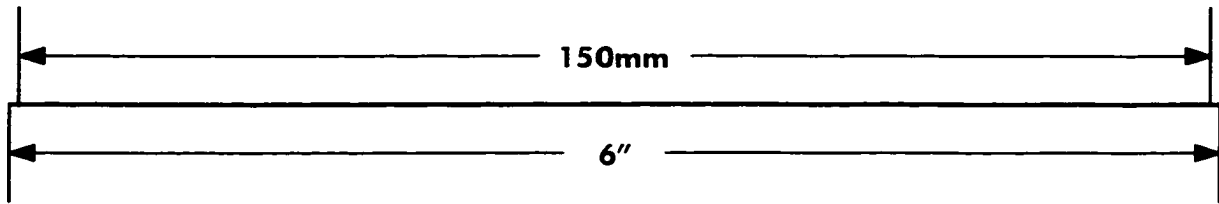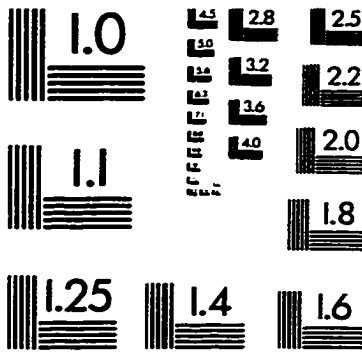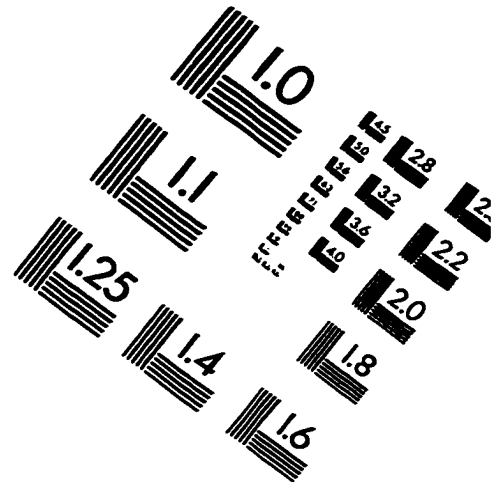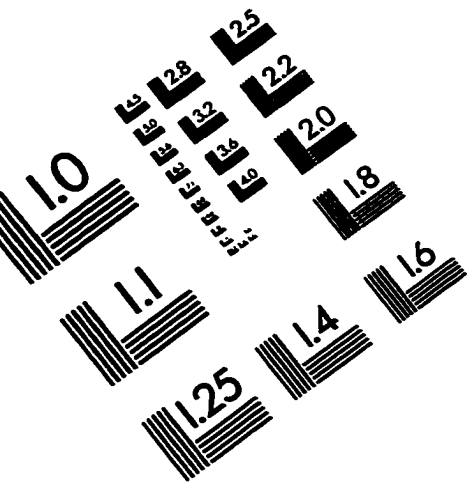
Res. 100(D12), 26061–26092.

Pilewskie, P. and F. P. J. Valero (1995, March). Direct observations of excess solar absorption by clouds. *Science 267*, 1626–1629.

Pilewskie, P. and F. P. J. Valero (1996, February). Response. *Science 271*, 1134–1136.

Pilinis, C., S. N. Pandis, and J. H. Seinfeld (1995, September). Sensitivity of direct climate forcing by atmospheric aerosols to aerosol size and composition. *J. Geophys. Res. 100*(D9), 18739–18754.

Pruppacher, H. R. and J. D. Klett (1997). *Microphysics of Clouds and Precipitation* (Second ed.), Volume 18 of *Atmospheric and Oceanographic Sciences Library*. Dordrecht, Holland: Kluwer Academic Publishers.

Radke (1991). Particulate and trace gas emissions from large biomass fires in North America. In J. S. Levine (Ed.), *Global Biomass Burning: Atmospheric, Climatic, and Biospheric Implications*, Chapter 28, pp. 209–224. Cambridge, Massachusetts, U.S.A.: The MIT Press.

Ramanathan, V., B. Subasilar, G. J. Zhang, W. Conant, R. D. Cess, J. T. Kiehl, H. Grassl, and L. Shi (1995, January). Warm pool heat budget and shortwave cloud forcing: A missing physics? *Science 267*, 499–503.

Reiss, H. (1950, June). The kinetics of phase transitions in binary systems. *J. Chem. Phys. 18*(6), 840–848.

Reiss, H. and G. J. M. Koper (1995). The Kelvin relation: Stability, fluctuation, and factors involved in measurement. *J. Phys. Chem. 99*(19), 7837–7844.

Rieland, M. and E. Raschke (1991). Diurnal variability of the Earth radiation budget: Sampling requirements, time integration aspects and error estimates for the Earth Radiation Budget Experiment (ERBE). *Theor. Appl. Climatol. 44*, 9–24.

Rogers, R. R. and M. K. Yau (1989). *A Short Course in Cloud Physics* (Third ed.). Oxford, England: Pergamon Press.

Russell, P. B., J. M. Livingston, R. F. Pueschel, J. J. Bauman, J. B. Pollack, S. L. Brooks, P. Hamill, L. W. Thomason, L. L. Stowe, T. Deshler, E. G. Dutton, and R. W. Bergstrom (1996, August). Global to microscale evolution of the Pinatubo volcanic aerosol derived from diverse measurements and analyses. *J. Geophys. Res. 101*(D13), 18745–18763.

Sagan, C. and J. B. Pollack (1967, January). Anisotropic nonconservative scattering and the clouds of Venus. *J. Geophys. Res. 72*(2), 469–477.

Schimel, D., D. Alves, I. Enting, M. Heimann, F. Joos, D. Raynaud, T. Wigley, M. Prather, R. Derwent, D. Ehhalt, P. Fraser, E. Sanhueza, X. Zhou, P. Jonas, R. Charlson, H. Rodhe, S. Sadasivan, K. P. Shine, Y. Fouquart, V. Ramaswamy, S. Solomon, J. Srinivasan, D. Albritton, R. Derwent, I. Isaksen, M. Lal, and D. Wuebbles (1996). Radiative forcing of climate change. In J. T. Houghton, L. G. M. Filho, B. A. Callander, N. Harris, A. Kattenberg, and K. Maskell (Eds.), *Climate Change 1995: The Science of Climate Change*, Intergovernmental Panel on Climate Change, Chapter 2, pp. 65–131. Cambridge, England: Cambridge University Press.

Stephens, G. L. (1978, November). Radiation profiles in extended water clouds. I: Theory. *J. Atmos. Sci. 35*, 2111–2122.

Stephens, G. L. (1996, February). How much solar radiation do clouds absorb? *Science 271*, 1131–1133.

Tang, I. N. (1996, August). Chemical and size effects of hygroscopic aerosols on light scattering coefficients. *J. Geophys. Res. 101*(D14), 19245–19250.

Tang, I. N. (1997, January). Thermodynamic and optical properties of mixed-salt aerosols of atmospheric importance. *J. Geophys. Res. 102*(D2), 1883–1893.

Tang, I. N. and H. R. Munkelwitz (1994, September). Water activities, densities,

and refractive indices of aqueous sulfates and sodium nitrate droplets of atmospheric importance. *J. Geophys. Res.* *99*(D9), 18801–18808.

Tang, I. N., H. R. Munkelwitz, and J. H. Lee (1988). Vapor-liquid equilibrium measurements for dilute nitric acid solutions. *Atmos. Environ.* *22*(11), 2579–2585.

Tang, I. N., A. C. Tridico, and K. H. Fung (1997, October). Thermodynamic and optical properties of sea salt aerosols. *J. Geophys. Res.* *102*(D19), 23269–23275.

Taylor, K. E. and J. E. Penner (1994, June). Response of the climate system to atmospheric aerosols and greenhouse gases. *Nature* *369*, 734–737.

Thekaekara, M. P. and A. J. Drummond (1971, January). Standard values for the solar constant and its spectral components. *Nature Physical Science* *229*, 6–9.

Toon, O. B., J. B. Pollack, and B. N. Khare (1976, November). The optical constants of several atmospheric aerosol species: Ammonium sulfate, aluminum oxide, and sodium chloride. *J. Geophys. Res.* *81*(33), 5733–5748.

Trenberth, K. E., J. T. Houghton, and L. G. M. Filho (1996). The climate system: an overview. In J. T. Houghton, L. G. M. Filho, B. A. Callander, N. Harris, A. Kattenberg, and K. Maskell (Eds.), *Climate Change 1995: The Science of Climate Change*, Intergovernmental Panel on Climate Change, Chapter 1, pp. 51–64. Cambridge, England: Cambridge University Press.

Twomey, S. (1974). Pollution and the planetary albedo. *Atmos. Environ.* *8*, 1251–1256.

Twomey, S. (1977, July). The influence of pollution on the shortwave albedo of clouds. *J. Atmos. Sci.* *34*, 1149–1152.

Twomey, S. A., M. Piepgrass, and T. L. Wolfe (1984). An assessment of the impact of pollution on global cloud albedo. *Tellus* *36B*, 356–366.

van de Hulst, H. C. (1980). *Multiple Light Scattering: Tables, Formulas, and Applications*, Volume 1. New York, New York, U.S.A.: Academic Press.

van de Hulst, H. C. (1981). *Light Scattering by Small Particles.* New York, New York, U.S.A.: Dover Publications, Inc.

Volz, F. E. (1972, April). Infrared refractive index of atmospheric aerosol substances. *Appl. Opt. 11*(4), 755–759.

Wallace, J. M. and P. V. Hobbs (1977). *Atmospheric Science: An Introductory Survey.* New York, New York, U.S.A.: Academic Press, Inc.

Whitby, K. T. (1978). The physical characteristics of sulfur aerosols. *Atmos. Environ. 12,* 135–159.

Wielicki, B. A., R. D. Cess, M. D. King, D. A. Randall, and E. F. Harrison (1995, November). Mission to planet Earth: Role of clouds and radiation in climate. *Bull. Amer. Meteor. Soc. 76*(11), 2125–2153.

Wilemski, G. (1984, February). Composition of the critical nucleus in multicomponent vapor nucleation. *J. Chem. Phys. 80*(3), 1370–1372.

Wilemski, G. (1988, April). Some issues of thermodynamic consistency in binary nucleation theory. *J. Chem. Phys. 88*(8), 5134–5136.

Winter, B. and P. Chýlek (1997). Contribution of sea salt aerosol to the planetary clear-sky albedo. *Tellus 49B,* 72–79.

Wiscombe, W. J. and G. W. Grams (1976, December). The backscattered fraction in two-stream approximations. *J. Atmos. Sci. 33,* 2440–2451.

Woods, D. C., R. L. Chuan, W. R. Cofer, III, and J. S. Levine (1991). Aerosol characterization in smoke plumes from a wetlands fire. In J. S. Levine (Ed.), *Global Biomass Burning: Atmospheric, Climatic, and Biospheric Implications,* Chapter 31, pp. 240–244. Cambridge, Massachusetts, U.S.A.: The MIT Press.

Young, K. C. and A. J. Warren (1992, July). A reexamination of the derivation of the equilibrium supersaturation curve for soluble particles. *J. Atmos. Sci. 49*(13), 1138–1143.

IMAGE EVALUATION
TEST TARGET (QA-3)

150mm

6"